Role of ultrasonic shear rate estimation errors in assessing inflammatory response and vascular risk

BY

JEAN KAOHUI TSOU

B.S. (National Taiwan University, Taipei, Taiwan) 2001

Submitted in partial satisfaction of the requirements for the degree of

DOCTOR OF PHILOSOPY

in

Biomedical Engineering

in the

OFFICE OF GRADUATE STUDIES

of the

UNIVERSITY OF CALIFORNIA

DAVIS

Approved:

Michael F. Insana

Scott I. Simon

Abdul I Barakat

Committee in Charge

2006

ABSTRACT

Vascular hemodynamics, most notably vascular wall shear stress (WSS), play an important role in atherogenesis. Endothelial cell dysfunction would lead to the development of atherosclerosis. Routine monitoring of vascular WSS can identify the potential sites of early atherosclerotic plaques. Noninvasive ultrasonic narrow-band Doppler imaging with high signal power has been widely used for blood flow visualization. However, its increase in echo signal-to-noise ratio (eSNR) is gained at the cost of spatial resolution, and therefore results in significant bias in the WSR estimation. In order to link WSR profiles with atherosclerosis pathobiology, there is an urgent need for improvement in ultrasonic imaging technique. The goal of this dissertation is to develop a new method to provide reliable WSR measurements to assess vascular hemodynamics, endothelial cell function, and risk for focal plaque development.

We apply broadband coded excitation techniques with compression on the received signals to demonstrate an increase in eSNR while maintaining high image resolution. The feasibility of coded-pulse excitation implemented for ultrasonic shear rate imaging is examined for both *in vitro* phantom and *in vivo* imaging. At noise-limited conditions, coded pulses reduce errors in WSR measurement by half compared with uncoded ones. Ultrasonic WSR errors are found to increase slightly with shear. Within the physiological shear range of 0-1.6 Pa, shear-regulated vascular function is investigated through *in vitro* studies on cultured human aortic endothelium. The

expression of cell adhesion molecules VCAM-1 and E-selectin are found to positively associate with the efficiency of monocyte recruitment, where they are most responsive to low fluid shear (< 0.4 Pa). The differential shear regulation on endothelial cell function indicates that endothelium exposed to low fluid shear exhibits a higher tendency to have inflammatory response that triggers atherogenesis.

At the end of the dissertation, a connection between the shear-dependent ultrasonic WSR estimation errors and the shear-sensitive endothelial function is established. The results indicate that it is important to optimize ultrasonic shear imaging techniques when WSS is below 0.8 Pa, where cell adhesion molecule expression is highly sensitive to shear. This series of comprehensive study laid the groundwork for developing methods to optimize and evaluate new ultrasonic shear flow imaging techniques.

TABLE OF CONTENTS

LIST OF FIGURES AND PHOTOGRAPHS

LIST OF TABLES

1. INTRODUCTION

1.1. Motivation for improving ultrasonic imaging for monitoring hemodynamics in cardiovasculature.

Cardiovascular disease has been the leading cause of mortality in the United States since 1900.[1] Cardiovascular disease claims more lives each year than the next four leading causes of death combined, which include cancer, chronic lower respiratory diseases, accidents and diabetes mellitus.[1] The cost in lives and medical bills can be dramatically reduced with early detection and treatment. Cardiovascular disease often results from atherosclerosis,[2] which is an arterial disease characterized by the accumulation of lipids and calcification within the vascular wall.[3] It is known as a geometrically focal disease and originates preferentially near regions of high vessel curvature and branchings that exhibit certain hemodynamic patterns.[4] Routine monitoring of vascular hemodynamics can be useful for identifying potential sites of early atherosclerotic plaque formation. Therefore, low-cost, non-invasive and reliable imaging techniques to track blood vessel dynamics are needed.

1.2. Hemodynamics, vascular homeostasis, and atherosclerosis.

Vascular hemodynamics, most notably vascular wall stress (WSS) acting on the endothelial cell (EC) surface has been identified as an important factor in initiation of atherogenesis.[5] Shear stress has been shown to be a critical determinant of vessel

health. It has also been implicated in vascular remodeling related to pathobiology. As shown in Eqn. 1, WSS is the product of blood viscosity (μ) and the radial velocity gradient known as wall shear rate (WSR).

$$\text{WSS} = \mu \text{ WSR} \text{ , where} \quad \text{WSR} = \left.\frac{dV}{dr}\right|_{r=r_0} . \tag{1}$$

r is the radial position within the vascular lumen and r_0 is the instantaneous lumen radius.

Current literature suggests that arteries adjust their diameters reflexively so as to maintain a physiological time-averaged WSS in a narrow range of values between 1.2-1.7 Pa. This is carried out through the action of the mechanically-responsive endothelium that preserves the homeostasis of blood vessel structure and function.[6,5] Instantaneous vascular WSS ranges from 0.1-0.6Pa in the venous system and between 1-7 Pa in the arterial vascular network.[5] Arterial level of WSS at elevated magnitude ($>$ 1.2 Pa) induces endothelial quiescence and an atheroprotective gene expression profile, such as decreased endothelial turnover, decreased apoptosis, increased the production of vasodilators, paracrine growth inhibitors, fibronolytics and antioxidants, and suppressed production of vasoconstrictors, paracrine and growth promoters.

Intimal thickening is an important sign of early atherosclerosis development. Carotid artery bifurcation, coronary, infrarenal and femoral arteries are the most common sites of atherosclerotic lesion development. The carotid bifurcation and segments of

coronary arteries near branch points are particularly susceptible to plaque development.[7] Correlations between fluid dynamic variables and intimal thickness revealed that atherosclerotic plaques tended to occur at the curvatures and branching sites, where hemodynamic WSS is usually lower (<0.4 Pa) than the athero-protected regions, and also exhibit disturbed and non-uniform shear gradient flow patterns.[6,5] These shear patterns induce both structural and functional changes in endothelial cells such as enhancing membrane permeability, inflammation, leukocyte adhesion, and the expression of vasoconstrictors. These changes lead to arterial wall remodeling, atheroma, and eventually atherosclerosis.[8] The shear-rate-related mechanism[2] implies that mass transport between the blood and the endothelium lining the vessel wall is a key factor.

1.3. Atherogenesis

The development of atherosclerosis is summarized into five major steps: lesion initiation, inflammation, foam cell formation, formation of fibrous plaques, and formation of complex lesions and thrombosis (Fig. 1).[9] Current theory suggests WSS plays an important role in the first two steps.[10] Abnormal WSS patterns initiate lesion formation and promote inflammation. Literature shows that when ECs experience low and oscillatory shear stress, the membrane permeability to low density lipoprotein (LDL) increases significantly, causing LDL accumulation in the subendothelial matrix.[11] Trapped LDL undergoes modifications, most notably oxidation, and are then taken up by macrophages to generate foam cells.[12] Inflammation in atherosclerosis

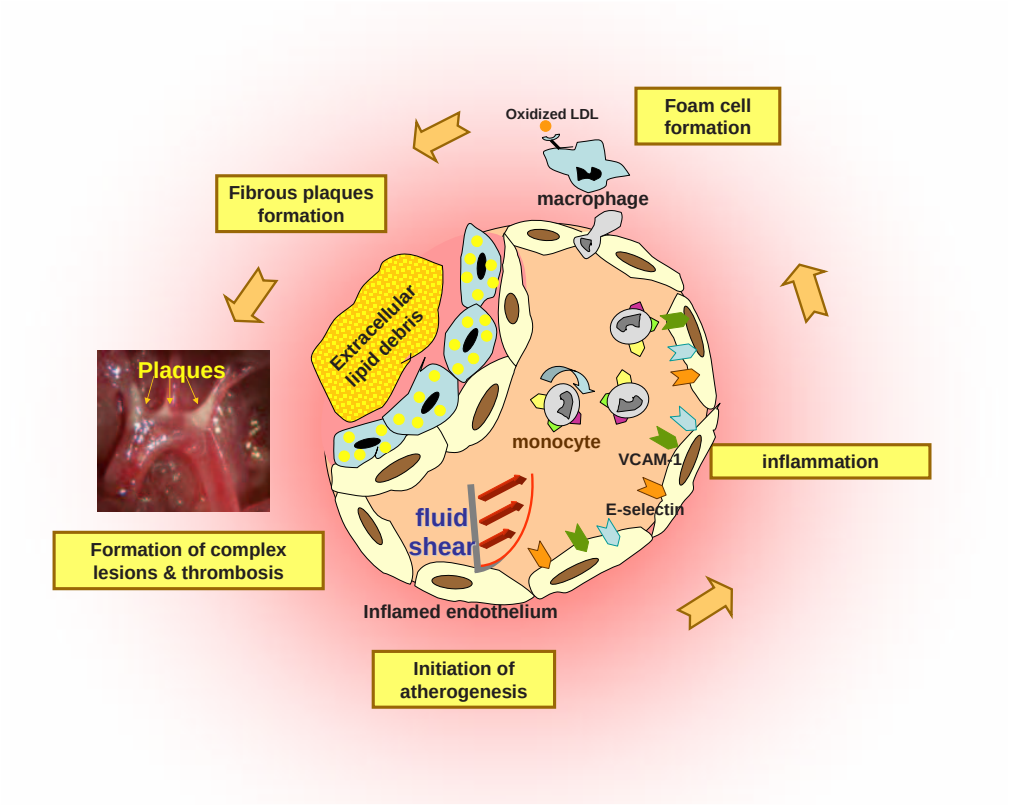

Figure 1. Development of atherosclerosis

is characterized by the recruitment of monocytes and lymphocytes, but not neutrophils, to the artery wall.[9] A triggering event for this process is the accumulation of minimally oxidized LDL, which stimulates the overlying ECs to produce a number of pro-inflammatory molecules, including cell adhesion molecules (CAMs, such as vascular cell adhesion molecule-1 (VCAM-1), intravascular cell adhesion molecule-1 (ICAM-1) and E-selectin) and growth factors. Monocyte recruitment into the subendothelial space is the key step in the development of atherosclerosis that leads to the formation of foam cells and complex plaques. Shear stress and chemotactic factors regulate the expression level of CAMs, which supply the binding force that supports

leukocyte attachment to the endothelium. Therefore, the level of CAM expressed on the surface of endothelium under different shear conditions has been widely studied over the past decade.

1.4. Endothelial cell function and hemodynamics

Functional regulation of the endothelium by local hemodynamic shear stress of known geometry provides a model for understanding the focal propensity of vessels toward plaque formation in the setting of systemic factors.

In order to understand the mechanism of shear-regulated EC function, flow chambers with simple geometry that deliver well-defined shear fields to a monolayer of cultured endothelium have been commonly used.

Current studies that focus on the dependence of in vivo shear flow regulation on EC function have taken three approaches: 1) the impact of the magnitude of the applied shear stress, 2) the influence of applying temporal-varying shear profiles (i.e. oscillatory, pulsatile and steady) and 3) the effect of introducing a complex shear flow patterns including directional change and flow disturbance.

1.4.1. Uniform laminar shear field

A parallel-plate flow chamber (PPFC) and Couette flow apparatus[13] are commonly used to generate a uniform and constant shear flow field for *in vitro* studies.

A PPFC that consists of parallel plates as the upper and lower sides of a chamber of rectangular cross-section produces a uniform fully developed two-dimensional

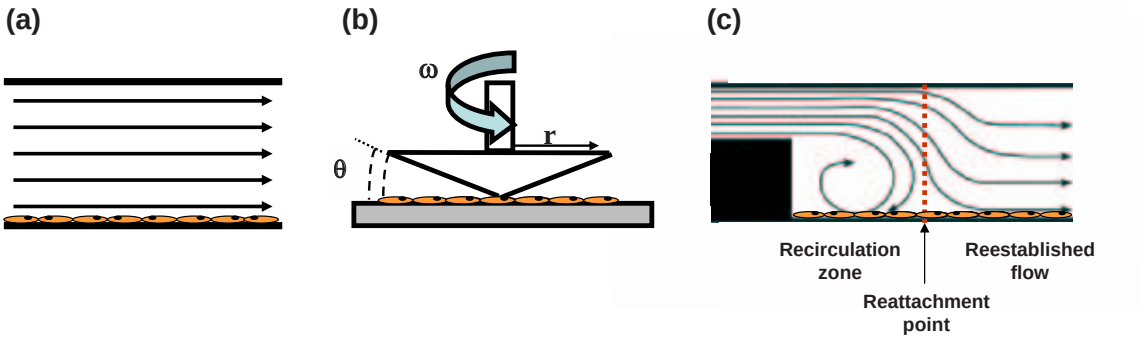

Figure 2. ***In vitro*** **hydrodynamic flow models. (a) parallel-plate flow chamber, (b) Couette flow apparatus (cone-plate viscometer) and (c) vertical step flow chamber.**

flow (Fig. 2 a). Endothelium seeded on the bottom plate surface are subjected to unidirectional shear stress using steady or pulsatile laminar flow. PPFCs are usually constructed of lucite or other transparent materials to allow for continuous microscopic viewing and recording of cell morphology.

Couette flow apparatus utilizes the geometry of a cone-plate viscometer (Fig. 2 b). Shear stress is produced in the fluid contained between a stationary plate and a rotating cone. Monolayers of endothelial cells grown on coverslips can be placed at various radial distances from the center of the cone where they experience the same shear stress magnitudes in laminar flow but quite different average stress when flow conditions include turbulence or a combination of laminar and turbulent flows at varying radial distances.

The shear stress generated in these two flow apparatuses is controlled mainly by

the input flow rate or angular speed between the rotating cone and the stationary plate. The resulted uniform WSS field can be estimated via,

$$\tau_w = \frac{6\mu Q}{w^2 h}\ , \text{ for PPFC} \tag{2}$$

$$\tau_w = \frac{\mu r\omega}{r\tan\theta} \sim \frac{\mu\omega}{\sin\theta}, \text{for Couette apparatus, (when } \theta \text{ is small, } \tan\theta \sim \sin\theta) \tag{3}$$

μ is the fluid viscosity, Q is the volumetric flow rate, w, h are the length and width of the PPFC, ω is the angular velocity, r is the radius of the rotating cone, and θ is the angel between the surface of the cone and the plate in the Couette flow apparatus.

Since each flow or rotation rate can only generate one particular shear stress field, the response of EC over a range of WSS is achieved by varying the flow rate or rotation rate in separate experiments.[14–18]

Shear flow studies using these two methods suggest that EC function can be altered by changing WSS in different aspects. The investigated shear range have generally been focused on two narrow shear ranges. High WSS has been applied to model the value observed in arteries of healthy human subjects (i.e. 1.2-1.7 Pa) and is shown atheroprotective.[6] Within this WSS range, the flow-sensitive ion (K^+ and Cl^-) channels are activated, and thus change EC membrane potential. This alters the electrochemical gradient for calcium transport across the membrane[19] and leads to an influx of calcium into the endothelium,[20] increasing the production of nitric oxide (NO).[21] Secretion of NO into the vessel lumen initiates a series of reactions that prevent atherosclerosis including reduction of the adhesive properties of platelets

and leukocytes, which helps to remove low-density lipoprotein. Increased levels of NO within endothelial cells alters metabolic pathways leading to endothelial cell activation. Secretion of NO into the smooth muscle cells of the media causes vasorelaxation and reduces the inflammatory response and EC proliferation. NO also suppresses the expression of endothelin-1,[18] vascular cell adhesion molecule-1 (VCAM-1),[22,14] where studies have shown a strong link between high VCAM-1 and atherosclerosis.[23,24]

Conversely, preconditioning EC at low WSS (i.e. 0.2-0.4 Pa) results in atherogenic conditions associated with membrane upregulation of VCAM-1 and E-selectin,[14–16,10,25] EC permeability to macro-molecules and increased efficiency of monocyte recruitment on inflamed EC.[5,16,26,27] These changes increase the tendency of endothelial cells to become atherosclerosis-prone cells and promote monocyte capture.[5] Low shear also contributes to an increase in monocyte adhesion by elongating the interaction time between monocytes and the adhesion molecules expressed on the endothelium surface. Also monocyte adhesion is elevated through expression of adhesion molecules on endothelial cells.

1.4.2. The impact of temporal variation in shear flow profile.

Temporally-varying flow profiles such as oscillatory and pulsatile flow for *in vitro* flow models are generally achieved by infusing a time-varying inflow into a PPFC.[28] Significant amplification in VCAM-1, ICAM-1 and E-selectin expressions were reported when the EC monolayer was exposed to an oscillatory shear flow with zero net flow (0 ± 0.5 Pa at 1Hz) for 6 hours. Similar oscillatory flows with greater rate variation

(0 ± 2 or 4 Pa at 1Hz) showed no influence on cell orientation compared with the static control.[29] In contrast, an elongation pattern in cell morphology was observed when EC monolayers were exposed to a pulsatile sinusoidal flow with (2 ± 4 Pa at 1Hz) or without the reversing flow (4 ± 2 Pa at 1Hz).[29] These results suggest that EC can discriminate among different types of pulsatile flow environments. The pro-inflammatory response in EC indicates that atherosclerotic lesion initiation is likely related to unique signals generated by oscillatory shear stress.

1.4.3. The effect of non-uniform shear field with complex flow profile

Spatial heterogeneity in the phenotype of EC *in vitro* as reported by Chen et al.[30] and White et al[31] can be attributed to changes in shear direction or magnitude within a step flow chamber (Fig. 2 c). The Vertical step flow chamber provides an opportunity to create a spatially heterogeneous shear profile by creating a flow disturbance. Downstream, the flow recovers its steady laminar flow pattern. Several studies were conducted to investigate the impact of spatial variations in the shear field on EC function. White et al. found that the spatial gradient caused by the flow disturbance exerted a minimum influence on cell proliferation compared with the temporal change in shear flow pattern. Chen et al. showed that spatial heterogeneity in the shear field resulted in a differential efficiency in recruiting leukocytes, where the maximum adhesion was observed at the reattachment flow region where the shear stress is nearly zero. However, the shear gradient created by this step flow chamber involves not only a change in shear magnitude, but also a directional change and an even more complex

flow profile that can alter EC function as well.

1.5. Limitations in current shear-regulated EC studies and the future direction

Literature suggests that fluid shear results in differential regulation of CAM transcription that is either pro- or anti-inflammatory in the context of leukocyte recruitment.[15,17,32] *In vivo*, endothelial cell phenotypic heterogeneity is observed over spatial scales on the order of millimeters where disturbed flow profiles can result in an enhanced inflammatory response.[33,34]

Besides further investigation in the fundamental studies of shear flow influence on EC function, the next step would be monitoring the dynamic change in EC function under a spatially- and temporally-varying shear coupled with wall motion as a representative model of realistic shear flow conditions. However, it would impossible to achieve this goal by using the conventional flow chamber shown in Fig. 2. It would be also difficult to obtain an analytical solution for the instantaneous shear field when designing a new flow chamber. Thus, there is an urgent need for a reliable WSS measurement technique for *in vivo* or *in vitro* research that would provide accurate WSS estimates with high temporal and spatial resolution. In addition to creating a complex flow profile that is challenging to generate with available flow chambers, little information is reported about the EC response to intermediate fluid shear or shear gradient without directional change. This underlines the need for understanding the mechanical signal pathways in the EC function and also the importance of identifying

the necessity of improving WSR imaging under certain shear conditions.

1.6. Medical imaging techniques for monitoring vascular hemodynamics

Among the non-invasive medical imaging modalities, only magnetic resonance imaging (MRI)[35] and ultrasound[36] are routinely used to visualize blood flow across the vessel lumen. In large arteries such as the carotid artery and brachial artery, blood viscosity is approximately constant,[37] and therefore WSR imaging that is derived from a spatial velocity profile can be used to estimate corresponding WSS. The accuracy and sensitivity of WSS measurements relies on the accuracy of WSR. Essentially, the challenges for developing accurate WSR measurement techniques fall into three categories: high spatial resolution and velocity sensitivity to measure slow blood velocity near the vessel walls, high temporal resolution to track rapid changes in WSR under unsteady flow situations, and non-invasive capability for frequent clinical applications.

1.6.1. Shear assessment using magnetic resonance phase contrast imaging technique

In MRI, flow velocity distribution in a cross-section of an artery can be visualized as a function of time by placing the artery of interest in a strong static magnetic field (∼1-2T) and modulating the static field with high-frequency magnetic pulses. In this way, a small fraction of the hydrogen atoms are then brought to resonance (∼150

MHz). After adding a gradient field to this static magnetic field, the phase shift of the resonating atoms becomes position dependent. When no flow motion is present, only a linear gradient in phase shift is generated. In contrast, an additional phase shift proportional to the flow velocity is generated when the excited atoms are moving along the direction of the magnetic gradient. The phase shift can be detected using a phase contrast method by comparing the phase shift between a reference scan and a velocity encoded sensitized scan. The velocity is then obtained by multiplication of the observed phase shift with a calibration factor, defined as the aliasing velocity divided by 180 degrees. In order to prevent aliasing and false reading in the velocity estimation, aliasing velocity has to be set greater than the maximum velocity while maintaining a high signal-to-noise ratio for phase assessment for velocity estimation.

Papathanasopoulou et al[38] characterized the performance of MRI phase contrast on WSS measurement by comparing the results with the predicted WSS obtained from computational fluid dynamics (CFD) simulation on a carotid bifurcation model. They found that 3D MRI data show relative good agreement ($\sim$ 20% bias) when measuring high WSS at the uniform shear region. However, MRI was not able to detect high WSS along the divider wall where the flow profile is complex. This limitation may be caused by displacement artifacts due to inadequate phase-contrast pulse sequence and signal loss caused by intra-voxel dephasing in the regions of complex flow. Cheng et al.[39] found the mean absolute error of circumferentially resolved shear stress for the nonaxisymmetric phantom to decrease from 28% to 15% when image resolution (pixel size) was improved from 0.047 to 0.023 mm. In vivo measurements

reported by Oshinki et al.[40] and Wu et al.[35] showed that the values of WSS or WSR are lower in the infrarenal aorta and superficial femoral arteries than other major arteries investigated, where these two arteries are known to have a higher tendency for developing atherosclerotic lesions.

1.6.2. Ultrasound approaches to measuring vascular shear rate.

Non-invasive medical ultrasonic imaging has been the most popular imaging modality for visualizing blood flow patterns[41] and locating plaques.[42] There are several ultrasonic approaches available for velocity and shear rate estimation. Narrow-band Doppler imaging is the most common method for measuring the flow velocity, and it is also the most intuitive way to estimate WSR simply by taking the spatial derivative of the velocity map.[43,44,6] Brands et al. used a modified Doppler velocity estimation algorithm featuring a regularization term depending on the eSNR to reduce noise and estimate WSR from narrow-band Doppler data.[43] The downside of this approach is a relatively poor spatial resolution ($\sim$ 0.2 mm), and therefore it is not suitable for measuring shear rate at the vessel wall. Another common method for estimating velocity ultrasonically is to use a cross correlation estimator and broadband pulsed transmission to calculate the phase shift between ensemble signal pairs. Samijo et al.[45] adapted this method to measure WSR in carotid arteries from the echo data acquired with a 3-cycle, 5.3 MHz pulse. The advantage of using a cross correlation velocity estimator is that the accuracy can be improved by applying a small correlation window, but at the cost of amplification in estimation noise. Another approach

requires special acoustic contrast agents presented in the flow region. Kim et al.[46] used 6.7 MHz broadband pulses and particle image velocimetry techniques to track the flowing contrast agents and construct the 2D flow field. This method is invasive, and the nature of the contrast agents is a major limitation in WSR estimation due to its active response to radiation force generated from the imaging pulses.

In addition to transcutaneous ultrasound, intravascular ultrasound (IVUS) has become more popular in assessing small arteries, especially in coronary studies, due to its higher spatial resolution and low tissue clutter artifacts. Wentzel[47] et al. used a 30 MHz IVUS catheter to access the WSR profile inside the coronary artery. Although IVUS has the advantage of high spatial resolution, it is an invasive procedure that creates a flow disturbance within the targeted artery. A major limiting factor of IVUS is the risks associated with invasive procedures, and thus IVUS is generally only used for advanced diagnosis and guidance of stent placement.

1.7. Comparison between ultrasound and MR imaging

For general medical imaging applications, MRI yields a better soft tissue contrast resolution than ultrasonic imaging. However, for flow imaging, MRI is restricted by long acquisition times and relative poor spatial resolution. Wu et al.[35] reported the scanning time for each measurement is about 3 minutes when acquiring in vivo imaging data. Although the available time resolution can provide 20-32 frames per cardiac cycle by using interleaving and ECG-triggering, the ability to track dynamic change within one cardiac cycle remains limited. The spatial resolution in MRI phase

contrast image is determined by the pixel size and the slice thickness in the direction that is perpendicular to the imaging plane. For blood flow velocity imaging, spatial averaging is required in MRI to suppress estimation noise, and that results in a degradation in spatial resolution to 1-2 mm while the slice thickness is generally 4-8 mm.[37] Higher spatial resolution is achievable by reducing the slice thickness or pixel size but at the cost of signal power.[48]

In contrast, ultrasonic imaging is known for delivering real time information safely and at low cost. Similar to MRI, it requires tradeoffs between spatial resolution and transmitted signal power. Generally, ultrasonic flow imaging transmits a narrow-band Doppler pulse sequence to improve eSNR. Thus instead of choosing the shear rate value at the vessel wall to determine the instantaneous WSR, the maximum of the radial derivative of the velocity profile is selected. Due to limited spatial resolution, the maximum shear rate is normally assessed at 250-300 μm from the blood-intima boundary.[37]

Overall, ultrasonic flow imaging has the ability for real-time imaging and therefore it has a better potential to monitor the dynamic changes in vascular hemodynamics.

1.8. Methods to improve ultrasonic shear imaging

As mentioned previously, the accuracy and precision of ultrasonic WSR estimates is limited by tradeoffs between the signal power and spatial resolution.[37,49] Long duration narrow-band pulses reduce velocity errors in uniform flows by increasing eSNR,[50] while short broadband pulses improve spatial resolution.[51] Long pulses

produce spatial blurring that biases velocity estimates and results in large systematic WSR errors ($\sim$28%[52]). The other way to reduce WSR variance is to increase the packet size,[53] but the loss in temporal resolution reduces WSR measurement accuracy. Fig. 3 shows that the shear rate for laminar flow is greatest at the EC surface where blood velocity V is minimum. However, the measured velocity profile is blurred by the estimation process, thus velocity gradient estimates, and consequently shear rate estimates, are biased. The bias is greatest at the lumen surface, where WSR influences EC function. The bias can be reduced by increasing the pulse bandwidth and shortening the echo window used to localize velocity estimates, at the cost of the sensitivity to blood echoes. Though eSNR can be improved by increasing the transmitted sound pulse amplitude while maintaining the signal broad bandwidth without elongation, most commercial scanners are already nearing the mechanical index safety regulatory limit at 1.9.

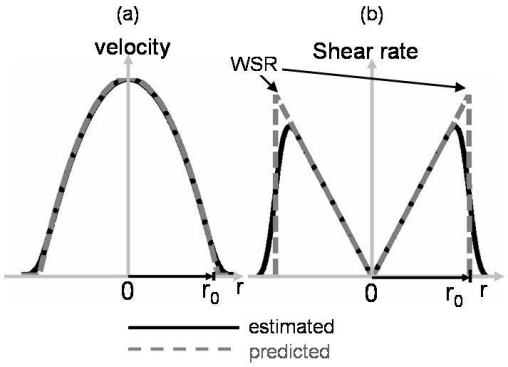

Figure 3. Predicted and measured WSR profiles. of (a) flow velocity and (b) shear rate magnitude across a laminar flow channel of radius r_0. Wall shear rate (WSR) is measured at channel $r = r_0$

In summary, both conventional broadband and narrow-band ultrasound systems have disadvantages in terms of accuracy and precision for WSR estimation. Therefore the important question is how to obtain accurate WSR estimates from a low eSNR and band-limited signal, especially when the region of interest is highly non-stationary in space.

The literature has shown it is possible to improve the accuracy of WSR estimates by deconvolving the velocity acquired from Doppler data with the intensity function of the transducer.[54,52,55] However, this method is very sensitive to the velocity estimation noise and velocity profile shape. The quality of velocity estimations with Doppler techniques depend mainly on the wall filters whose performance is generally based on the signal separation between the blood and the vessel wall in both Doppler frequency (velocity) and signal energy domains. However, near the vessel wall, blood velocity is very slow and roughly equal to pulsatile vessel wall motion due to the non-slip condition. Thus, the overlap in Doppler frequency limits the wall filter's ability to preserve low blood flow velocity at the intima-blood interface. Bias in velocity estimate can lead to severe distortion in WSR estimates when applying this type of deconvolution method.

1.9. Coded excitation to achieve high spatial resolution and high signal power flow imaging

Conventional uncoded systems transmit pulses with a constant time-bandwidth product (TBP), which equals to 1. In this way, narrow-band pulses yield high signal power

while broadband pulses exhibits the opposite. In contrast, coded-excitation techniques, originally developed for radar tracking, generate long-duration pulse sequences that have a TBP greater than one.[56,51] This feature increases the time-averaged signal energy without increasing the spatial-peak acoustic intensity or mechanical index. By applying a decoding filter to the received echoes, the pulse is then compressed to restore spatial resolution while preserving the enhanced eSNR. Ideally, the eSNR gain equals the TBP from coded transmission of the imaging pulse.[57] It is common to see coded excitation techniques implemented onto ultrasound systems mainly for the purpose of improving the penetration depth in 2D Bmode imaging.[58,51] Liu et al.,[57] Pedersen et al.[59] and Wang et al.[60] further utilized coded-pulse excitation techniques in ultrasonic elastography, flow and IVUS flow imaging, and showed promising results.

Considering that blood flow imaging and vascular WSR imaging are derived from the same measurement, we proposed to adapt the coded-pulse excitation techniques for WSR imaging. The high spatial resolution of B-mode imaging along with the enhanced eSNR of color flow imaging so as to facilitate velocity measurements very close to vessel walls.

Pulse codes, in general, can be sorted into three different categories: linear frequency-modulated (FM),[59] non-linear FM[61] and phase modulated (PM) codes.[61,57] The choice of codes and code lengths depend on the imaging task, but all codes have the same advantage in transmitting large time-averaged power without increasing the peak instantaneous power that may pose safety risk. The minor side effect is the contrast resolution may be degraded during the decoding process due to the production

of sidelobes.[56]

The challenge for WSR imaging is to obtain accurate and precise velocity measurements near the vessel wall with spatial resolution of B-mode imaging. In order to achieve this goal, a cross correlator that provides more precise velocity calculation is selected.[62] With higher eSNR, a smaller cross correlation window can be applied to reach high spatial resolution in velocity mapping and minimize bias in both velocity and shear rate measurements.[45] However, for transmission frequencies less than 20 MHz, the difference in echo amplitudes measured inside (blood) and outside (tissue) the lumen is large enough to generate inaccurate velocity estimates to bias shear rate estimates. Therefore, a method that minimizes the amplitude difference between blood and tissue is also proposed to work with the cross correlator.

1.10. Scope

The intention of this dissertation is to demonstrate a new ultrasonic method that can provide high quality ultrasonic WSR imaging, and to study the influence of ultrasonic measurement errors on registering the shear-mediated biological response to the corresponding WSS. The central chapters of this dissertation address both the engineering and biological aspects. Chapters on the engineering aspect involve the design and evaluation of the ultrasound methods for both *in vitro* phantom experiments and *in vivo* studies. The chapters representing the biological aspect of this dissertation show the detailed studies in shear-regulated endothelial function on cultured human aortic endothelial cells. At the end, these two elements are brought together to predict the

effect of ultrasonic WSR estimation errors on the determination of shear-mediated endothelial function and associated inflammatory response.

2. ULTRASOUND SIMULATION MODEL AND PROCESSING ALGORITHM

2.1. Objectives

This chapter describes the image processing algorithm for ultrasonic shear rate imaging. It covers the excitation pulse sequence design and off-line processing methods for shear rate estimation. A signal model that simulates the acoustic environment of an adult carotid artery is developed using the same experiment parameters used in our in-house ultrasonic system. The simulation results help to guide the system design and processing techniques by evaluating the system performance in WSR estimation under different simulated conditions.

2.2. Ultrasonic wall shear rate estimation algorithm

An outline of our 2D ultrasonic shear rate imaging technique is illustrated in Fig. 4. First, a voltage waveform, created from a function generator, is used to drive the ultrasound probe to transmit an acoustic pulse toward the imaging target. If coded pulses are used, the received echo signals are then decoded to restore spatial resolution. All echo signals are conditioned prior to the velocity estimation step to minimize tissue clutter artifacts. A modified velocity estimator is applied to calculate the velocity profile. The WSR value is finally obtained by taking the spatial derivative of the velocity estimates at the vessel wall.

The challenges in designing a better ultrasound shear rate imaging algorithm are

finding methods to improve spatial resolution while maintaining high eSNR, creating filters to reduce tissue clutter artifact without biasing the flow estimation, and selecting velocity estimators that provide robust velocity estimates.

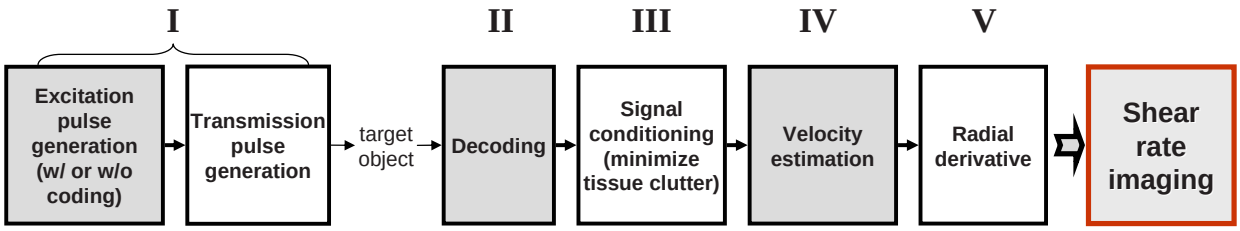

Figure 4. Ultrasonic wall shear rate imaging algorithm

2.3. Simulation model and detailed image processing algorithm

A simulation model based on our in-house ultrasonic system was constructed to efficiently evaluate the imaging method prior to system implementation and flow experiments. In most ultrasonic imaging systems, a single frame 2D B-mode image is assembled from several lines of 1D echo A-line signals. In situations where the vessel lumen is much larger than the ultrasonic beam width, the variation in lateral velocity inside the ultrasonic beam becomes negligible. An 1D signal model is sufficient for simulating the ultrasonic echo acquisitions in such flow conditions. The lateral beam width of the transducer used in the simulation is 225 μm. This simulation model, as shown in Fig. 5, closely describes our experimental system design and serves as a

general outline of the simulation and experimental methods.

A discrete-time voltage waveform $e[m]$ is applied to the transducer to generate the pulse-echo point spread function of the ultrasonic system h. Echo data g are generated through a linear transformation of the object f via h. The echo data from coded transmissions are filtered to compress the pulse sequence and produce decoded echoes g_d. The results are amplitude equalized before velocity and WSR are estimated. Each of these processes is described below.

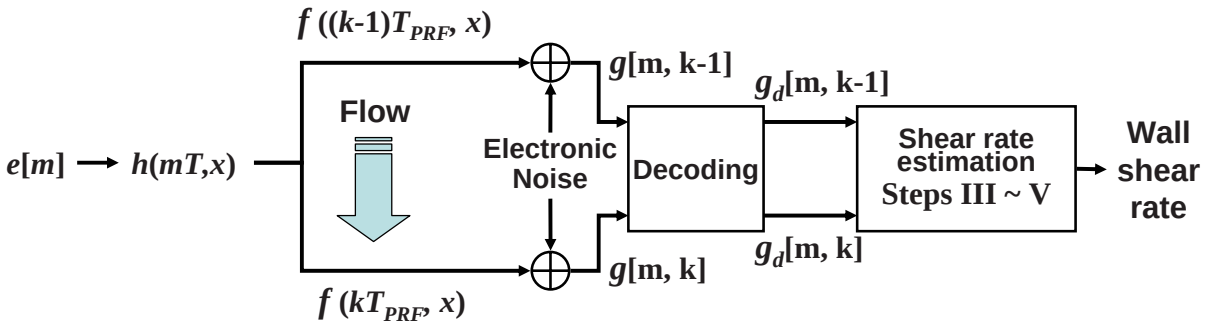

Figure 5. Echo signal model with flow.

2.3.1. Step I: Excitation pulse generation

The spatiotemporal point spread function of the imaging system is the temporal convolution of the voltage waveform e and the pulse-echo impulse response of the system h_s; That is, $h(mT, x) = \sum_{m'=-\infty}^{\infty} e[m - m']h_s(m'T, x)$, where time is uniformly sampled and $0 \leq m \leq M - 1$. RF echo signals are sampled on the time interval T, such that $t = mT$ for integer m. Echo ensembles are acquired on the pulse repetition

interval T_{prf}, such that $t_s = kT_{\text{prf}}$. Since $T_{\text{prf}} \gg T$, t is called fast-time and t_s is slow-time. The pulse repetition frequency PRF $= 1/T_{\text{prf}}$. Two groups of excitation pulses are included: (a) standard uncoded pulses with TBP of 1. Both broadband and narrow-band Doppler pulses were used; (b) coded pulses with TBP > 1, including phase modulated (PM) and frequency modulated (FM) coded pulses.

(a) Uncoded pulse sequences:

Various lengths of uncoded pulses are widely used in conventional ultrasonic systems for different imaging applications. These pulses share the same characteristic of having a constant TBP=1. This means that when the pulse length increases, the bandwidth narrows, which leads to degradation of spatial resolution. In general, long pulses have a better tracking of flow signals from weak blood scatterers due to greater signal energy. Although, higher pulse energy for a short broadband pulse can be achieved by increasing pulse amplitude, the maximal amplitude is limited by Food and Drug Administration regulation. Consequently, there are always tradeoffs in the choice of pulse length between approaching high spatial resolution and higher eSNR. In this section, a 1-cycle broadband and a 5-cycle narrow-band Doppler pulses were both implemented in the study to compare the importance of bandwidth and eSNR in WSR estimation.

(b) coded pulses

A variety of codes are available for applications in the ultrasonic systems. Difficulty

in code generation, peak to side lobe ratio (Lp/Ls) after pulse compression and processing complexity are the determining factors for the choice of codes.

PM coded pulse sequences: For digital systems, binary PM codes are easier to be implemented. The general form of a phase coded signal can be express as Eq. 4.[63]

$$e(t) = \sum_{n=1}^{N} a_n \Pi_n(t/\tau) e^{j(\omega_0 t + \phi_n)}, \tag{4}$$

where a_n is the amplitude of the nth binary element of duration τ, and ϕ_n is the corresponding phase. N is the code length defined by applying a temporal window Π.

$$\Pi_n(t/\tau) = \begin{cases} 1 & \text{for } (n-1)\tau \leq t \leq n\tau; \\ 0 & \text{elsewhere.} \end{cases} \tag{5}$$

There are three major groups of phase codes:

Group A: a_n=1 and $\phi_n = 0$ or π;

Group B: a_n=1 and ϕ_n varies with n;

Group C: a_n and ϕ_n varies with n.

Group B codes, such as polyphase codes,[64] are hard to implement at MHz operating frequencies. Therefore, they are not practical for medical ultrasonic imaging applications. Group C codes have shown a significant increase in Lp/Ls ratio.[65] However, they are very sensitive and small errors, which reduces the Lp/Ls ratio.

Relatively speaking, group A codes have the advantages of easy implementation, stability and high Lp/Ls ratio after pulse compression. Thus, group A codes are most suitable for medical ultrasound applications.

The common codes in group A include Barker codes,[66] optimal codes,[67] Golay,[68] [69] and maximal length sequence (M-sequence).[63] Though Barker codes are very popular in radar systems, they show relatively lower Lp/Ls ratio, and the highest available code length is only 13 bits, which limits its highest Lp/Ls ratio and highest TBP. Both M-sequence and Golay used in our preliminary studies were not further investigated for the reason stated below. The pseudorandom binary sequence structure of M-sequence is very similar to random sequences and therefore has the advantage of approaching an ideal imaging system impulse response after pulse compression. However, the random noise property creates nulls in the frequency spectrum. The nulls make the signals more sensitive to system noise and therefore limit the choices of decoder.[63] Golay codes are pairs of complementary binary codes. Though this type of code can completely eliminate sidelobe artifacts, the perfect impulse can only be achieved while imaging stationary objects. In a normal physiological environment with rapidly changing blood flow and tissue movements, this type of coding would amplify sidelobes significantly. Also there is a need to double the number of pulses transmitted, and consequently the frame rate is halved. Therefore, Golay is not suitable for tracking vascular blood flow.

Optimal codes[67] were finally selected for our study because of their spectral properties and ease of implementation. They are optimal in the sense that they give the

flattest spectral response in the bandpass of the transducer.[61] A flat frequency spectrum means that matched or inverse filtering applied for pulse compression (decoding) yields comparable results, thus suppression of side lobes and noise amplification are balanced. Biphasic PM codes are of particular interest because they can be implemented on many clinical systems with minimal modifications.

Detector sensitivity is improved at the cost of reduced axial resolution by convolving a binary PM code $c[m]$ with a binary base sequence $b[m]$.[51] To facilitate this process, biphasic PM codes $c[m]$ are expanded in time by the integer factor $S > 1$ to match the sampling rate of the pulse generator, $c_e[m] = \sum_{m'} c[m']\delta[m - m'S]$. Assume the sampling interval of the pulser and receiver are both T. Then the voltage waveform driving the transducer is the temporal convolution

$$e[m] = \sum_{m'=-\infty}^{\infty} b[m - m']\, c_e[m'] \; . \quad \text{(PM code)} \tag{6}$$

An example of an 8-bit Optimal code sequence and the generated excitation waveform is illustrated in Fig. 6. The binary sequence of the Optimal codes used in this simulation are listed in Table 1.

FM chirp pulses:

In our experimental ultrasonic system, an arbitrary waveform generator is used to create excitation voltage waveforms. Therefore, it is possible to implement a FM code such as a linear chirp that requires more than binary control in waveform amplitude. In the simulation, we followed the general technique of Misaridis et al.[70] to generate

Table 1. Optimal code sequence

length of code N	code
3	-1-11
5	-1-1-11-1
7	-1-1-111-11
8	-1-1-111-11-1
10	-1-111-11-1-1-1-1
13	-1-1-1-1-111-1-11-11-1
15	-1-1-1111-1111-111-11

a linear FM chirp sampled on the interval T:

$$e[m] = w_c[m]\ \cos(2\pi((u_0 - \Delta u/2)mT + \alpha(mT)^2))\ , \quad \text{(FM code)} \tag{7}$$

where α is the slope of the frequency sweep in MHz/μs, u_0 is the center frequency, Δu is the bandwidth, and $w_c[m]$ is a 10% cosine taper window function of duration T_p,

$$w_c[m] = \begin{cases} 1 - \cos^2 5\pi mT/T_p & 0 \le m \le T_p/10T \\ 1 & T_p/10T \le m \le 9T_p/10T \\ 1 - \cos^2 5\pi(mT - T_p/5)/T_p & 9T_p/10T \le m \le T_p/T \end{cases} \tag{8}$$

w_c is applied to suppress the range side lobe level of the compressed pulse by 2 dB compared with a rectangular window but with some broadening of the pulse length after matched filtering. Spatial resolution is traded for side lobe suppression. In our simulations, $\alpha = 1.0508$ MHz/μs and $T_p = 2.855\mu$s. Pulses were simulated with

$u_0 = 10$ MHz, and the fractional bandwidth was 60% so that $\Delta u/2 = 3$ MHz. The generated chirp waveform is plotted in Fig. 6(d).

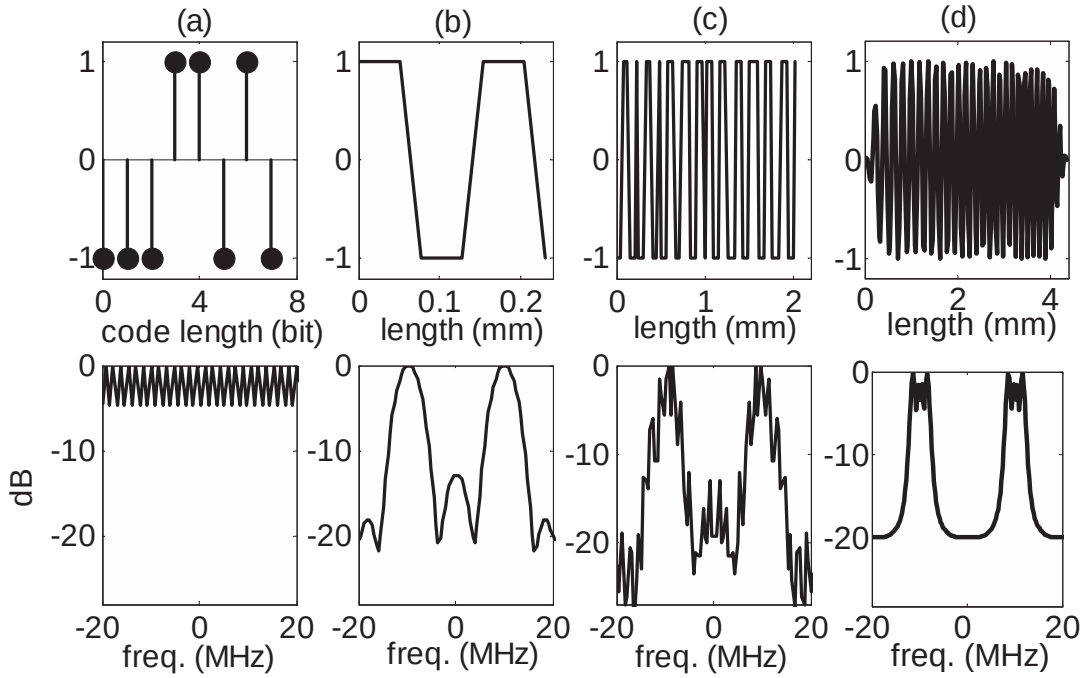

Figure 6. Coded pulse examples. Top row shows (a) an 8-bit Optimal code, (b) typical base sequence, and (c) their convolution resulting in the excitation voltage waveform. (d) Frequency-modulated coded (chirp) pulse. Bottom row shows the corresponding frequency spectra.

2.3.2. Simulated echo signal generation

The frequency range used in most conventional external medical ultrasonic systems for imaging vascular flow is between 7 and 10 MHz. Based on its penetration depth and accessibility, carotid arteries are the most common arteries for ultrasonic blood flow scans. Therefore, echo signals were generated in our simulation study to mimic

the acoustic environment in an adult common carotid artery. The object scattering function f and noise process n are modeled as random functions of space x and slow time $t_s = kT_{\text{prf}}$.[71] Both were drawn from wide-sense stationary, white Gaussian noise (WGN) processes, except that the magnitude of f was adjusted spatially to create tissue echoes in simulations that were 25 dB greater in amplitude than the intraluminal blood echoes. Depth-dependent signal losses through 2 cm of tissue were simulated by applying frequency dependent attenuation $\beta = \beta_0 f x$, where $\beta_0 =$ 0.5 dB cm^{-1}MHz^{-1} and assuming the attenuation within blood is minimum and can be neglected. For each data point reported, 150 statistically independent pairs of echo waveforms ($g[m, k-1]$ and $g[m, k]$ in Fig. 5) were generated for analysis. Only scatterer movements parallel to the ultrasonic beam axis were simulated in this 1D model. For a fully developed pipe flow model without secondary flow, a parabolic profile similar to the flow field inside the single channel flow phantom was used to describe general moving patterns of blood scatterers. Axial motion was generated by moving blood scatterers $f(x, t_s)$ in x for each $t_s = kT_{\text{prf}}$. For discrete x, sub-sample motion is achieved by spline interpolation. The moving object function at ensemble pulse k can be expressed recursively:

$$f(x', kT_{\text{prf}}) = f(x, (k-1)\,T_{\text{prf}}) \qquad \text{for } \; k > 0\;, \tag{9}$$

where $x' = x + \triangle x$, $\Delta x = V(x, (k-1)\,T_{\text{prf}}) \times T_{\text{prf}}$, and $V(x, t_s)$ is the x-axis component of scatterer velocity. Scatterer displacement varies with position according to the model adopted for vascular flow.

The mth echo sample recorded from the kth ensemble pulse, $g[m,k]$, is modeled through the continuous-to-discrete integral transformation,

$$g[m,k] = \int_{-\infty}^{\infty} dx'\ h(mT,x') f(x', kT_{\rm prf}) + n[m,k]\ . \tag{10}$$

$g[m,k]$ is the sequence of radio frequency (RF) echo data for a single line of site: m is the index for samples in fast time and k is the index for the waveform ensemble in slow time. We can simulate a two dimensional flow data (i.e. color flow image on conventional medical ultrasonic system) by increasing the dimensionality, $g[m,k,q]$, where q is the index indicating acquisition of an echo ensemble at lateral position $y = q\Delta y$.

Eqs. 9 and 10 are related to Eq. 1 through V. Assuming a Newtonian fluid is flowing steadily in a long rigid channel without slipping at the walls, a laminar flow profile is generated with the radial velocity given by[36]

$$V(r) = \begin{cases} V_{max}(1 - \frac{r^2}{r_0^2}) & r < r_0 \\ 0 & r \geq r_0 \end{cases}\ .$$

Therefore Eq. 1 gives

$$\text{WSR} \ = \ -2V_{max}/r_0\ , \tag{11}$$

where V_{max} is the spatial peak velocity. For many applications the minus sign is ignored. The beam axis can be positioned so that the laminar flow limits scatterer motion to the image plane and thus echo decorrelation is minimal.

Flow parameters for simulations were chosen to match the experiment settings: a 5-mm-diameter flow channel with $V_{max} = 500$ mm/s imaged at 72^o Doppler angle

with PRF = 5 kHz. The true WSR for this simulated data is 400 s^{-1}, which is in the normal range for mean WSR in carotid arteries[6] assuming the blood viscosity is a constant around 4 mPa-s.[37] As V_{max} varies, PRF is adjusted so that $V_{max}T_{\rm prf} = 0.1$.

2.3.3. Step II: Decoding for pulse compression

In simulation, the entire process including system parameters and pulse generation is well-defined. In this case, a Wiener filter that requires a better understanding of the pulse characteristics can be used to decode the pulse and restore the spatial resolution. The advantage of using a Wiener filter is that the noise can be effectively suppressed while recovering the highest possible bandwidth and minimizing sidelobes.

The Wiener filter $w[m]$ applied to noisy echo waveforms $g[m,k]$ is given by $g_d[m,k] = \sum_{m'} w[m-m']\, g[m',k]$. If successful, spatial resolution is restored and eSNR is enhanced. The frequency response of the Wiener filter is

$$W[\ell] = \begin{cases} C^*[\ell]/(|C[\ell]|^2 + \gamma/\overline{\rm eSNR}[\ell]) & \text{(PM code)} \\ E^*[\ell]/(|E[\ell]|^2 + \gamma/\overline{\rm eSNR}[\ell]) & \text{(FM code)} \end{cases}, \tag{12}$$

where $C^*[\ell]$ is the complex conjugate of the discrete Fourier transform of the code sequence $c[m]$ and $\overline{\rm eSNR}[\ell]$ is a frequency domain representation of the echo signal-to-noise ratio described below. The index ℓ is related to the continuous frequency variable u via $u = \ell/MT$. Notice that the transmitted voltage waveform e is used to filter FM coded signals while the code without the base sequence c is used to filter PM coded signals. γ is a regularization constant that we set to 0.4 in this study. For low-noise echo waveforms, i.e., when $|C[\ell]|^2 \gg \gamma/\overline{\rm eSNR}[\ell]$, the first term in the

denominator dominates the response and the Wiener filter approximates an inverse filter. Noisy data increases the magnitude of the second term in the denominator such that the Wiener filter is essentially a weighted matched filter. To understand this weighting, we must define eSNR in the spatial and frequency domains.

Spatial domain: Recall that object scatterers and additive noise are assumed to be zero-mean, WGN processes. Consequently eSNR(x) is given by the associated variances σ_f^2 and σ_n^2 and the shift-varying point spread function (psf) measured after decoding h_d,[57]

$$\begin{aligned} \mathrm{eSNR}(x)(\mathrm{dB}) &= 10\log\frac{\sigma_f^2}{\sigma_n^2}\int dt\; h_d^2(mT|x) \\ &\simeq 10\log \mathrm{TBP} + \mathrm{eSNR}'(x)\;. \end{aligned} \tag{13}$$

eSNR (coded excitation) exceeds eSNR$'$ (short-duration Gabor pulse) by an amount related to the time-bandwidth product of the code for equal-amplitude pulses. For TBP = 1 pulses, eSNR$'$ increases with pulse length at the cost of bandwidth. However coding provides the possibility of fixing eSNR$'$ and bandwidth and then increasing eSNR by lengthening the code since code length is approximately proportional to TBP for most PM codes.

For known component variances, as in simulations, Eq. 13 is implemented by placing a point reflector at x. Applying $f(x', t_s') = \delta(x' - x, t_s' - t_s)$ to Eq. 10 and ensemble averaging over noise, $\mathcal{E}\{\cdot\}_n$,[57]

$$h_d(mT|x) = \mathcal{E}\{g_d[m,k]\}_n.$$

For unknown component variances, as in experiments, we measure the net sample variance of decoded echo signals $\hat{\sigma}^2_{g_d}$ in a homogeneous scattering region and $\hat{\sigma}^2_n$ in a scatterer-free region, and then we approximate

$$\mathrm{eSNR}(x) \simeq 10 \log(\hat{\sigma}^2_{g_d}/\hat{\sigma}^2_n - 1). \tag{14}$$

Frequency domain: $\overline{\mathrm{eSNR}}$ is the ratio of power spectra for the noise-free echo signal and the noise alone at position x,

$$\overline{\mathrm{eSNR}}[\ell] = \frac{\mathcal{E}\left\{|\mathcal{E}\{G_d[\ell,k]\}_n|^2\right\}_f}{\mathcal{E}\{|N[\ell]|^2\}} = \frac{|H_d[\ell]|^2 \mathcal{E}\{|F[\ell,k]|^2\}_f}{\mathcal{E}\{|N[\ell]|^2\}} \ . \tag{15}$$

Of course, to compute the Fourier transforms, we assume there exists an analysis region in signal space where f is wide-sense stationary and h_d is shift invariant. Ensemble averages on the far right of Eq. 15 are constant over frequency and proportional to the corresponding variances. By summing over frequency and invoking Parseval's formula, it is easy to show that $\mathrm{eSNR}(x) = 10 \log \sum_\ell \overline{\mathrm{eSNR}}(\ell/MT)$. Eq. 15 is more general than Eq. 13 since it holds for nonwhite random processes.

2.3.4. Step III: Signal conditioning to minimize tissue clutter influence

By focusing on time-domain cross correlation (CC) measurements of slow velocity for broadband signals, as we did, clutter filters are not applicable. However, velocity estimation is challenged significantly by echo nonstationarity; e.g., when there is a difference in mean echo amplitudes inside and outside the lumen. The problem is that displacements estimated using CC estimators can be unbiased only for wide-sense stationary random processes. When the correlation window straddles the vascular

wall, displacement estimates are influenced by motion of wall echoes more than motion of blood echoes because of the greater amplitude of wall echoes. This effect appears in the color-flow format of Fig. 7(a) as an apparent loss of the steady flow near the motionless phantom wall.

To minimize this loss of motion sensitivity, we precondition g_d echo signals by equalizing the RF echo intensity across the flow channel. Like depth-gain compensation, tissue equalization (TEQ) applies a spatially varying gain to the echo signal before correlation to equalize signal variance. As shown in Fig. 7 (b), much of the low flow is restored. The amplitude distortions from TEQ are acceptable since we are only interested in the signal phase. Furthermore, TEQ does not change eSNR(x). When the bandwidth of the pulse and the PRF are set high enough so that scatterer displacements over the interval T_{prf} were smaller than the speckle correlation length, TEQ generated no velocity bias.

2.3.5. Step IV: Velocity Estimation

Accurate and precise estimates of WSR require that there be minimal velocity variance and bias in the low flow-velocity range. Hoeks et al.[62] showed that CC estimators outperform the commonly used autocorrelators at measurements of low flow velocity. Fig. 8 (left) shows the velocity profile estimated from one set of simulation data processed with different CC window lengths. Velocity bias is most significant near the wall. Small CC window lengths reduce the velocity bias without significantly increasing velocity variance at high eSNR ($\geq$ 30 dB). The negative bias from spatial

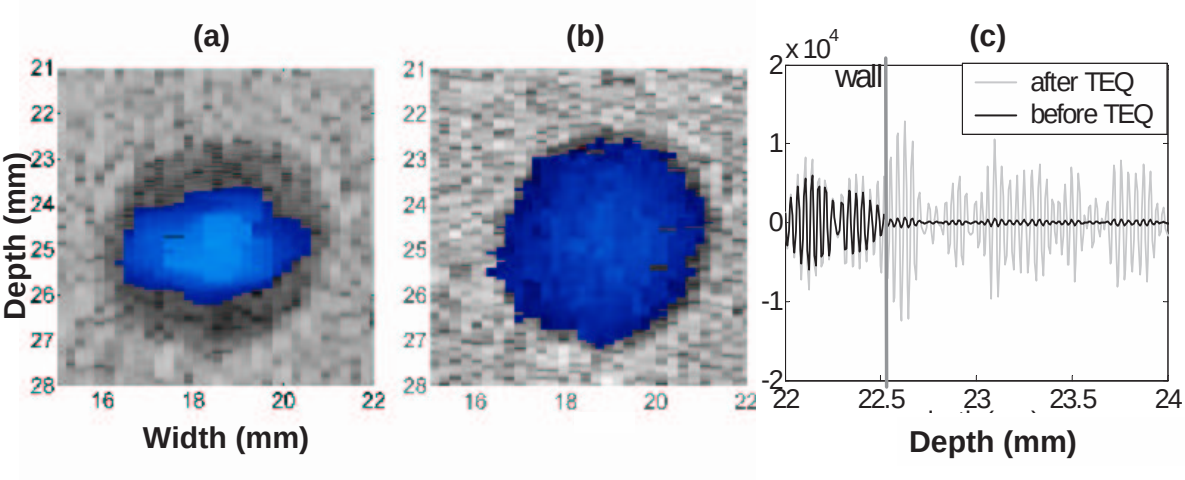

Figure 7. Color flow images from the CC estimator (a) without and (b) with TEQ processing. (c) The radio frequency (RF) signals before and after tissue equalization (TEQ).

averaging indicates that WSR is usually underestimated. Fig. 8 (right) shows that narrow-band pulses and long duration CC windows yield high WSR bias.

Because WSR is computed from the derivative of velocity, it is highly sensitive to random errors. We developed a broadband velocity CC based estimator with a regularization term that minimizes WSR variance without spatial averaging that would reduce resolution.

First, displacements (measured in pixels) are found by minimizing two signal energy terms in the objective function

$$\hat{d}[m_0, q] = \arg\min_d \left\{ \left| 1 - \frac{\hat{\phi}_{m_0,q}[d]}{(\hat{\phi}_{m_0,q})_{max}} \right|^2 + \xi(|d_{fit}[m_0, q] - d|^2) \right\} , \tag{16}$$

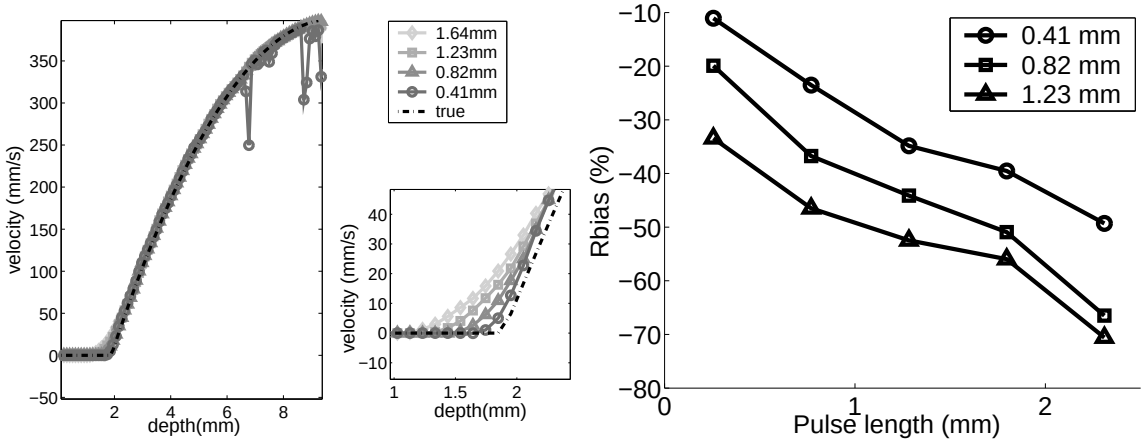

Figure 8. (left) Estimated velocity profiles using a standard short pulse (0.12 mm) and various correlation window lengths. Inset: zoom near the wall. eSNR = 30 dB. (right) Relative bias in WSR estimates for various pulse lengths and three CC window lengths. eSNR = 30 dB.

where the cross correlation function is

$$\hat{\phi}_{m_0,q}[d] = \sum_{m \in CCwindow} g_d[m, k-1, q]\, g_d[m-d, k, q] \ ,$$

ξ is a constant, and m_0 indicates the center sample of the correlation window. The first term on the right side of Eq. 16 depends on the echo data; it is based on the 1D estimate $\hat{\phi}$ that yields minimally-biased but noisy displacement estimates when a small CC window is applied. The second term is based on conventional color flow estimates over the vessel lumen to suppress noise from the data. Color flow estimates are accurate near the center of an artery where blood velocity is high. So we fit color-flow velocity estimates to a second order polynomial, subject to the constraint

$V(r_0) = 0$, to find $d_{fit}[m_0, q]$. By minimizing the difference between d and d_{fit}, weighted by the constant ξ, we reduce variance of velocity estimates. To prevent undesired bias in the estimates, *a priori* knowledge of the flow profile d_{fit} is required. To estimate sub-sample displacements, either g_d is upsampled before correlation or $\hat{\phi}$ is interpolated. The former does not bias displacement estimates while the latter does. In our study, $\xi = 0.6$.

Velocity estimates $\hat{V}$ are computed from the unitless displacement estimate $\hat{d}$ using the standard pulsed Doppler equation,

$$\hat{V}[m_0, q] = \frac{cT}{2\cos\theta T_{\text{prf}}}\,\hat{d}[m_0, q]\ , \tag{17}$$

where θ is the Doppler angle. This algorithm is only applied to positions in the lumen near vessel walls. To obtain accurate velocity estimates, most of the flowing scatterers must stay within the ultrasound pulse during the measurement time T_{prf}. Echo coherence is maintained by carefully adjusting the PRF. Finally, WSR is calculated from the radial slope of Eq. 1 at the channel wall location. When the vessel walls are nonstationary, a tracking method based on a border detection technique and velocity distribution[72] would be implemented to accurately locate the vessel walls.

2.3.6. Step V: Vascular shear rate estimation obtained through radial derivative

Shear rate is the spatial derivative of velocity along the vessel radius. Generally a linear array ultrasound probe is used to image the blood vessels. Therefore, the

received echo data is in a uniformly sampled grid format. In this case, an position-dependent 2D interpolation with respect to the center of the lumen is required. The shear rate values are then obtained by taking the spatial derivative of the velocity map, as shown in Fig. 9. For simulation data, the 1D signal ensembles were assumed to be acquired at the center line of the cross sectional plane of the vessel and therefore only axial derivative is needed. The 2D method is developed for 2D data acquired from in-house or conventional systems.

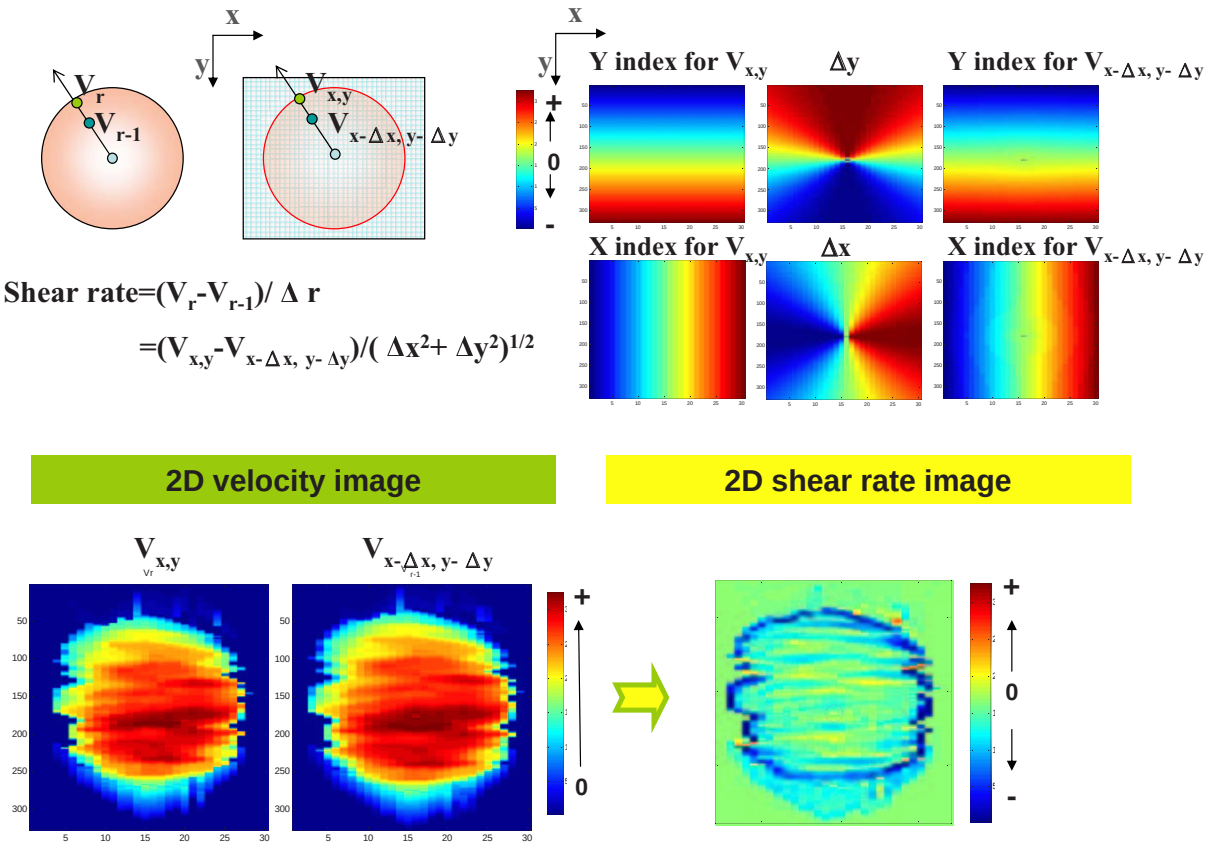

Figure 9. Method to obtain vascular shear rate image by taking radial derivative of a 2D velocity map.

2.3.7. Evaluation metrics

WSR estimation performance is evaluated based upon the bias and standard deviation of estimates. Relative percent bias is defined in terms of the ensemble mean of the values estimated $\widehat{\mathrm{WSR}}$ and predicted WSR:

$$Rbias = \frac{\mathcal{E}\left\{\widehat{\mathrm{WSR}}\right\} - \mathrm{WSR}}{\mathrm{WSR}} \times 100\%;, \tag{18}$$

where WSR is given by Eq. 11. Relative percent standard deviation is found from

$$Rstd = \frac{\left(\mathcal{E}\left\{\widehat{\mathrm{WSR}}^2\right\} - \mathcal{E}^2\left\{\widehat{\mathrm{WSR}}\right\}\right)^{1/2}}{\mathrm{WSR}} \times 100\%;. \tag{19}$$

2.4. Simulation results

Fig. 10 shows the WSR errors for uncoded pulses estimated from simulated data with different CC window lengths. Values are plotted as a function of uncoded pulse length where pulse amplitudes are held constant. For pulses longer than 0.5 mm, WSR biases increase and random errors decrease as transmission pulses lengthen. When the axial pulse length is less than 0.5 mm, eSNR is so low that it is impossible to obtain reliable displacement estimates via cross correlation. Therefore systematic and random errors both increase significantly; the effect is greater for shorter CC windows. The negative bias is caused by the spatial averaging within the CC window and WSR estimation window.

Fig. 11 shows WSR systemic and random errors for three pulse types as a function of eSNR. Other parameters are held constant. Coded pulses reduce WSR errors only

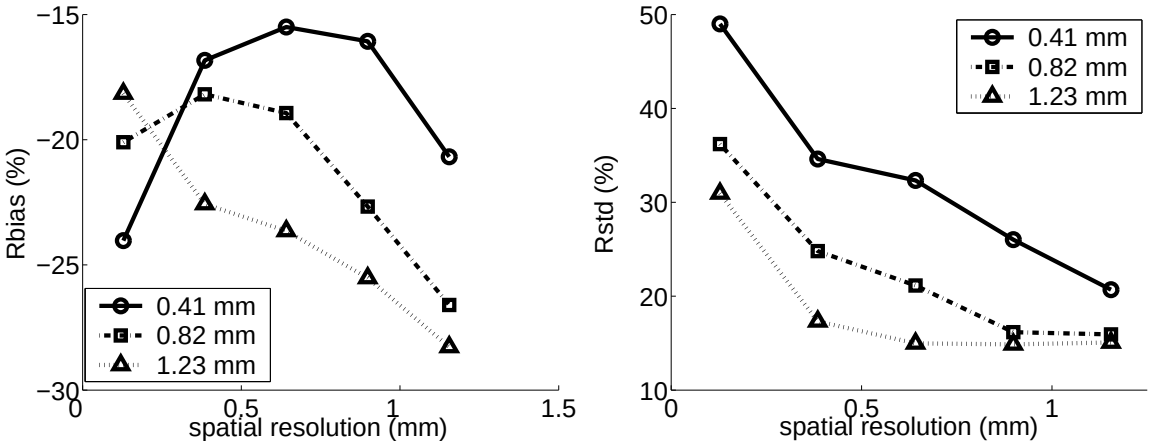

Figure 10. Wall shear rate (WSR) errors for various uncoded pulse lengths and cross correlation (CC) window sizes.

for eSNR < 30 dB. Biases converge when eSNR > 30 dB to a value that depends on the particular CC window size and pulse bandwidth selected.

For subsequent simulations, we selected eSNR = 25 dB as a reasonable representation of clinical scanning conditions on carotid arteries. Other values selected for comparison are a 1-cycle broadband pulse ($\sim$0.1 μs), a 5-cycle narrow-band pulse ($\sim$0.5 μs), a 2.85 μs chirp, and Optimal coded pulses ranging in duration from 3 bits (0.45 μs) to 15 bits (2.25 μs). The amplitudes of all pulses were similar. The voltage waveform energies of the FM chirp and 8-bit Optimal codes were equal although their lengths were not, i.e., 2.85 μs and 1.2 μs, respectively. The FM pulse, consisting of sinusoids, has a lower energy density than the PM pulse, consisting of square waves. Passing the voltage waveforms through the transducer bandwidth produced acoustic pulses where the energy of the FM chirp exceeded that of the PM code by 20%.

Fig. 12 shows that both types of coded pulses increase eSNR; there is a 6.5 dB gain

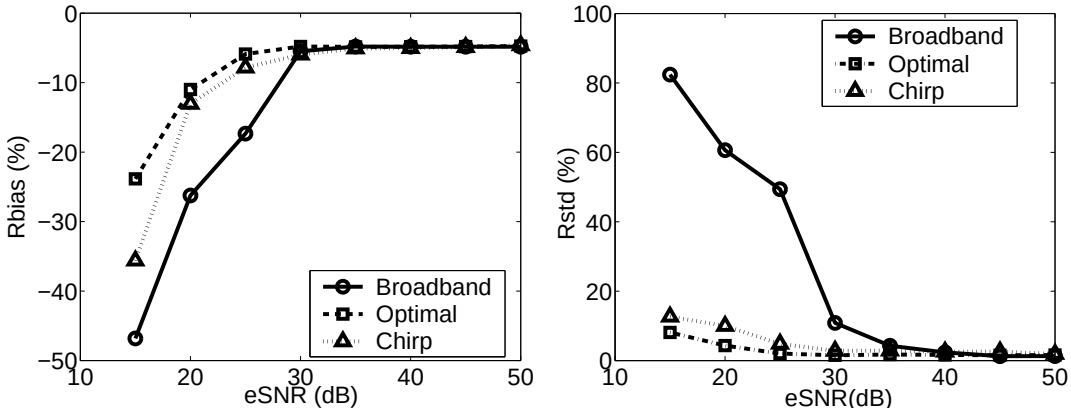

Figure 11. Wall shear rate (WSR) errors for an uncoded broadband pulse, frequency-modulated (FM) coded pulse, and 8-bit Optimal phase-modulated (PM) coded pulse versus echo signal-to-noise ratio (eSNR). The cross correlation (CC) window length is 0.4 mm and the true WSR was set at 400 s^{-1}. The eSNR axis is computed for the uncoded broadband pulse.

for the FM chirp pulse over the broadband pulse. eSNR increases monotonically with PM code length as expected from Eq. 13). Longer duration uncoded pulses improve eSNR but only with a significant loss of bandwidth. The FM code preserves more bandwidth than the PM codes. The bandwidth of the decoded PM pulses increases with code length because Wiener filters in Eq. 12 approximate inverse filters at high eSNR with their greater ability to recover bandwidth.

The most important performance metrics for our application are the WSR errors, such as those shown in Fig. 13. Coded-pulse excitation effectively reduces Rbias by 9-22% and Rstd by 31-45% compared to the results using uncoded broadband pulses. The 8-bit Optimal code shows the minimal relative errors (Rbias -4% and Rstd 9%)

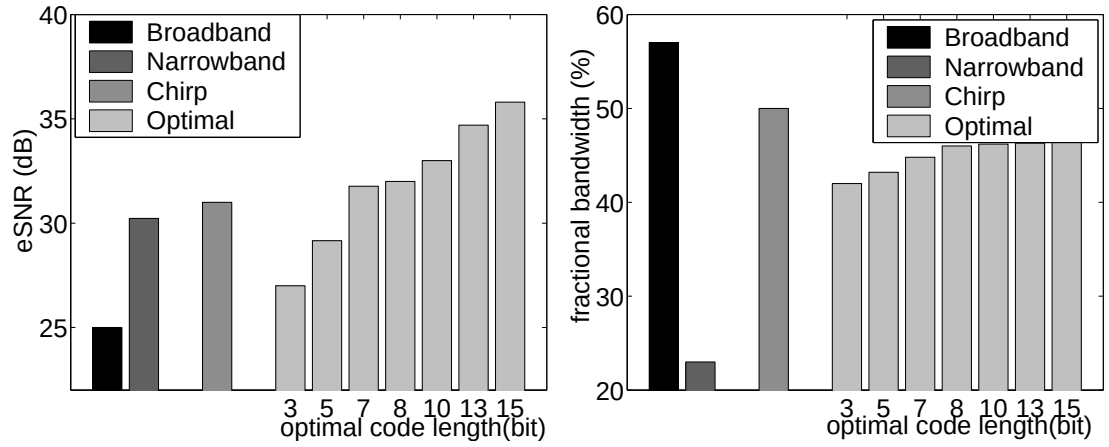

Figure 12. (a) Echo signal-to-noise ratio (eSNR) for a broadband, narrow-band, frequency-modulated (FM) chirp and phase-modulated (PM) Optimal-coded pulses. (b) Corresponding fractional bandwidths.

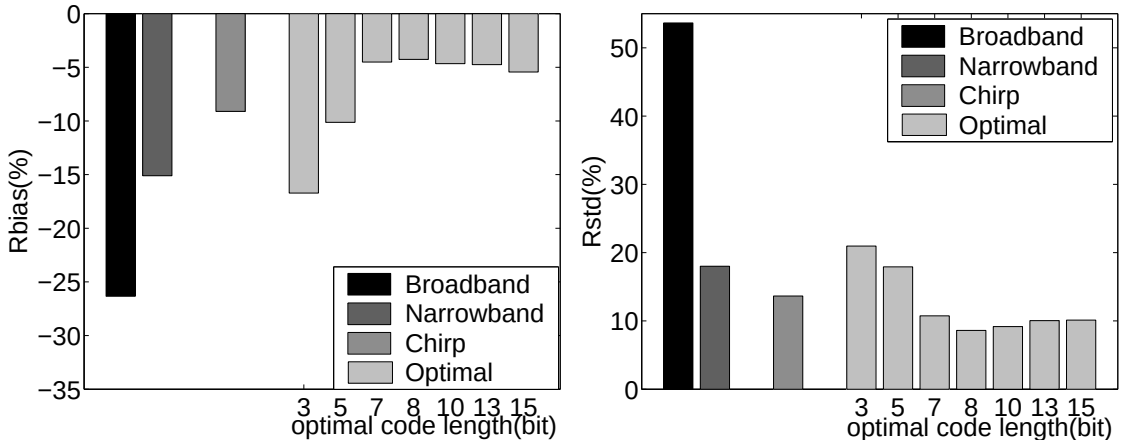

Figure 13. Wall shear rate (WSR) errors estimated from simulated echo signals.

for all the codes considered in this study. In these simulation data, the CC window length was 0.4 mm, eSNR = 25 dB, V_{max} = 500 mm/s, and PRF = 5 kHz.

We also examined the effects of code length and laminar flow WSR on WSR estimation errors; see Fig. 14. The normal atheroprotective physiological value of

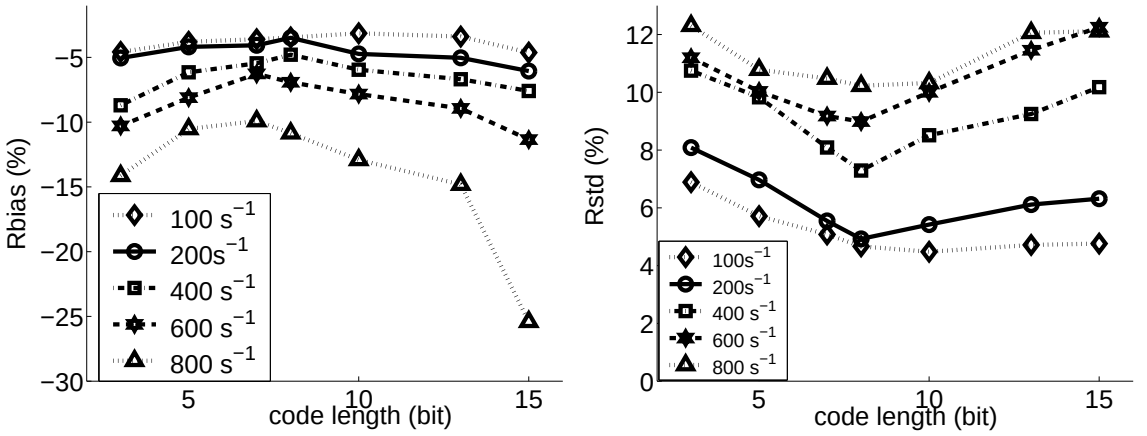

Figure 14. Wall shear rate (WSR) errors with increasing flow as a function of code length.

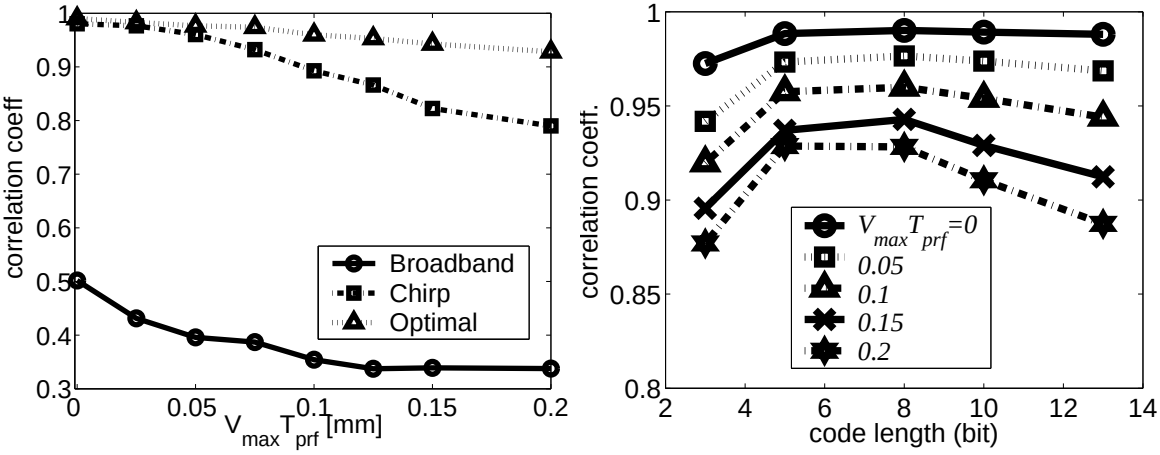

Figure 15. (left) Echo correlation coefficient versus flow velocities normalized by the pulse repetition frequency (PRF) = 5 kHz. (right) Correlation coefficients versus phase-modulated PM code length.

time-averaged WSS in carotid arteries is approximately 1.6 Pa.[6] From Eq. 1, and assuming blood viscosity is 4 mPa-s, WSR = 400 s^{-1}. From Eq. 11, which is for laminar flow, and assuming a 3 mm lumen diameter, V_{max} = 300 mm/s. Conversely, WSS $\leq$ 0.4 Pa is considered atherogenic. Other parameters being equal, WSR $\leq$

100 s^{-1} and $V_{max} \leq 75$ mm/s. The physiological effects on the vessel wall of WSS between these values is an open question. We measured WSR errors using simulated echoes under flow conditions when the true WSR values ranged between 100-800 s^{-1}, corresponding to a WSS range of 0.4-3.2 Pa. Other parameters are the same as those in the simulations described above. Fig. 14 shows that WSR errors increase slowly with WSR, and that PM codes near 8 bits minimize errors.

PM codes longer than 8 bits suffer larger WSR errors at high flow velocities despite higher eSNR and bandwidth. Errors increase because flow distorts the pulse code for the received echoes leading to echo decorrelation during displacement estimation, Eq. 16. We measured the correlation coefficient between echoes $g_d(m, k-1, q)$ and $g_d(m, k, q)$ over a 0.4 mm CC window. The results are summarized in Fig. 15. When there is no flow, $V_{max}T_{prf} = 0$, decorrelation is due to noise, including quantization and computational roundoff errors. As shown in Fig. 15 (left), both FM and PM coded pulses show higher signal correlation than that of the uncoded broadband pulse when eSNR = 25 dB. The signals slowly decorrelate as flow velocity increases (larger $V_{max}T_{prf}$). The same phenomenon can also be observed in Fig. 15 (right). The 8-bit PM code achieves maximum correlation under most of the simulated flow conditions where $V_{max}T_{\mathrm{prf}} < 0.2$. However, the 5 bit Optimal code reaches the maximum correlation while flow velocity is high ($V_{max}T_{\mathrm{prf}} = 0.2$). Shorter codes are limited by noise, while longer codes are limited by decorrelation from range side lobes that appear with greater code distortion.

2.5. Summary

Simulation results show that coded excitation improves eSNR without a significant loss of spatial resolution. In noise-limited situations, specifically when eSNR < 30 dB, coded-pulse excitation provides a significant reduction in velocity errors and therefore WSR errors. Although the selection of transmission bandwidth, carrier frequency, PRF, code type and code length depend on flow conditions, the criteria for selecting these parameters is straightforward. Select codes with the highest energy density per wavelength that are relatively insensitive to code distortions caused by scatterer motion and echo noise. Binary PM codes satisfy these criteria for our application. Then select a broadband transducer with a carrier frequency that gives a broadband-pulse eSNR between 15-25 dB to maximize spatial resolution within the high performance eSNR range of the code. Increase the code length to boost eSNR until WSR errors are minimal and further increases in code length decorrelate echoes. The eSNR of the decoded echoes must be high to minimize the duration of the CC window that dominates spatial resolution for the velocity estimator of Eq. 16.

3. IMPLEMENTING CODED EXCITATION ON THE IN-HOUSE SYSTEM

3.1. Objectives

The echo simulation described in Section 2 was modeling the conditions of our in-house experimental ultrasonic system while scanning a tissue-mimicking flow phantom with a steady inflow. The results suggest that both the systematic errors (bias) and random errors (standard variation) in WSR measurements can be significantly reduced by using broadband coded-pulse excitation techniques and processed with our velocity estimation method under conditions where eSNR is less than 30 dB inside the vessel. In this chapter, various ultrasound transmission pulses were examined in a series of phantom experiments to illustrate the feasibility of implementing coded-pulse excitation techniques on an experimental system.

3.2. In-house experimental ultrasonic system

The original experimental ultrasonic system was developed for imaging tumor blood flow by our former colleagues Kargel et al..[73] The experimental system was modified to use an arbitrary function generator instead of the tone-burst pulse generation board TB1000 (Matec, Inc.) to create excitation voltage waveforms for the purpose of implementing broadband coded-pulse excitation. The details of the pulse-echo imaging system are diagrammed in Fig. 16.

The low-cost experimental system consists of one single-element transducer me-

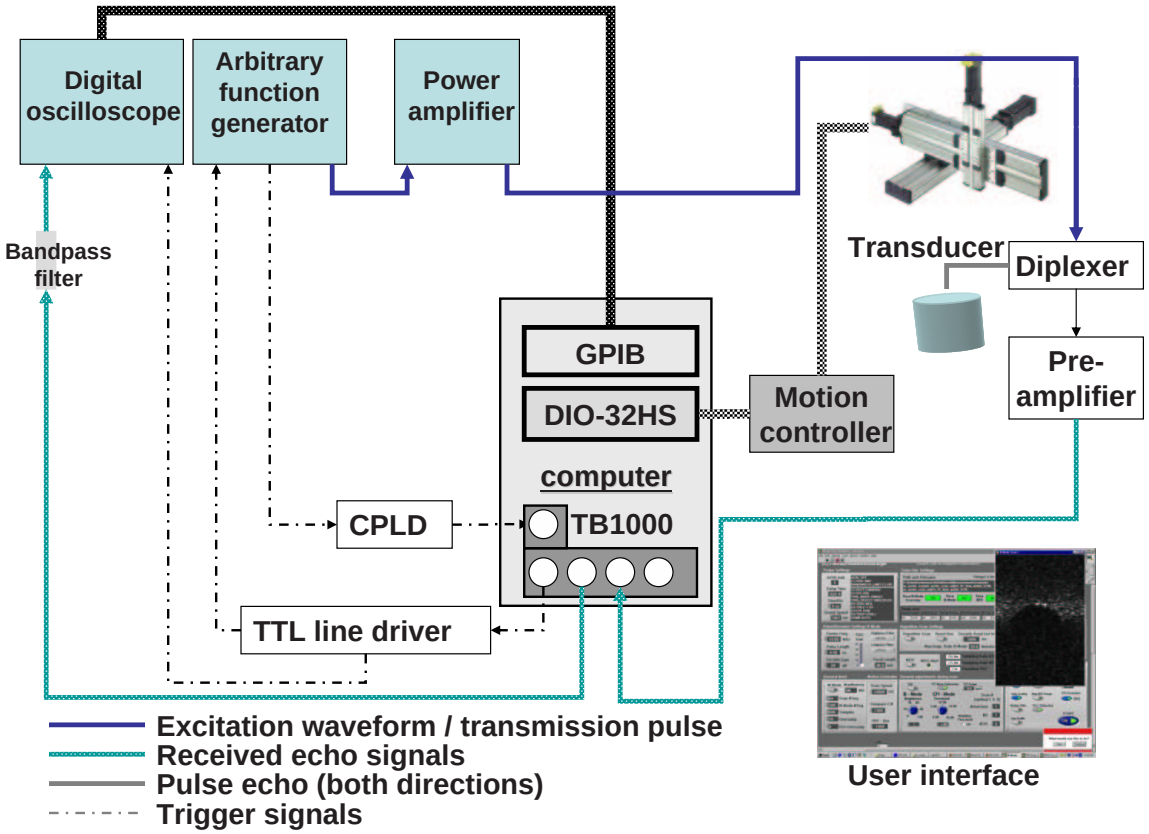

Figure 16. Block diagram of our in-house system. The user interface for adjusting parameters for data acquisition and image processing is shown in the lower right corner.

chanically scanned over five degrees of freedom. The programmable motion controller (Galil, Inc., DMC2000) determines the three Cartesian axes of the micro-positioning unit (Parker-Daedal). The remaining two degrees of freedom are applied by manually tilting the transducer about the axis with a goniometer. Optical quadrature encoders attached to the 3D positioner provide position accuracy of 100 nm. With a single transducer, echo data for a two dimensional ultrasonic image is acquired by

mechanically scanning across the region of interest. This method records echo data as a function of time while slowly moving the transducer perpendicular to the beam axis to acquire data from several spatial locations. Mechanical scanning provides a maximum flexibility in data acquisition and echo processing, but at the cost of frame rate. The low frame rate limits our ability to track dynamic changes in flow especially. In this study, a constant flow rate was applied and therefore the influence of low frame rate was minimal. To improve the lateral spatial resolution in the displayed image under the restriction of temporary storage memory, a smaller ROI and a low mechanical scanning speed of 1 cm/s were used. For constructing a 2D color flow image, multiple pulses per spatial location were transmitted. A constant temporal ensemble sampling interval (i.e. pulse repetition frequency, PRF) and scanning speed were applied to ensure accurate spatial registration and velocity reading.

Limited by a maximum of 10V peak-to-peak voltage output, the excitation waveforms were amplified by a 35dB power amplifier in order to drive the ultrasound transducer to transmit acoustic pulses. The pulse amplitude was monitored closely to avoid overheating the transducer. A low-noise pre-amplifier was used to improve received echo SNR, while a diplexer (Matec, DIP) protects the pre-amplifier from the high-voltage transmit pulses. RF echo signals are recorded at 8 bits and sampling rates up to 8 Gsamples/s by a digital oscilloscope (LeCroy, WavePro 940) with 16 MByte acquisition memory. Communication with the digital motion controller, scan action, control of the pulser/receiver and oscilloscope, synchronization of data acquisition and transfer, signal and image processing as well as image display are all

carried out by a host PC running LabView using IMAQ-Vision software tools. Most of the system parameters can be adjusted directly from the user interface (Fig. 16).

3.3. Ultrasound shear rate phantom studies with laboratory system

3.3.1. Flow phantom experiment setup

An acoustic flow phantom was constructed by forming a 5-mm-diameter horizontal cylindrical channel in a graphite-in-gelatin block (Fig. 17). The scattering fluid was a water-alcohol solution into which cornstarch particles were suspended at a concentration 3% by weight. The scatterer densities of the fluid and the surrounding gelatin were similar in order to accommodate the limited voltage resolution of the analog-to-digital converter (8-bit) on our experimental ultrasonic system. 60 cm of straight tubing was connected to the inlet of the flow channel to generate steady laminar flow. The fluid had similar density as water but with higher viscosity (density ~ 1 g/cm^3, $\mu > 1$ mPa-s). Reynold's number (Re) of the flow at room temperature was much smaller than the limit for laminar flow (Re<2000) for the 5-mm-diameter flow channel with an average velocity of 100 mm/s.[36] A perfusion pump supplied a known steady flow. The Doppler angle was adjusted to 72^o, the limit of the goniometer, the PRF was 1 kHz, and RF echo sampling rate ($1/T$) was 125 Msamples/s. Limited by the highest possible PRF (1kHz) in our laboratory system, the peak flow velocities (WSRs) were selected to be 100 mm/s (80 s^{-1}) and 200 mm/s (160 s^{-1}) in order to maintain a similar level of signal decorrelation between echo ensemble waveforms

that was found for the simulations. The product of $V_{max} \cdot T_{\text{prf}}$ values were 0.1 and 0.2 under these two flow conditions and were the same as those used in simulating data.

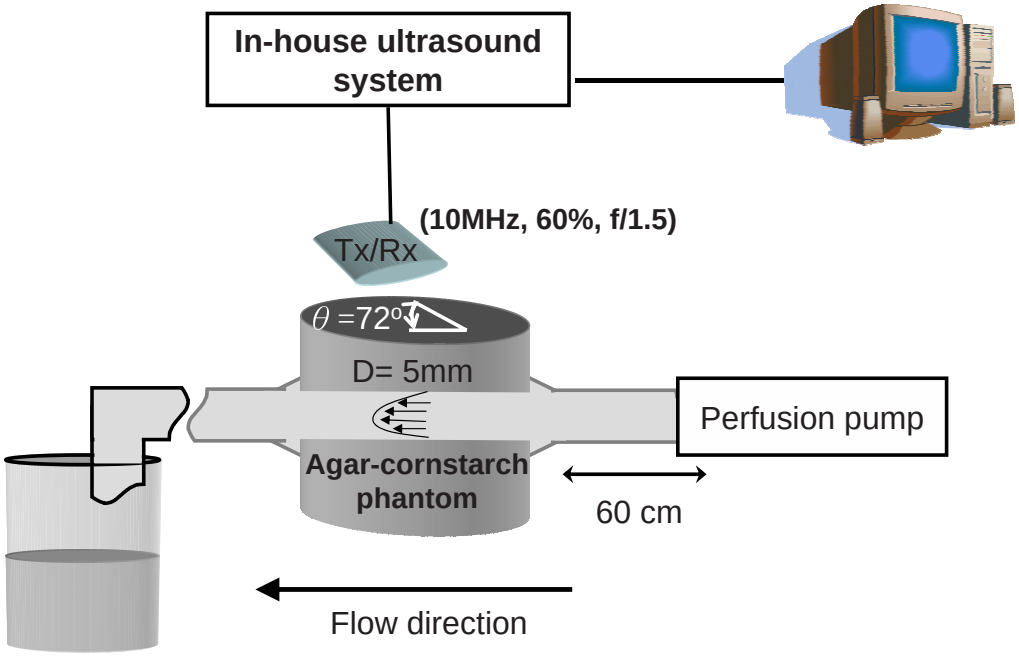

Figure 17. Experimental setup for flow phantom studies.

The lab-based imaging system consisted of a 10 MHz (60% bandwidth), 30-mm-diameter, f/1.5, circular aperture, spherically focused transducer[50] that was mechanically scanned. The depth of focus was very limited and approximately equal to $7.2\lambda(f/\text{No})^2 = 2.5$ mm. Fig. 18 a shows measured 2-D point spread functions imaged using a fine line target phantom at multiple depths near the radius of curvature. The axial impulse response $h_s(t|x)$ and corresponding frequency spectrum $|H(u|x)|$ are plotted in Fig. 18 b. Four types of excitation pulses were applied: one-cycle sinusoid, five-cycle sinusoidal bursts, 8-bit Optimal code convolved with a 1.67 cycle base sequence, and a linear FM chirp. The bandwidths of the base pulse and chirp were

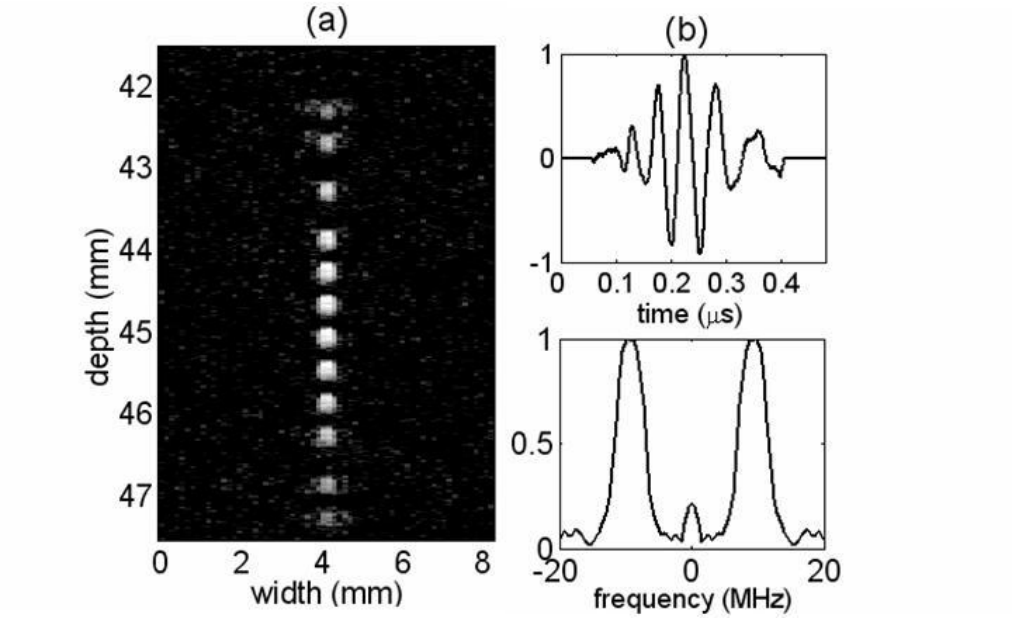

Figure 18. (a) 2-D point spread functions (psfs, log envelope of the RF echo) for the transducer used in phantom experiments as a function of depth. (b) Axial psfs near the radius of curvature and the corresponding frequency spectrum.

approximately equal to the bandwidth of the transducer. For further comparison, the duration of the chirp was adjusted to provide the voltage energy equal to that of the 8-bit Optimal code.

3.3.2. Data processing and wall shear rate estimation

The details of data processing and shear rate estimation methods are described in Section 2.3. In short, the received echo data are first being decoded to restore spatial resolution and then conditioned to minimize the amplitude difference from tissue clutter to reduce potential bias in velocity estimation. A modified velocity estimator is used to calculate the velocity profile with low estimation noise. Wall shear rate

values are then obtained by taking the spatial derivative of the estimated velocity profile.

The main difference between the simulation and the phantom studies is that, due to noisy data conditions, the phantom echo signals were compressed by two decoding methods to restore spatial resolution: Wiener filtering and matched filtering. The former method is explained in details in Section 2.3.3. Matched filter method is described below.

For PM codes, the received echo signals, $g[m,k]$ are compressed by a matched filter via convolving with the time reversed digital code sequence $c[-m]$,

$$g_d[m,k] = \sum_{l=-\infty}^{\infty} c[l-m]g[m,k] = \left[\sum_{q=-\infty}^{\infty} \phi_{cc}[m-q,k] \int_{-\infty}^{\infty} dx\, h_b(qT,x) f(x,t_s)\right] + n_d[m,k]\ , \tag{20}$$

where ϕ_{cc} is the autocorrelation sequence for the code, $h_b[m]$ is shorthand for the temporal convolution $\{h * b\}[m]$ and the noise is filtered, $n_d[m,k] = \phi_{cn}[m,k]$. For the FM chirp, e replaces c in the match filter:

$$g_d[m,k] = \sum_{l=-\infty}^{\infty} e[l-m]g[m,k] = \left[\sum_{q=-\infty}^{\infty} \phi_{ee}[m-q,k] \int_{-\infty}^{\infty} dx\, h(qT,x) f(x,t_s)\right] + n_d[m,k]\ . \tag{21}$$

Ideally, with successful pulse compression, $\phi[m] = \delta[m]$ for any code.

Matched filters are preferred in high noise environments to minimize noise amplification. However, when eSNR is large, e.g., near the focal length, inverse filters are preferred to minimize range side lobes. Fourier methods may be used to apply

inverse filtering in isoplanatic regions where the scattering is wide-sense stationary:

$$g_d[m,k] = \begin{cases} \mathcal{F}^{-1}\{G[u,k]/C[u]\} & \text{PM codes} \\ \mathcal{F}^{-1}\{G[u,k]/E[u]\} & \text{FM chirps} \end{cases} . \quad (22)$$

Unlike phantom data, inverse filters were applied to the simulation data to probe the limits of high spatial resolution velocity estimation.

3.4. Phantom study results using the laboratory ultrasonic system

3.4.1. Transmission pulse characteristics

Point spread functions:

Fig. 19 shows psf images measured from our lab system for the four pulse types: broadband, narrow-band, FM chirp and 8-bit PM Optimal code. Amplitudes have been normalized and log compressed to emphasize the presence of side lobes. Broadband pulses are most compact, having the highest bandwidth and lowest amplitude side lobes. The chirp pulse we adopted has more widely spread, higher amplitude range lobes than the Optimal code. The lateral pulse dimension is about the same for all pulses.

Matched filter decoding yields the highest eSNR at the cost of smaller bandwidth and higher range lobes. Wiener filters can balance the growth of range lobes and bandwidth but yield lower eSNR. Lower eSNR is observed from flow phantom measurements in Fig. 21 for both coded signals when using a Wiener filter instead of a

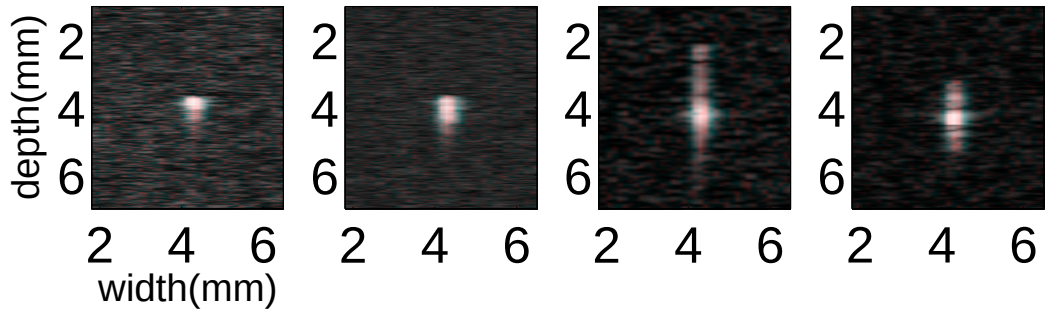

Figure 19. Envelope of the point spread functions (psfs) for (a) broadband, (b) narrow-band, (c) chirp and (d) 8-bit Optimal coded pulses after matched filtering.

matched filter. Also range lobes from the FM and PM pulses decrease from -12.5 dB to -22 dB and -17 dB to -25 dB using a Wiener filter in place of a matched filter. A 40% reduction in the main lobe width (improved lateral resolution) for both coded pulses was observed for the Wiener filter relative to the matched filter.

3.4.2. Flow experiment results

Echo signal-to-noise ratio using various pulses:

Fig. 21 shows a B-mode image across the phantom flow channel. The mid-point depth of section A is at the focal length of the 10 MHz, f/1.5 aperture. It is also near the anterior wall of the echogenic flow channel. Sections B and C are in the far field of the focused transducer. Table. 2 shows estimates of eSNR for the three sections. eSNR is greatest for all pulses in the focal region, decreasing with depth, but more slowly with coded pulses. We think the reason that eSNR for the FM code is lower than that for the PM code in simulation and higher in the experiment is related to

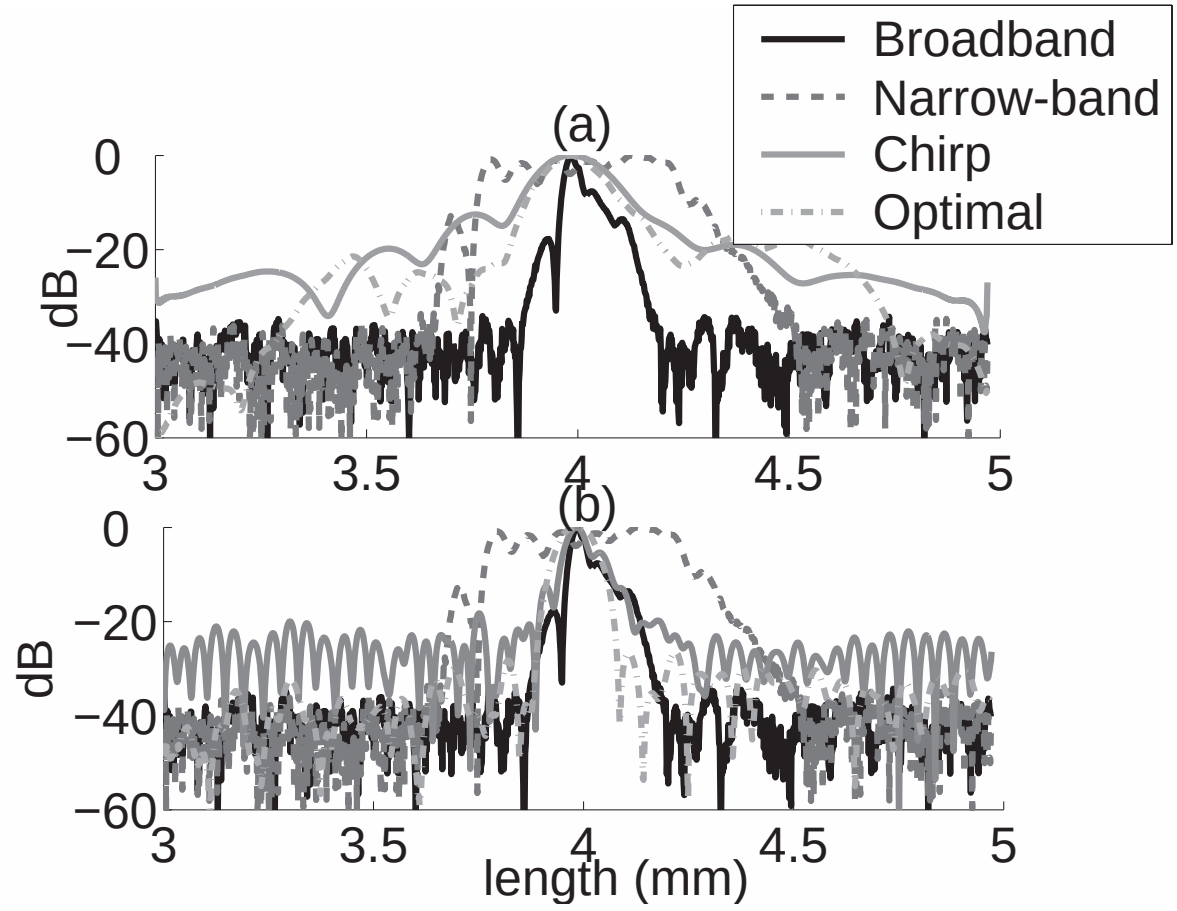

Figure 20. Axial profiles of the PSFs decoded by (a) matched filtering and (b) Wiener filtering.

the dual characteristics of the Wiener filter. eSNR was set to 25 dB for the echo simulations and was less than 2 dB for the lab system echo recordings. In low eSNR conditions, the Wiener filter responds like a matched filter, which enhances eSNR for the FM chirp. However, in high eSNR conditions, the Wiener filter responds more like an inverse filter, which is less efficient at decoding chirp pulses and thus yields a diminished eSNR. The decision about how to decode pulses is made depending on the task and its requirement for eSNR and spatial resolution.

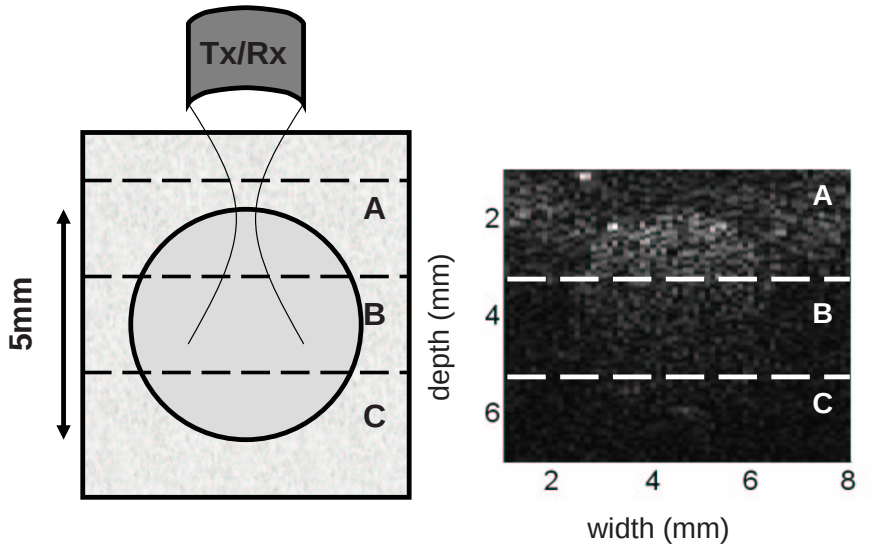

Figure 21. B-mode image of a cross-section of a flow phantom. Echo signal-to-noise ratio (eSNR) was measured at three phantom depths: A (centered on focal length $F = 45mm$), B ($F + 2$ mm) and C ($F + 4$ mm).

Velocity mapping of the phantom experiments under two flow conditions: Fig. 22 shows the color flow images estimated at two flow rates from data acquired with the broadband pulses (a)(g), narrow-band pulses (b)(h), chirp (c)(i)(d)(j) and 8-bit Optimal code (e)(k)(f)(l). Images (c)(i)(e)(k) were decoded by matched filters while (d)(j)(f)(l) were by Wiener filters. All images were acquired with a PRF of 1 kHz. The maximum flow rate was set to 100 mm/s in color flow images (a)-(f) and 200 mm/s for (g)-(l). The color flow images of a broadband pulse (Figs. 22 a,g) show that velocity estimation is too noisy to discern any type of the flow structure. Increased eSNR by using narrow-band or coded pulses allows the flow channel to be seen. The result is especially improved when either chirp or the 8-bit code is used. Due to the

Table 2. Echo signal-to-noise ratio (eSNR) measured from the flow phantom with different acoustic pulses and decoding methods: matched filters (MF) and Wiener filters (WF). Regions A, B and C correspond to those shown in Fig. 21.

	Broadband	Narrowband	Chirp		Optimal 8bit	
			MF	WF	MF	WF
(A)	1.43	6.05	12.26	10.47	11.93	10.25
(B)	0.88	2.25	10.94	7.74	10.46	7.14
(C)	0.21	0.41	3.19	2.33	2.83	2.39

small depth of focus, we can see the quality of the velocity estimation is dependent on the eSNR level. Results of Wiener filtered show much noisier estimates compared with those of matched filtered, especially at the lower half of the channel. Higher flows degrade imaging quality (noisier at the focal zone) and cause aliasing in the channel center where velocities are greatest.

Wall shear rate errors: For high echo noise conditions, the final shear rate profiles were obtained after radial averaging over 30 degrees ($\pm 15^o$ from the centerline of the flow channel) to further reduce estimation noise. Shear rate profiles under two flow conditions measured at the proximal wall along the centerline of the flow channel in a 2 mm range near the aperture focal length are plotted in Fig. 23. Results using matched filters (MF) and Wiener filters (WF) to decoded echoes are shown. The corresponding WSR error estimates are listed in Table 3. Broadband pulses generate the largest errors due to low eSNR. The improvements using narrow-band

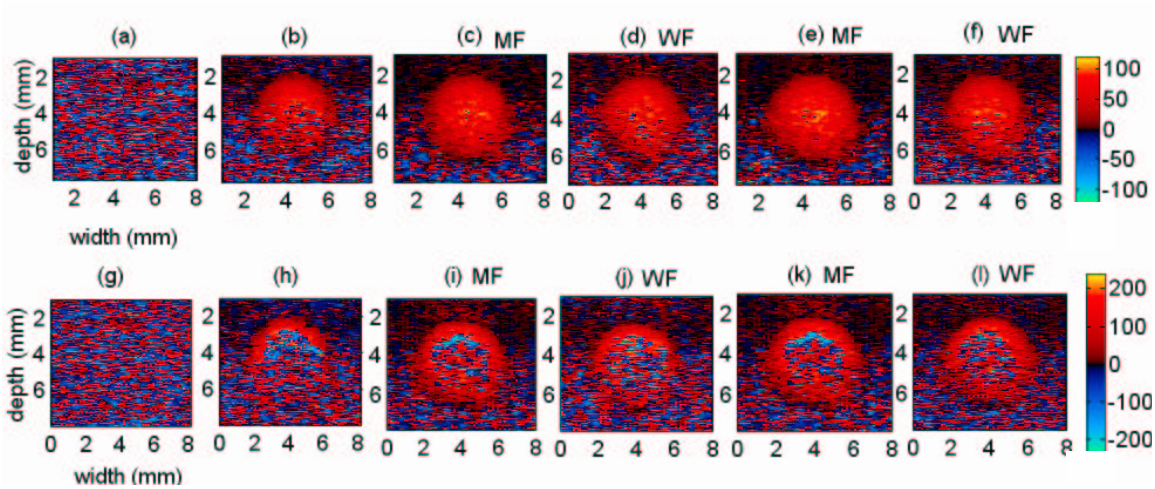

Figure 22. Color flow images from phantom studies with various excitation pulses. MF: decoded by matched filtering. WF: decoded by Wiener filtering. Maximum velocity for images in first row is 100 mm/s and 200 mm/s for the second row.

and coded pulses follow the same trends observed in the simulations. Wiener filters outperformed matched filters by suppressing additional 2-8% in WSR bias but at the cost of increased random error (4-5%).

3.5. Summary of phantom studies with the in-house system

This series of flow phantom studies demonstrates the feasibility of implementing broadband coded excitation techniques on a laboratory ultrasonic system with promising results in dramatic reduction of WSR errors in the shear rate experiments.

The experimental data are consistent with the analysis and results from 1-D simulated echo data. As shown in this chapter, both FM and PM coded excitation

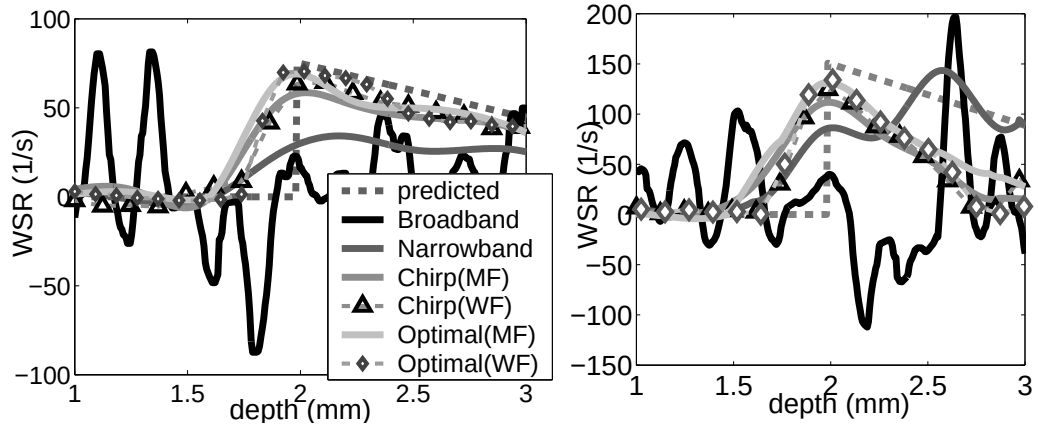

Figure 23. Shear rate measurements in flow phantom with steady laminar flow. Four pulses and two compression filters are examined at two peak flow velocities, V_{max} = 100 and 200 mm/s). Optimal coded pulses decoded by Wiener filters provided the most accurate shear rate estimates under both flow conditions

Table 3. WSR errors measured from flow phantom experiments. Maximum flow velocities were (a) 100 mm/s and (b) 200 mm/s.

		Broadband	Narrowband	Chirp		Optimal 8bit	
				MF	WF	MF	WF
(a)	Rbias(%)	-65	-42	-18	-12	-9	-7
	Rstd(%)	58	34	10	14	8	13
(b)	Rbias(%)	-67	-43	-25	-17	-13	-11
	Rstd(%)	57	36	15	20	10	16

improves eSNR without a significant loss of spatial resolution. In noise limited situations (eSNR $<$ 30dB), as suggested from the simulation results in Section 11, coded-pulse excitation effectively suppresses both velocity errors and WSR errors.

By using a Wiener filter instead of a matched filter to compress the coded signals to recover the spatial resolution, the resulted eSNR is lower but the restored bandwidth is higher (Table 2). As a result of these two signal characteristics, signal decoded by Wiener filtering shows more improvement in reducing systematic errors (Rbias) than in suppressing random measurement errors (Rstd) as compared with matched filtering. However, the differences in measurement errors between these two decoding methods are small, and final measurement errors are still much lower than the uncoded pulses.

The laboratory system provides a lot of flexibility in data acquisition and image processing. However, the high system noise from the power amplifier, narrow signal dynamic range, and slow acquisition frame rates limit the benefits of using broadband coded-pulse excitation techniques in WSR measurements. Through collaboration with Siemens Medical Solutions, we are able to implement PM coded-pulse excitation techniques directly onto a commercial medical ultrasound scanner. The experimental results will be shown in the next chapter.

4. IMPLEMENTATION CODED-PULSE EXCITATION TECHNIQUES ONTO A COMMERCIAL SCANNER

4.1. Objectives

The feasibility of implementing coded-pulse excitation techniques onto a laboratory ultrasonic system has been demonstrated in Section 3. The quantitative error analysis in phantom studies showed that coded acoustic pulses with high spatial resolution and high pulse energy effectively improved the accuracy and precision in the ultrasonic wall shear rate measurements. This chapter describes further implementation of this method onto a commercial medical imaging system (Siemens Antares, Siemens Medical Solutions, Mountain View, CA). With such device, we were able to take advantage of its robust and versatile design, including better eSNR, wider dynamic range, higher lateral spatial resolution, faster frame rate and a wider range of pulse repetition frequencies to construct 2D shear rate images. The simulation studies (Chapter 2) shows that the measurement errors vary as a function of imaged shear field. In order to confirm the simulation results, a Hele-Shaw parallel-plate flow chamber that delivers a shear range between 100-625 s^{-1} (corresponding shear stress of 0.3-1.9 Pa) is developed for ultrasonic WSR error assessment. The feasibility of in vivo imaging is also shown in this chapter.

4.2. Implementation of coded-pulse excitation onto a commercial scanner

In our laboratory system, an analog arbitrary function generator was used to create the excitation waveforms that drive the transducer to transmit the acoustic pulses. In the commercial scanner, the transmission pulse is generated based on a built-in index table (TXPG in Fig. 24) depending on the current imaging mode and selected system parameter. In order to transmit coded pulses on a digital system, we generated several index tables in binary format with our desired coding sequences using Matlab. The table is then uploaded to the Antares system via proprietary Siemens development interface to overwrite the defaults, thus enabling coded pulse transmission. RF data are acquired using ultrasound research interface (URI) and processed off-line to generate the 2D shear rate images. In order to prevent the possibility of overheating the ultrasound probe, the energy of transmission pulses is controlled under the maximum limit by setting the pulse amplitude lower than that of a similar-length uncoded narrowband pulse. The pulses are switched back to the system default right after the data acquisition. This switching step is done by manually running a separate script to avoid problems occur during the data capture and transfer steps.

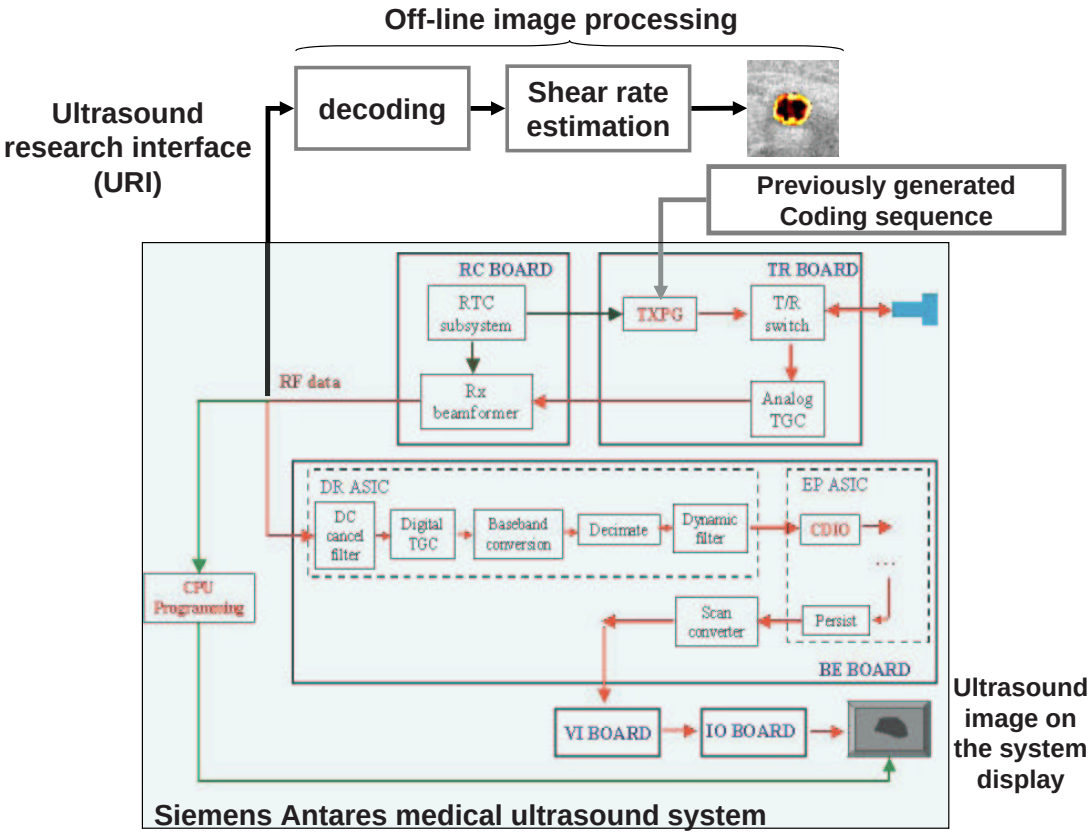

Figure 24. Block diagram of basic imaging processing algorithm in a commercial medical ultrasonic system.

4.3. Development of the Hele-Shaw WSS flow chamber for ultrasonic experiments

The flow chamber generates a WSS that varies approximately linearly along its length as schematically depicted in Fig. 25 a. The flow channel has a constant height $h = 3$ mm throughout its 130-mm length, an entrance width $w_1 = 3$ mm, and an exit width $w_e nd = 9$ mm. The channel width w increases along the length axis x according to $w = 150w_1/(150 - x)$ mm for $0 \leq x \leq 100$ mm. For the second part of the chamber,

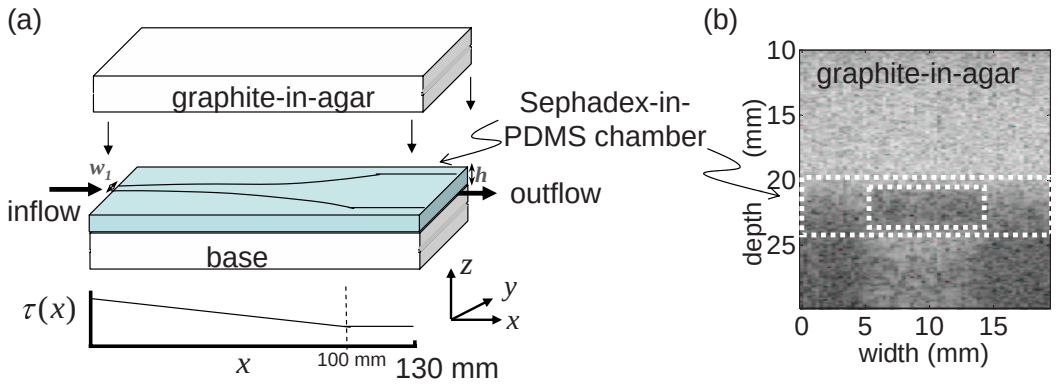

Figure 25. (a) Flow chamber geometry. (b) Ultrasonic B-mode image of the flow chamber in cross section. The PDMS chamber contains Sephadex scatterers, and is surrounded by a graphite-agar ultrasonic phantom medium.

the channel width is a constant of 9mm for $100 \leq x \leq 130$ mm. The expanding channel width creates a lateral flow profile that varies, beginning close to a parabolic flow at the entrance $x = 0$ mm and ending approximate to a blunt flow at $x = 100$ mm. CFD simulations were performed to obtain more accurate flow field information (Section 4.4). The flow channel design was first created using AutoCAD (AutoDesk Inc), optimized using CFD, and the best design was molded out of machined plastic. The chamber material was a mixture of poly-dimethylsiloxane (PDMS) (Slygard 184, Dow Corning) at a 5:1 ratio of base to curing agent. PDMS was selected over agar and gelatin due to its flexible yet sturdy material properties after curing. The drawback is the high acoustic attenuation, which will be discussed in Section 4.5. Therefore, casting a thin layer (<1 mm) of PDMS at the top and bottom of the flow channel minimized ultrasonic echo-signal losses. The PDMS also contained Sephadex G-100

microspheres (Sigma-Aldrich, St. Louis, MO) at a concentration of 3% by mass to generate ultrasonic scattering. The PDMS mixture was placed under vacuum for at least 30 minutes to remove the air bubbles created during the mixing processing, which would contribute to further loss in signal strength due to attenuation. The PDMS mixture was then cured to create the shape of the flow chamber after 1 hour of baking at 75^{o}C. The flow connectors were last inserted into the outlet and inlet and sealed with PDMS after a second time of curing at 75 ^{o}C. Tissue-mimicking graphite-agar blocks pressed onto the top and bottom chamber surfaces provided rigidity to the walls. Fig. 25 b shows a cross-sectional B-mode image of the rectangular flow channel (dotted line), surrounded by graphite-agar blocks. A 14 dB loss of echo-signal amplitude can be seen to either side of the flow chamber beneath the 5 mm-thick PDMS sidewalls.

4.4. Computational fluid dynamic simulation

4.4.1. Geometry and mesh generations

A mold of the flow channel volume was depicted to form a volume grid for CFD simulation. An overset grid approach was used together with body fitted meshes to model the system. The two computational meshes were created within the 100-mm expanding width section of the channel and the 9-mm constant width section at the end (Fig 26). The constant width section prevented back flow disturbance due to mismatched flow impedance at the outlet connector. Since flow is symmetric about the central axis of the channel, we simulated flow in only one quarter of the

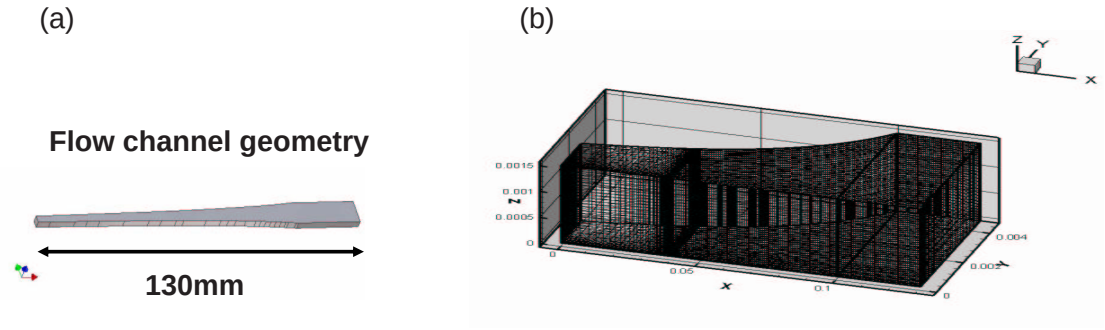

Figure 26. (a) Flow channel geometry. (b) Computation mesh created within the flow channel for CFD simulation.

cross sectional area to reduce computational time and attain high spatial resolution. The CFD mesh was created using object-defining nodes from which a surface mesh was then generated. Finally a volume mesh using a structured grid was produced. The number of nodes chosen balanced the need for spatial resolution and reasonable computation time. The mesh was progressively refined and presented solution has shown to be mesh independent.

4.4.2. Initial and boundary conditions

The CFD software Fluent (Fluent Inc, Lebanon, NH) was used in the CFD simulation. The simulation parameters were those used in ultrasound studies. At the flow inlet, a uniform flow velocity of 200 mm/s was applied normal to the chamber cross-section. Chamber walls were assumed to be rigid and a no-slip condition was applied. At the outlet, the flow was assumed to be fully developed. The 200 mm/s average flow velocity input into the channel was selected based on parallel plate flow chamber

studies. With viscosity of flow medium equals to 3 mPa-s, it creates the linear shear field range 0.3-1.9 Pa , which covers both the low-shear atherogenic (<0.4 Pa) and high-shear atheroprotective (>1.2 Pa) ranges.

4.4.3. Governing Equations.

In general, shear rates in medium and large arteries are sufficiently large to assume that blood behaves as a Newtonian fluid.[74] The blood mimicking fluid material (RG Shelley Ltd, Ontario, Canada) used in the experiments is also a Newtonian fluid.[75] Therefore, flow in the chamber is governed by the mass and linear momentum conservation equations for an incompressible viscous fluid:

$$\nabla V = 0 \qquad \text{and} \qquad \partial V/\partial t + (V\nabla)V = -1/\rho(\nabla p) + \nu\nabla^2 V, \tag{23}$$

where V is the velocity vector, p is pressure, t is time, ρ is fluid density, and ν is fluid kinematic viscosity. The flow density and viscosity were constant with ρ=1050 kg/m^3 and ν=0.003 Pa-s. Based on the inlet velocity and entrance width, Re was 180. Since Re is below 2100, the CFD simulation was performed based on the laminar flow condition.

4.4.4. Simulation results

Fig. 27 a depicts computed velocity contours within the flow chamber. At any x, the velocity is maximal at the channel center as expected, and the velocity decreases progressively with x. WSR at the bottom plate of the flow channel that predicted by CFD simulation is illustrated in Fig. 27 b. As expected, WSR is the highest near

the entrance and decreases with larger channel width. WSR derived from the CFD was determined to decrease linearly with distance from the inlet in the region 25 mm $\leq x \leq$ 95mm (Fig. 27 c). A linear regression fit yield a correlation coefficient of 0.98. Fig. 27 d shows the computed velocity profiles along the z axis at the positions marked in Fig. 27 a. As expected, the velocity profiles are parabolic with maximum velocities at z=0. The estimated WSR profiles along the y axis are plotted in Fig. 27 e. Near the entrance, the flow channel is very narrow so the flow profile is nearly parabolic, which means the WSR is much higher at the regions close to the center line than area close to side walls. However, due to gradual expansion in the channel, the flow profile at the sections near the channel outlet become more blunt, similar to that of a parallel-plate flow chamber geometry. This phenomenon results in a much flatter WSR profile at the end of the flow channel (Fig. 27 e).

4.5. Acoustic properties of PDMS

In this series of studies, PDMS is used to construct the ultrasonic flow chamber to create an acoustic environment similar to an adult's carotid artery. Though tissue-mimicking materials like agar and gelatin have been widely in ultrasonic studies, but PDMS has been chosen for its sturdiness in making arbitrary-shaped phantoms. However, as shown in Fig. 28, the attenuation of ultrasound through a thin layer of PDMS pad is much higher than that through a thick agar block. This effect is reduced by minimizing the thickness of the PDMS sample (Fig. 28 b). Ultrasound gel in this figure is served as reference to show the condition with minimal signal attenuation.

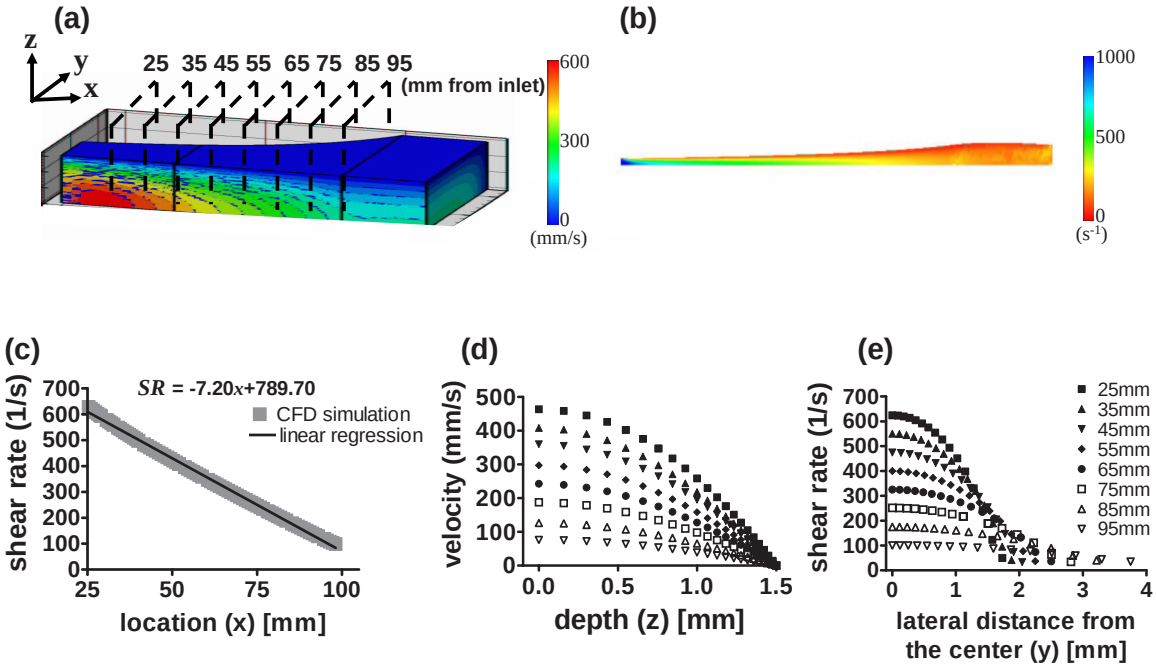

Figure 27. CFD simulation results. (a) 3D velocity and (b) 2D wall shear rate contours within the flow channel. (c) Wall shear rate along the center axis of the flow channel is a linear function of distance from the flow entrance. (d) Cross-sectional velocity profiles at different scan planes as a function of the z axis. (e) Wall shear rates are plotted along the y axis for different scan planes.

In order to predict and effective minimize the echo-signal loss from acoustic propagation through PDMS, longitudinal sound speed and attenuation coefficients were estimated in water at room temperature. We used a substitution technique[76] where the phase and amplitude of narrow-band pulses transmitted through different samples of PDMS in water were measured. The experiment setup is illustrated in Fig. 29. For each attenuation estimate, signals from two samples of different thicknesses were

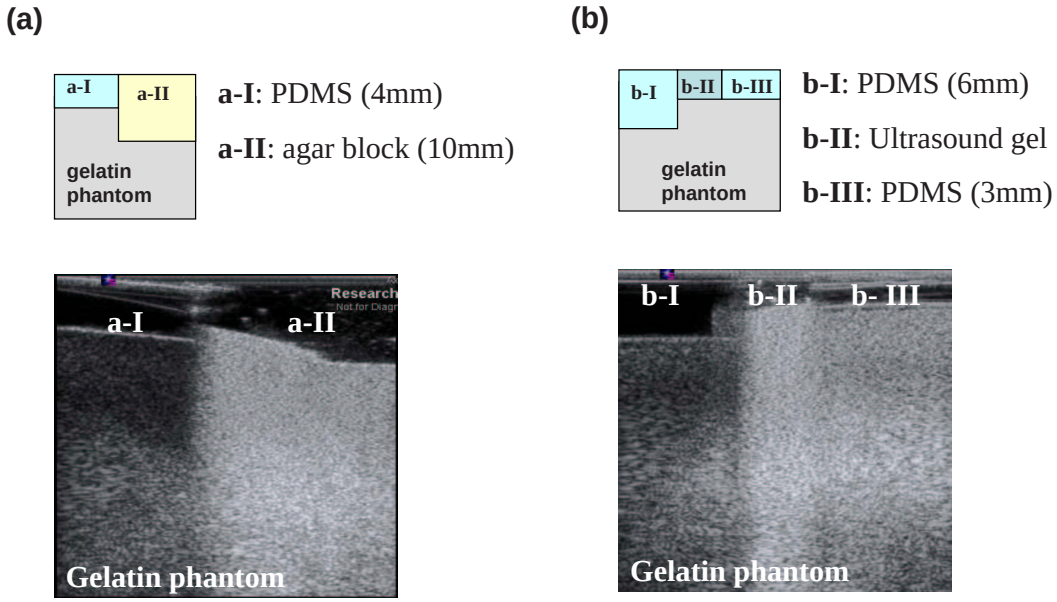

Figure 28. PDMS causes significant signal loss due to its highly attenuating property. A gelatin phantom is imaged through different materials to illustrate the comparative attenuation effects. (a) This figure illustrates the different effects of attenuation from a 4mm PDMS layer and a 10mm agar block on the intensity of the underlying gelatin phantom. (b) 6mm-thick PDMS is placed on the left side, while a 3mm-thick PDMS is on the right side, with ultrasound gel in the center serving as a nonattenuative reference material. Reduction in PDMS sample thickness can improve the intensity of the underlying material dramatically.

compared, instead of comparing signals with and without a PDMS layer, to minimize estimation bias from reflective losses. The experiments are repeated for frequencies between 3-11 MHz. The frequency-dependent attenuation coefficient α is then calcu-

lated via

$$\alpha[dB/cm] = \frac{20}{d}\log(\frac{A_1}{A_2}), \tag{24}$$

where d is the thickness difference between 2 PDMS samples, and A_1 and A_2 are the signal amplitudes recorded from the thinner and thicker sample, respectively.

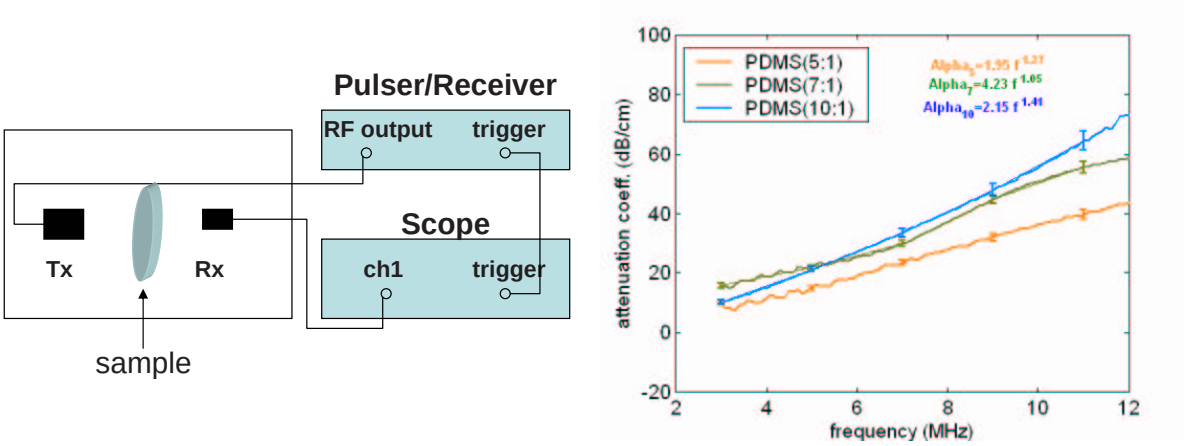

Figure 29. Experiment setup for measure PDMS attenuation and the measured attenuation coefficients for different PDMS samples as a function of frequency.

Results of the attenuation and speed of sound measurements over the diagnostic imaging frequency range are summarized in Table 4. The speed of sound in PDMS is significantly lower than that in water. The speed of sound is determined by density ρ and compressibility κ of the medium (Eq. 25).

$$c = \frac{1}{(\kappa\rho)^{0.5}} \tag{25}$$

The impedance difference between PDMS and water could be reduced somewhat by reducing κ (i.e. increasing the stiffness). This approach is achieved by raising the concentration of prepolymer curing agent to increase the cross-linkage in the cured PDMS. However, changing the ratio of the curing agent to the polymer base from 1:10 to 1:5 increased the sound speed by just 4% and decreased the attenuation coefficient at all frequencies. The acoustic properties of PDMS remained very different from biological tissues. Nevertheless, the mechanical properties of PDMS for the flow channel offer major advantages. Acoustic losses were minimized by imaging through a 1-mm thick PDMS layer.

Table 4. Acoustic properties of PDMS

	Speed of sound (m/s)	Attenuation coefficient (dB/cm)			
		5 MHz	7 MHz	9 MHz	11 MHz
PDMS(5:1)	1119.1 ± 49.3	14.86 ± 0.62	23.38 ± 0.80	31.94 ± 1.23	39.61 ± 1.51
PDMS(7:1)	1089.1 ± 11.8	21.92 ± 0.77	29.88 ± 0.89	44.88 ± 1.46	55.51 ± 2.14
PDMS(10:1)	1076.5 ± 12.1	21.30 ± 1.12	33.57 ± 1.45	47.85 ± 2.26	64.33 ± 3.31

4.6. Ultrasonic shear rate measurements

The experimental apparatus is shown in Fig. 30. Blood mimicking fluid[75] was used as flow medium for the ultrasound experiments. The flow channel was separated from the peristaltic pump using two glass flasks in series that serves as a buffer to eliminate flow pulsatility and provide steady inlet velocity with a volumetric flow rate of 1.8

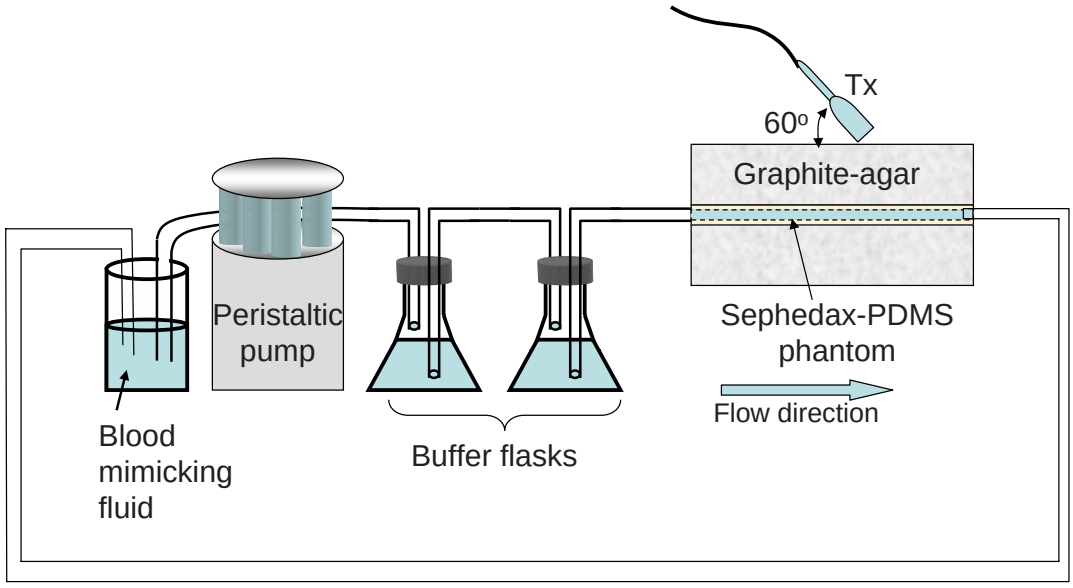

Figure 30. Diagram of the ultrasound flow experiment.

ml/s. A large-diameter tubing (8 mm) was connected to the 3x3-mm channel inlet so that the entering flow velocity profile was assumed to be blunt with an average velocity of 200 mm/s. The imaging Doppler angle was adjusted to 60^o.

A Siemens Antares system with URI provided the access of store echo signals for off-line analysis. RF data were acquired in image planes along the cross section of the flow channel at 10 mm increments. The transmission frequency on the linear array was 8.9 MHz and the PRF was 3.5 kHz. Four groups of transmission pulses were programmed into the Siemens Antares using special manufacturer software: uncoded broadband imaging pulses (1 cycle), uncoded narrow-band Doppler pulses (4 cycles), PM code pulses (7 and 13-bit Optimal codes),[67] and FM code pulses (1.17 and 2.10 μs pseudo chirps).[57] The transmission amplitude was the same for all pulses.

Also the transmission energies of the PM and FM codes with similar durations were approximately equal. The received signals were decoded using matched filters to restore spatial resolution as described previously.[49]

The 2D PSFs of all imaging pulses measured from a thin wire (60 μm) are shown in Fig. 4.6. It is obvious the energy from coded pulse (Fig. 4.6 c-f) is much greater than that of uncoded either a broadband or a narrow-band pulse (Fig. 4.6 a, b). Sidelobes that degrade the contrast resolution were generated during the decode process. However, the peak-to-side lobe ratio increases when a coded pulse was used.

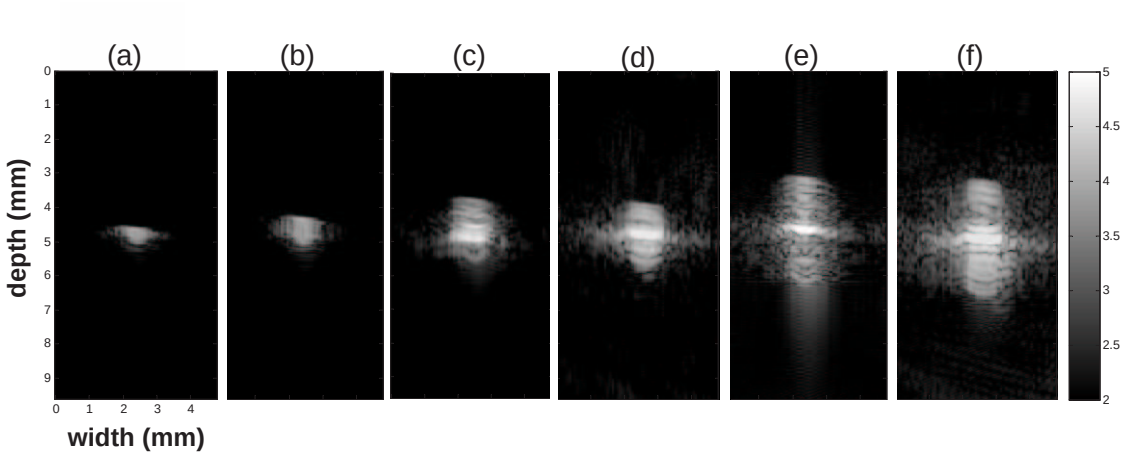

Figure 31. Two dimensional point spread functions of the imaging pulse used. (a) one cycle broadband, (b) four cycle narrow-band, (c) 7 bit optimal code, (d) 1.17 μs pseudo chirp, (e)13 bit optimal code and (f) 2.1 μs pseudo chirp. The brightness is normalized for all images.

4.6.1. Shear rate estimation

The velocity estimation algorithm used for WSR estimation was described and evaluated in previous chapters. Basically, velocity profiles are computed off-line using a broadband correlation velocity estimator by minimizing the energy of an objective function with two terms. One term is based on the cross correlation function between the ensemble pair. The other is a smoothness constraint obtained from the conventional color-flow processing algorithm, which regularizes the first term by suppressing noise. WSR estimates are then calculated via the radial derivative of the Doppler-angle-corrected velocity estimates. The strength of this velocity estimator relative to conventional Doppler methods is amplified near the wall of the flow channel or blood vessel.

4.6.2. Evaluation metrics

WSR estimation performance is evaluated based upon the bias and standard deviation of estimates. Relative percent bias is defined in terms of the ensemble mean of the values estimated $\widehat{\mathrm{WSR}}$ and predicted WSR (details see Section 2.3.7:

$$Rbias = \frac{\mathcal{E}\left\{\widehat{\mathrm{WSR}}\right\} - \mathrm{WSR}}{\mathrm{WSR}} \times 100\%;, \qquad Rstd = \frac{\left(\mathcal{E}\left\{\widehat{\mathrm{WSR}}^2\right\} - \mathcal{E}^2\left\{\widehat{\mathrm{WSR}}\right\}\right)^{1/2}}{\mathrm{WSR}} \times 100\%;. \tag{26}$$

The predicted WSR is obtained from CFD simulation results in Section 4.4.4.

4.7. Ultrasonic shear rate imaging results from phantom studies

Examples of 2-D velocity and 2-D shear rate images acquired using a 2.1 μs pseudo-chirp pulse are shown in Fig. 32. Images were acquired at either 85 mm or 25 mm downstream of the inlet. The velocity at 85 mm is 70% lower than that at 25 mm due to the larger cross sectional area. Peak velocities are observed at the center of the lumen where shear rates are minimal. The maximum shear rate is observed near the wall. The flow direction is parallel to the top and bottom plates of the flow channel, therefore shear rates are estimated by taking the derivative of velocity with response to the channel depth z.

The performance of the WSR estimator was evaluated by comparing Rbias and Rstd measured for different transmission pulse types. Details of ultrasonic WSR measurements are found in Fig. 33. To compare the impact of change in transmitted power on WSR estimation, the pulse amplitude used to generate results in Fig. 33 a-c is three times that used in the results of Fig. 33 d-f. eSNR inside the lumen was estimated via[49]

$$\text{eSNR}(x) \simeq 10 \log(\hat{\sigma}_g^2(x)/\hat{\sigma}_n^2 - 1). \tag{27}$$

The noise-free echo signal g was obtained by averaging 50 RF frames, while noise n was found from the difference between the average echo signal and any one realization.

Coded pulses yield higher eSNR than the uncoded pulses. The maximum eSNR was found when a 13-bit Optimal code or a 2.1 μs pseudo chirp was transmitted

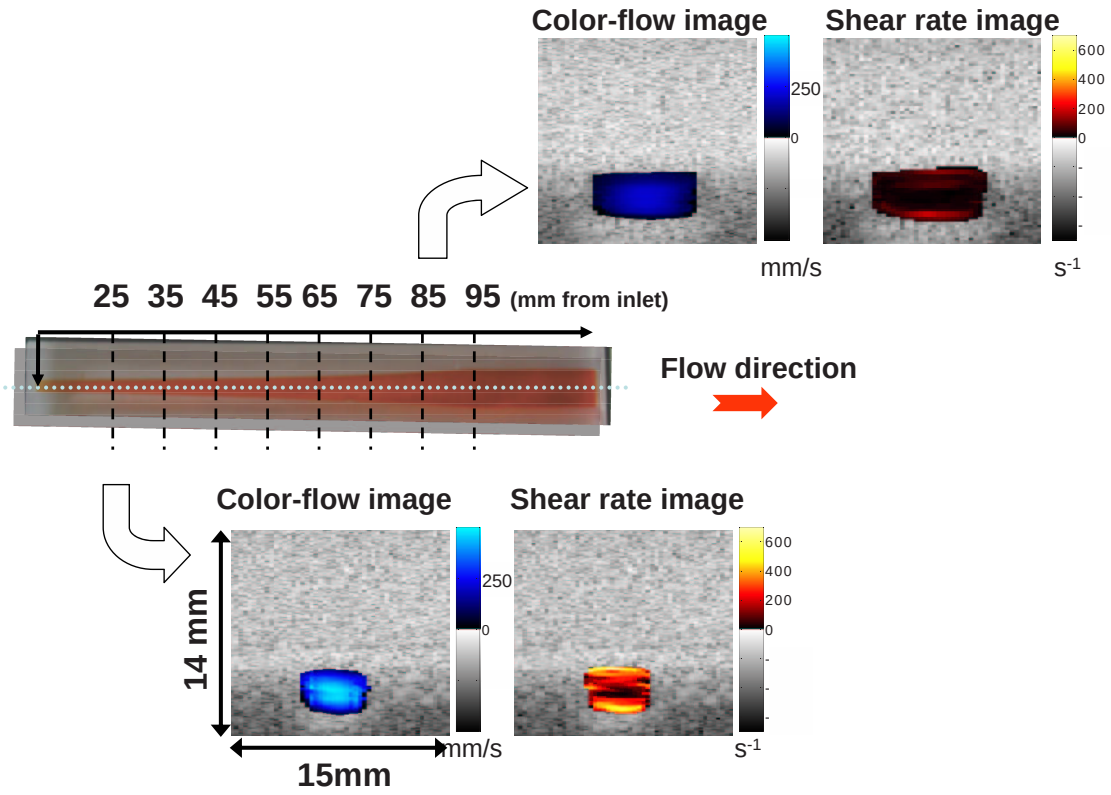

Figure 32. 2D velocity images in the $y-z$ plane at x = 85 mm (top row)and x = 25 mm (bottom row) and the corresponding shear rate images. The actual ultrasound flow chamber is shown at the center of the figure. The black dotted lines are the locations where the ultrasound data acquisitions take place. In all cases, a 2.1 μs pseudo-chirp coded pulse was used.

(Fig. 33 a, d). As expected, by tripling the transmission voltage, eSNR increases 10 dB for all pulses (Fig. 33 a). Comparable eSNR and WSR errors were observed between FM and PM coded pulses with similar pulse lengths, which were originally designed to have the same transmission energy. Pulses with the highest eSNR generate the minimum WSR errors. The improvement in WSR errors is greater when the

transmission voltage is low. In Section 2, the simulation results indicated there is no advantage of using coded pulses when eSNR exceeds 30 dB. However, to avoid over-heating the transducer, the greatest energy used in this study was ∼90% of the FDA limit (Fig. 33a-c).

Decoding using matched filtering techniques achieves the maximum eSNR but at the cost of lower image contrast due to range lobes. Range lobe length is positively correlated to the transmitted code duration. Unsuccessful decoding biases WSR estimates by mixing clutter and noise with the echo signals. The effect is more prominent when a longer code is used in a fast flow condition. As shown in Fig. 33 b, when shear rate is greater than >500 s^{-1}, WSR bias obtained from the 13-bit Optimal code and the 2.1μs pseudo-chirp code are slightly greater than those of shorter codes. In situations where eSNR is low, the noise reduction from longer codes is more important than range lobe clutter and therefore is recommended. Possibly due to greater decorrelation between signal ensembles, both Rbias and Rstd increase with shear rate for all imaging pulses.

4.8. In vivo vascular shear rate imaging

Our method was also used to scan the left common carotid artery and left brachial artery of a healthy female volunteer in her twenties. The data acquisition was ECG triggered at peak systole and diastole in order to compare results among the four different imaging pulses. The Doppler angle was estimated to be around 50^o. Data for 20 cardiac cycles were acquired for each measurement.

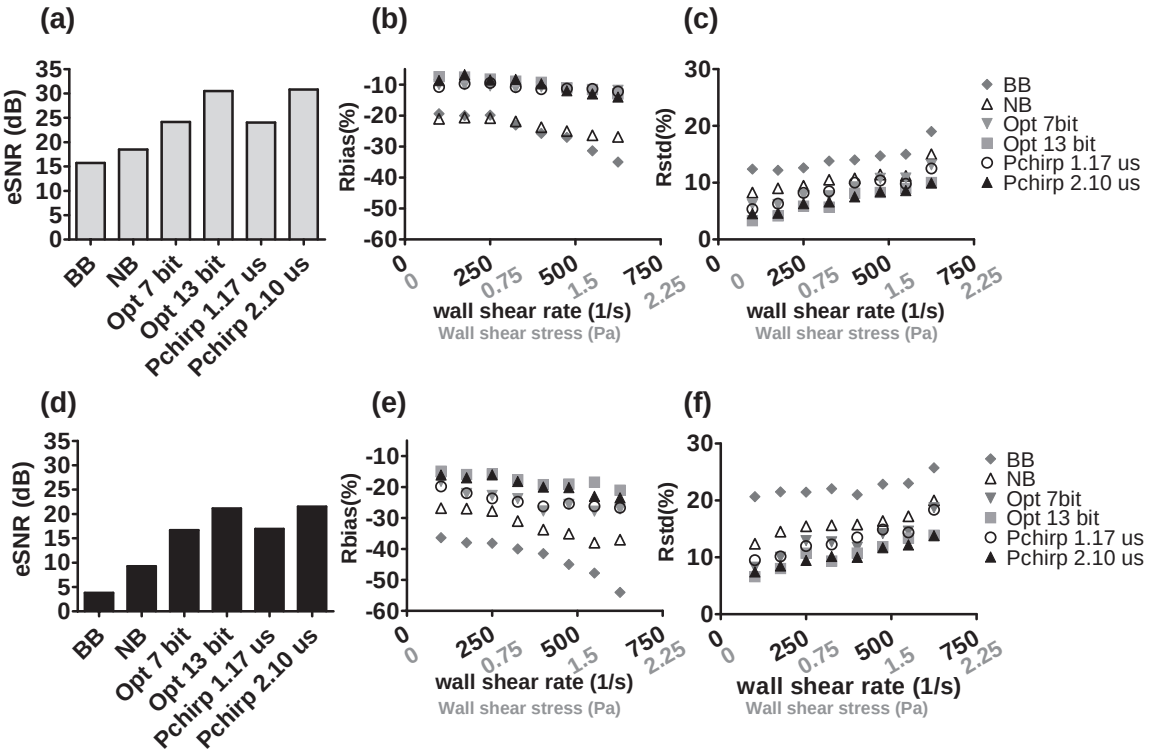

Figure 33. eSNR and WSR errors for various pulses with two transmission voltages: 15V (a-c) and 5V (d-f). Note that the abscissas in panels (b, c, e, f) can be converted from WSR to WSS (Pa) by multiplying the WSR values by the viscosity of the blood-mimicking fluid, 3 mPa-s.

4.8.1. Shear rate images acquired at carotid and brachial arteries

Shear rate images were acquired *in vivo* from the left common carotid artery and left brachial artery of a healthy volunteer using the Siemens Antares system. Echo acquisition was ECG triggered at peak systole and end diastole to obtain similar flow conditions for comparing imaging pulses. Fig. 34 shows the shear rate imaging data

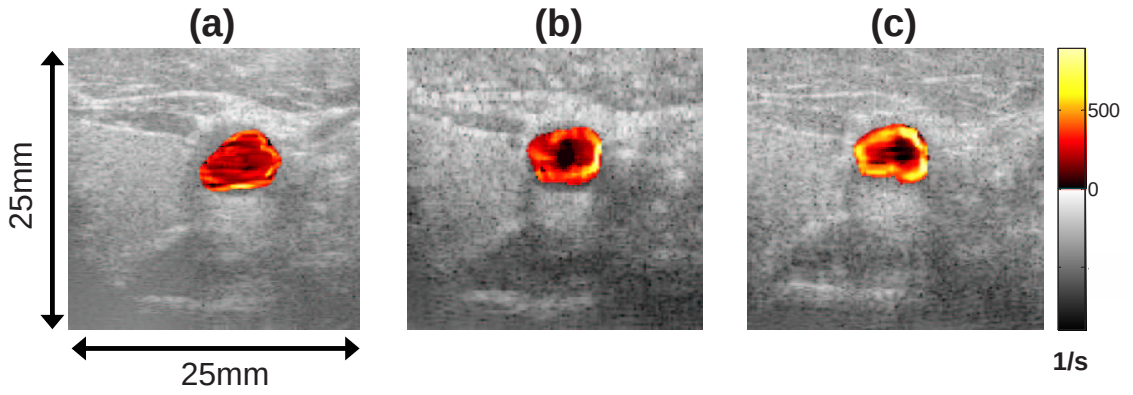

Figure 34. Shear rate images of a carotid artery at peak systole using (a) broadband (b) narrow-band and (c) 7-bit Optimal coded pulses.

as a color overlay on the B-mode image. Part a is the uncoded broadband pulse, part b is the uncoded narrow-band pulse and part c is the 7-bit Optimal coded; all are imaging the same carotid artery at peak systole. The broadband imaging pulse of part a clearly does not provide enough eSNR for reliable WSR estimates. The improved eSNR for the narrow-band pulse in part b gives a realistic pattern for WSR (the values of shear rate decrease at regions close to the center of the vessel) but with a poor spatial resolution that often biases low the WSR estimates. The coded pulse in part c hints at improved spatial resolution and clearly shows a more uniform pattern of WSR around the vessel. The WSR patterns for the 1.17μs pseudo chirp code were very similar to that of the 7-bit Optimal coded pulse shown in part c.

Fig. 35 shows representative in vivo shear rate images of a normal carotid and brachial artery using a 13-bit Optimal coded pulse measured at peak systole and end diastole. The shear rate patterns around the vessel are not symmetric, which could

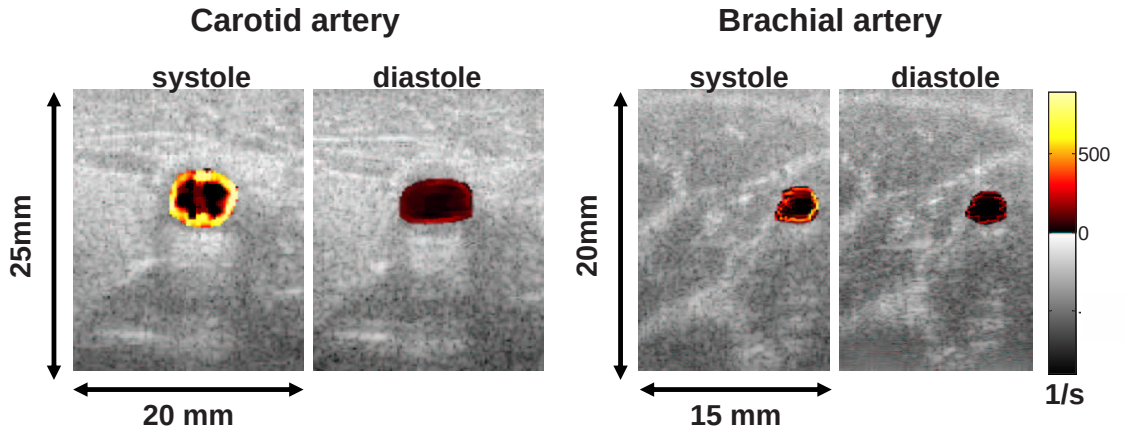

Figure 35. Shear rate images of human carotid and brachial arteries at peak systole and end diastole using 13-bit Optimal code.

indicate the spatially varying patterns of interest in the present study. For example, note the enhanced WSR values in the lower right quadrant of the brachial artery in systole. However, further study is necessary to validate these findings. Table 5 shows the estimated mean wall shear rates and the corresponding standard deviations averaged over 20 cycles from our volunteer. Since there are no standard comparisons for *in vivo* results, we can compute only standard deviations but not bias. Table 5 shows that higher energy pulses yield the smallest standard deviations and the highest means. Since we found that bias is always negative for WSR estimates, the inference is that both systematic and random errors are decreased using large-bandwidth coded pulses.

Table 5. In vivo estimates of wall shear rate from one normal subject

	Left common carotid artery		Left brachial artery	
Pulse type	Systole	Diastole	Systole	Diastole
	mean±std	mean±std	mean±std	mean±std
Broadband	590±88	137±64	458±66	128±51
narrow-band	729±63	154±57	574±47	163±43
Opt (7 bit)	785±37	173±25	699±33	187±29
Pchirp (1.17 μs)	773±52	198±30	703±32	204±35
Opt (13 bit)	853±32	219±21	710±21	213±22
Pchirp (2.10 μs)	820±41	225±23	743±25	219±19

4.9. Summary and Discussions

This chapter demonstrates the use of coded-pulse excitation techniques combined with a broadband regularized velocity estimator for wall shear rate estimation on a commercial ultrasonic system. Improved eSNR leads to improvements in the precision and accuracy of WSR estimates over a wide range of wall shear stresses (0.3 - 1.9 Pa). The advantages of our methods over standard Doppler techniques for estimating WSR are due to the use of broadband coded pulses with high time-bandwidth product, which match or exceed the eSNR of Doppler methods but with significantly greater bandwidth for enhanced spatial resolution. The nonstationary echo signals and decorrelation from flow distorts the codes but not sufficiently to generate range lobes during pulse decoding. A broadband velocity estimator that is regularized by a smoothness penalty obtained from color-flow information measured at the center of

the blood vessel is an important element in reducing estimation noise.

The pseudo-chirp and PM codes of similar pulse duration performed similarly. Unlike FM chirp pulses consisting of sine waves, FM pseudo chirp pulses are composed of square waves that provide more signal energy (in harmonics) for the same pulse length. The high pulse-energy density of the pseudo chirp is comparable to the PM Optimal coded pulse, and the high bandwidth of linear array systems provides access to the information from the harmonics. These coded pulses are able to significantly increase eSNR and bandwidth for velocity estimation before reaching a pulse duration where range lobe generation from incomplete decoding begins to significantly degrade contrast resolution. The WSR images in Figs. 34 and 35 suggest that in vivo imaging with real-time acquisition is possible, although the images presented in this report were generated off-line.

The results of Fig. 33 showed that increasing the transmission voltage improved eSNR for all imaging pulses and reduced the relative advantages of coded excitation regarding WSR bias and variance. Provided that eSNR <30 dB, pulsed excitation offers significant advantages (Fig. 11). We found it difficult to achieve eSNR > 30 dB *in vivo* while remaining within recommended output limits. Consequently coded-pulse excitation is potentially advantageous in many vascular imaging situations.

In summary, broadband coded-pulse excitation techniques can significantly reduce errors in the use of ultrasound when assessing endothelial cell function. Wall shear rate imaging provides a new dimension in monitoring spatial heterogeneity in hemo-

dynamic shear. These methods offer new tools for *in vivo* investigations into the effects of wall shear stress in the development of atherosclerotic disease.

5. REGULATION OF INFLAMMATORY RESPONSE IN HUMAN AORTIC ENDOTHELIAL CELLS UNDER SHEAR FLOW

5.1. Objectives

In previous chapters, we proposed a method using broadband coded-pulse excitation techniques to achieve high spatial resolution as well as high echo signal-to-noise ratio in ultrasonic shear flow imaging application. The techniques were implemented onto both our in-house laboratory ultrasonic system and a commercial scanner. This method was evaluated on both systems by a series of phantom studies with well-defined WSS fields and showed promising results in improving the accuracy and precision in wall shear rate estimation. As we showed a dramatic reduction in ultrasonic shear measurement errors using the new method, some important questions still remain unanswered. How do WSS measurement errors would effect the way we interpret the shear-regulated EC function both *in vitro* and *in vivo*? Does improvement in the accuracy and precision in shear estimation translate into significant improvements in our ability to assess shear-regulated EC function? Unfortunately, there is no literature available showing the impact of WSS errors on endothelial cell function, especially in regard to the inflammatory response that closely relates to the initiation of atherosclerosis. Also, there is a lack of information on the fundamental issue: How is CAM expression and leukocyte recruitment regulated on inflamed endothelium along a continuous gradient of WSS. As we will show CAM expression is

not a linear function of WSS, and therefore the errors in correlating ultrasonic WSS measurement errors to EC function depend on the values of WSS. This suggests we focus our attention on signal processing improvements to a specific WSS range to have the greatest diagnostic impact. This chapter describes our efforts at investigating the influence of shear magnitudes and gradients on cultured human aortic endothelial cell (HAEC) function using a specially designed microfluidic Hele-Shaw linear shear flow chamber.

5.2. *In vitro* approaches for investigating shear-regulated HAEC functions

5.2.1. Cell culture

Human aortic endothelial cells (Cascade Biologics, Portland, OR) at the fifth passage* were grown in tissue culture flasks with Medium 200 (Cascade Biologics) containing 2% fetal bovine serum (FBS, Cascade Biologics) and PSA solution (containing 100U/ml Penicillin G, 100 μg/ml Streptomycin and 0.25 μg/ml Amphotericin B). HAECs were cultured in a humidified incubator that provided an atmosphere of 95% air and 5% CO_2 at 37^{o}C. In order to facilitate cell deposition, the 35 mm-diameter glass cover slips were pre-coated with 1% (wt/vol) sterile aqueous gelatin solution, followed by seeding HAECs onto the surface at a density that yields confluent mono-

*Passage number refers to the number of times the cells have been subcultured. Primary culture at passage 0 is that stage of a cell culture following the isolation of the cells before the first subculture.

layers within 3 days. The medium was changed daily. Flow experiments were initiated on the day after cells had reached confluence. Compared with early passage (p3-7) cells, late-passage (p28-32) endothelial cells have been found to diminish cell proliferation, Akt phosphorylation, and secretion of smooth muscle cell chemoattractants in response to fluid shear.[77] In order to minimize these aging effects on shear-regulated endothelial cell function, cells from early passage p6-7 were used in this series of study.

5.2.2. Design and manufacturing of the Hele-Shaw microfluidic flow chamber

In order to investigate the change in EC function over a broad range of WSS in one experiment, a modified PPFC that delivers a linear decrease in fluid shear field from the inflow to the outflow was developed. With this flow system, it is possible to study EC function over a wide shear range with high spatial resolution while maintaining a constant shear gradient within a single chamber. This chamber was used to study the TNF-α-stimulated upregulation of vascular CAMs (ICAM-1, VCAM-1 and E-selectin) and leukocyte recruitment efficiency with respect to exposed WSS and spatial shear gradients in cultured HAEC.

Microfluidic flow system design: The design of the flow chamber was adapted from Usami et al.[78] based on Hele-Shaw flow theory. By setting the side walls of the flow chamber to be coincident with the streamlines of a two dimensional stagnation flow, and making the end of the channel shaped to match the iso-potential lines,

this configuration permits the WSS to decreases linearly along the center line of the channel (Fig. 36 c). At the end of the channel is a stagnation point and therefore the corresponding WSS is zero. The channel width w is a function of axial distance (x) and is designed using Eq. 28,

$$w(x) = w_1 \frac{L}{L - x}, \tag{28}$$

where w_1 is the entrance width, L is the total length of the channel, x is the distance measured from the channel entrance.

Then the WSS (designated τ_w to indicate surface shear stress at channel width w) along the center line of the flow channel is

$$\tau_w = \frac{6\mu Q}{h^2 w_1}(1 - \frac{x}{L}), \tag{29}$$

where Q is the volumetric flow rate, μ is the viscosity of the flow medium, and h is the height of the channel. The dimension of the flow chamber used in this study consists of the following parameters: h=100μm, w_1=2mm, L=20mm.

As shown in Fig. 36a, the design of the flow chamber consisting of two major components: (I) the Hele-Shaw flow chamber and (II) the vacuum channel network with a spider web-like pattern that serves to seal the flow chamber onto the cell-seeded cover slip surface.

Fabrication of the flow chamber master on a silicon wafer: The flow chamber pattern (Fig. 37 a) was first created using AutoCAD or Freehand (Macromedia) and

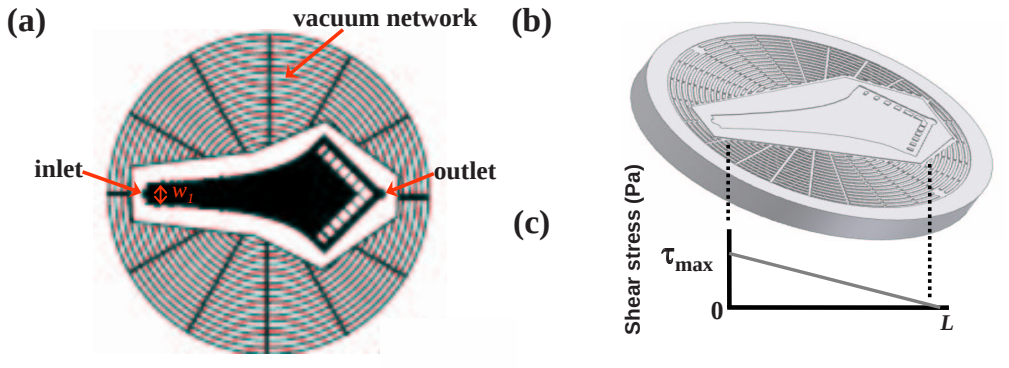

Figure 36. Diagram of the Hele-Shaw flow chamber. (a) The design of the flow chamber master that consists of a Hele-Shaw flow chamber and a vacuum network. (b) The PDMS flow chamber mold and the corresponding wall shear stress τ_w along the center axis of the flow channel.

printed onto a transparency to serve as a photomask in UV-photolithography to generate the master. In this procedure, the silicon wafer is served as a substrate and is cleaned with diluted acid and DI water prior to the coating process. A thin layer of negative photoresist SU-8 50 (MircoChem) was spin-coated onto the substrate at 1000 rpm for about 30 sec to reach a final thickness of 100 μm. The substrate with photoresist is then baked at 65 ^{o}C and then 95 ^{o}C for 10 minutes each to evaporate the solvent and densify the photoeresist film. Then the 100 μm thick photoresist layer is exposed to UV light (350-400 nm) through the photomask (flow chamber pattern) for 90 sec. It is important to avoid over-exposure that can result in fractures on the photoresist surface causing problems such as rough surface, open channel leaking, and photoresist layer detachment. Following the UV exposure, a two-step

post exposure bake (2 minutes at 65 ^{o}C and 5 minuteThe viscosity of these samples were measured at 95 ^{o}C) must be performed to selectively cross-link the exposed portions of the film. After the substrate slowly cools down to room temperature, it is then immersed in a small amount of a developing reagent for about 12 minutes to dissolve the uncrosslinked regions (previously masked). Following development, the substrate is then rinsed briefly with isopropyl alcohol and then dried with a gentle stream of air or nitrogen. The result structure functioned as a master for fabricating PDMS molds.

Fabrication of the PDMS flow chamber molds: A mixture of PDMS prepolymer and curing agent (mixed at 10:1 ratio, Slygard 184 kit, Dow Corning) was poured onto the master from the previous section. The mixture is left to cure at 75 ^{o}C for 1 hour. The PDMS is then peeled off from the master to produce a replica of the flow chamber design. The final flow chamber (ex: Fig. 36 b) is transparent and could be placed under microscope for visual observation during the flow experiments.

5.2.3. Viscosity measurement

Tsuboi et al.[17] have shown that EC function is mainly regulated by WSS instead of shear rate. In this case, it is very important to have an accurate estimate on the medium viscosity in order to correctly correlate EC function to corresponding shear stress. In order to expand the range of applied WSS range, the viscosity of the flow medium (Leibovitz, L-15, GIBCO) is elevated to that of the whole blood (3.2 mPa-s,[45] by adding Ficoll PM 70 (Amersham Biosciences). This viscosity range can not

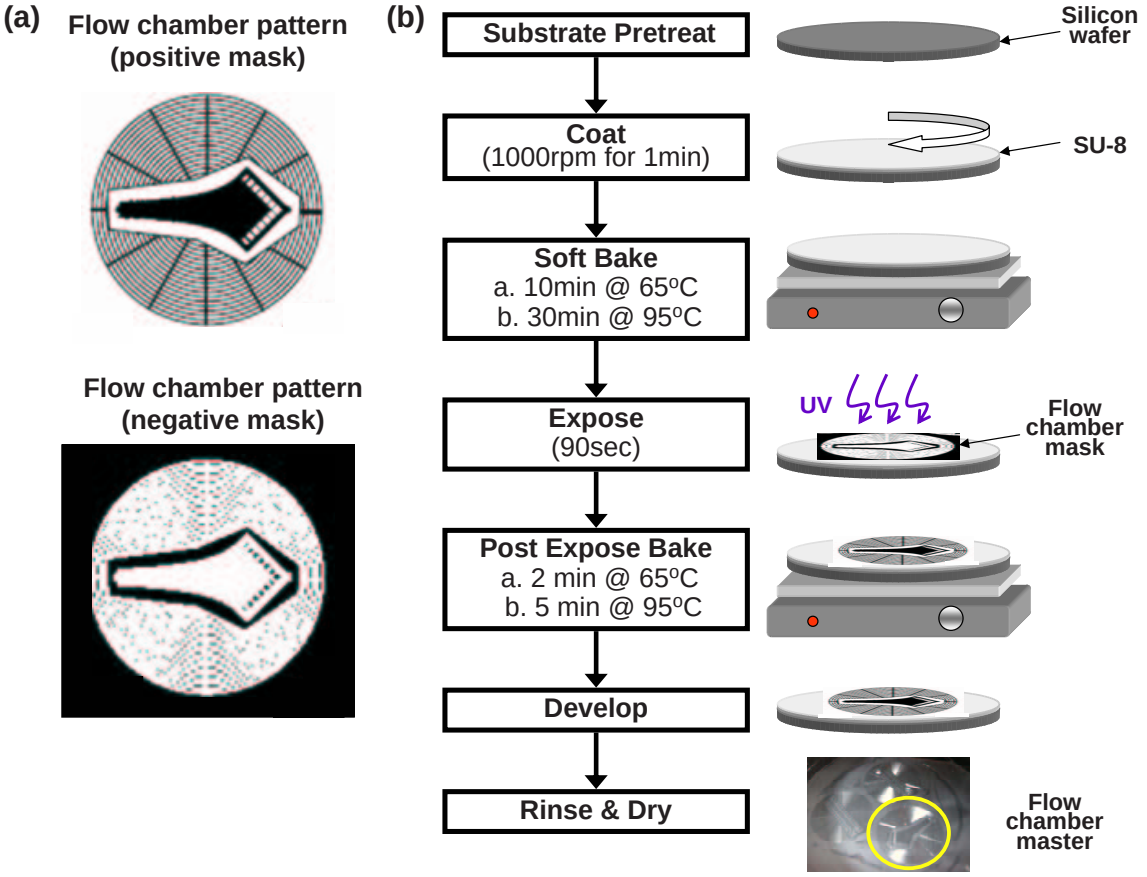

Figure 37. Fabrication process of making microfluidic flow chamber master. (a) flow chamber patterns. The choice of positive or negative photo masks depends on the type of the photoresist used as the coating. A negative photoresist SU-8 50 is used and thus a negative mask is applied. (b) Fabrication process of a flow chamber master including coating photoresist and etching the flow chamber pattern.

be measured by most digital cone-plate viscometers because the rotor and sensor sets were designed for measuring the viscosity for more viscous samples such as paste or gel. The low sensitivity in such viscosity range is a result of insufficient surface area

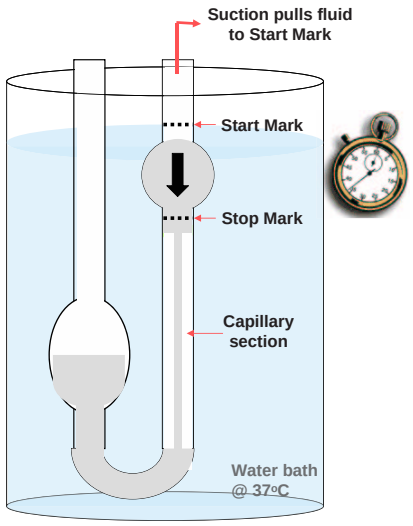

Figure 38. Experiment setup for measuring the viscosity of the flow medium.

between the cone and plate. The estimated viscosity from these digital viscometers were always a few folds higher than the true values. Surprisingly, the most accurate method for measuring low viscosity samples is to use a glass Ostwald viscometer, which is recommended in most of the mechanical textbooks for measuring liquid viscosities. Ostwald viscometer is an U shape glassware that includes a reservoir at the wider tube side, along with a reservoir and a thin capillary at the narrow tube side (Fig. 38). The Ostwald viscometer was held vertical and placed in a big beaker filled with water to maintain temperature at a constant value. An 1 ml of solution sample was pipetted into the viscometer through the wider tube side and incubated in the water bath for at least 5 minutes to reach the desired temperature. A pipet bulb was attached to the end of the narrow tube to suck the sample into the reservoir at the narrow tube side. Once all the liquid was in the reservoir, the pipet bulb was

then removed and the liquid started leaving the reservoir through the capillary due to gravity. With the Ostwald viscometer, the amount of hydrostatic pressure driving the liquid through the capillary depends on the height (h), and the density (ρ) of the liquid, and the acceleration due to gravity (g). This pressure represents the shearing stress. The rate of flow of the liquid through the capillary represents the rate of shear. Therefore, the viscosity of a liquid is proportional to the hydrostatic pressure divided by the volume of fluid that flows through the capillary per unit time. By using the same experiment setup, h, g and the sample volume are maintained constant. In this way, the ratio of the viscosity of two samples is equal to the ratio of the time each sample takes to pass through the viscometer multiplied by the density (Eq. 30).

$$\frac{\mu_{ref}}{\rho_{ref} t_{ref}} = \frac{\mu_{sample}}{\rho_{sample} t_{sample}} \tag{30}$$

In our experiments, water is used as the reference medium. The calibration parameters were calculated by measuring the time for water to pass through the capillary section at temperatures of 25, 30 and 35^{o}C, where the corresponding viscosities are available in literature.[79] The samples are L-15 medium mixed with different concentrations of Ficoll PM 70. The viscosities of these samples were measured at 37 ^{o}C, which is the same temperature as that in the shear flow experiment. The measured viscosities are listed in Table 6. The viscosity of the flow medium (15% Ficoll in L-15 medium) used in the shear flow experiment is 3.264 $\pm$ 0.13 mPa-s.

Table 6. Measured viscosities of the flow medium samples

Samples	density ρ (g/cm^3)	Temp (^oC)	Time (sec)	viscosity (mPa-s)
DI water (ref1)	0.99	25	82.25	0.89
DI water (ref2)	0.99	30	75.75	0.79
DI water (ref3)	0.99	35	70	0.72
DI water	0.99	37	67.33 $\pm$0.57	0.710 $\pm$0.006
Leibovitz (L-15) medium	0.99	37	65.75$\pm$0.50	0.693 $\pm$0.005
7.5% Ficoll PM70 in L-15	1.075	37	140.75 $\pm$3.30	1.597$\pm$0.038
15% Ficoll PM70 in L-15	1.15	37	269 $\pm$11.50	3.264$\pm$0.130

5.2.4. Shear flow experiment

L-15 medium was used as the flow medium so that the pH could be properly maintained at 7.4 during the flow experiments without additional CO_2 supply. The viscosity of the flow medium was maintained constant throughout the study, and the two different flow rates of 0.1 and 0.07 ml/min were used to generate two different shear stress fields: 0-1.63 and 0-1.14 Pa.

One hour prior to the flow experiments, the incubation cell medium was switched to L-15 medium containing 0.2% FBS to slow down the cell cycle. The sterile filtered flow medium was placed into a vacuum chamber for 10 minutes to remove air bubbles generated during the mixing process. In order to mimic the condition of inflammation in selected experiments, HAECs were continuous exposed to TNF-α (R & D) at the concentration of 30 U/ml (0.43 pg/ml) by adding TNF-α into the flow

medium in the syringe right before the start of the flow experiments. TNF-α is an important mediator of the inflammatory processes that occur during the progression of atherosclerosis.[34] Produced by macrophages that infiltrate the lesion, cytokine such as TNF-α are known to induce the expression of many endothelial genes that contribute to the complex processes involved in atherogenesis.

The PDMS flow chamber and the inlet tubing were washed with ethanol and then sterilized with UV light and ozone for 20 minutes before usage. The inner surface of the flow channel was wetted with phosphate-buffered saline (PBS) and all the trapped air bubbles were cleared. The cover slip was carefully placed on the flow chamber with the cell side facing toward it. Then vacuum was turned on to create reversible but strong bonding between the cover slip and the flow chamber by generating a negative pressure inside the vacuum network. The tubing was inserted into the flow entrance and the outlet (Fig. 39). After four hours of shearing, the cover slip was carefully removed from the flow chamber without harming the cells, and then washed with a mixture of 0.2% human serum albumin (HSA) and Hepes buffer (HHB, 30mM Hepes, 110mM NaCl, 10mM KCl, 1mM MgCl2, 0.2% glucose, pH 7.4) to clean out the flow medium residue.

5.2.5. Immunofluorescence microscopy

Fluorescein (FITC) labeled monoclonal antibodies (mABs) VCAM-1 (CD106, 50μg/ml) and E-selectin (CD62E, 50μg/ml) were obtained from R & D systems (Minneapolis, MN). ICAM-1 mAB (CD54, 200μg/ml) and the control markers (mouse IgG_1 and

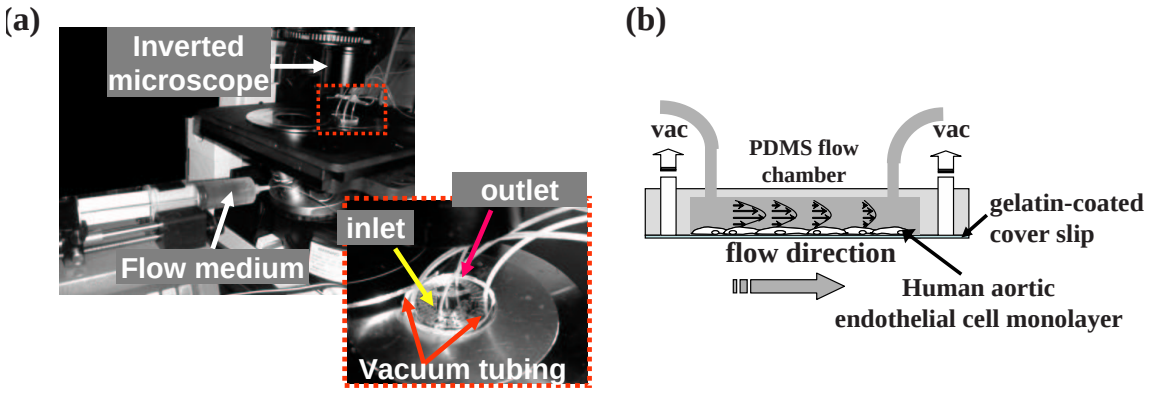

Figure 39. In vitro shear flow experiment on cultured human aortic endothelial cell monolayer.

mouse IgG_{2a} 100μg/ml) were purchased from Caltag, Burlingame, CA. For microscopic visualization of cell surface-associated proteins, cells were washed and incubated on ice for 20 minutes with specific mABs mixture (10μl of mAB in 200μl of 2% HSA with HHB buffer) as described above, and followed by secondary labeling using Qdot 605 protein A conjugate (Quantum Dot, Hayward, CA) (2μl of 4.0 μM Qdot 605 in 200 μl of 2% HSA with HHB buffer) that provided a better image contrast by emitting stronger and slower photo-bleached fluorescent signals. Then the HAEC monolayers were fixed in fresh-made 2% sterile paraformaldehyde for 20minutes on ice and covered from light. A fair amount (5 ml) of 0.2 % HSA with HHB was used to wash out the paraformaldehyde to prevent autofluorescence artifact. The cover slips were carefully placed and sealed onto the microscope slides. Fluorescence images were acquired within 24 hrs using a fluorescent reverse phase microscope with emission filter set at 546 nm. Due to the spatial variation in shear stress field, the number of ECs

in the region of interest for specific shear range was insufficient for flow cytometry. An alternative method was utilized to obtain the quantitative fluorescence intensity measurements through immunofluorescence microscopy by calculating the mean fluorescence intensity (MFI) in each field of view. The averaged intensity was estimated from eight to ten images that were acquired randomly around the region of interest.

5.2.6. Monocyte isolation

Heparin-anticoagulated whole blood was collected from healthy volunteers. Monocytes were first isolated using sedimentation over Lymphosep density separation medium (MP, Aurora, OH). Then the obtained monocytes were purified from platelets by resuspending in 2% HSA with HHB buffer and centrifuging the cell solution at 950 RPM until most of the platelets were removed. By using the negative isolation method with magnet beads (Dynal, Brown Deer, WI), monocytes were further purified from neutrophils and lymphocytes. The final working concentration of monocytes was controlled at 10^6 monocytes/ml by resuspending cells in 2% HSA with HHB. Ca^{2+} was also added to the monocyte solution to maintain a concentration at 1mM.

5.2.7. Neutrophil isolation

The protocol of isolating neutrophils from human blood is similar to the one used for monocyte isolation. Neutrophils were first isolated from heparin-anticoagulated whole blood using sedimentation over the PMN isolation medium (Matrix). Then the concentrated neutrophils were resuspended in HHB containing 1mM Ca^{2+} and 0.2% HSA to reach the final concentration of 10^6 neutrophils/ml.

5.2.8. Leukocyte recruitment assay

In order to observe the effects in recruiting leukocyte efficiency into endothelium caused by pre-shearing the HAEC monolayer, the leukocyte flowing over the EC surface has to be controlled at a constant rate. However, due to the geometry of the linear shear flow chamber, the flow velocity varies at different locations, although the volumetric flow rate for each cross sectional plane remains the same. Two additional flow chambers consisting of three separate parallel rectangular flow channels (300μm (w_p) x 100 μm (h_p) x 1 cm (L_p)) were created to investigate the effect of pre-shearing EC monolayers on dynamic EC-leukocyte interactions. After four hours of shearing, the original linear shear flow chamber was carefully removed from the cover slip, and HAEC monolayer were washed with HBSS thoroughly in preparation for the next experiments. In the first set of experiments, the channels were placed perpendicular to the original flow direction, where the EC were exposed to the same shear stress magnitude (the shear stress is the same for the lateral cross sectional plane in the original linear shear flow chamber). Therefore, the leukocytes would encounter the endothelial monolayer that has been sheared at the same specific shear magnitude (Fig. 44 a). With this setup, the leukocyte adhesion assay was performed independently for each interested shear stress level. On the other hand, we also considered the possible influence on EC-leukocyte interactions due to the spatial varied shear-mediated CAM expression. Therefore, the flow chamber used in the second set of experiments was placed on top of the pre-conditioned monolayer where the rectangular channels were properly aligned to let monocytes flow over the monolayer parallel

to the original shearing direction (Fig. 45 a). The reservoirs for adding leukocyte solution were modified from 20G needles, and were inserted into the entrance of the flow channel. The syringe connected to the outlet of the channel withdrew liquid from the flow channel creating a negative pressure to let the leukocyte enter the channel. The result shear stress when leukocyte flows though the flow channel can be estimated via,

$$\tau_w = \frac{6\mu_L Q_L}{w^2 h} \tag{31}$$

The viscosity of the leukocyte solution μ_L was approximated to that of water (1 mPa-s). The input flow rate Q_L was set to 6μl/min to create a shear field of 0.2 Pa. For each flow channel, five image sequences (one minute each) were recorded at a refresh rate of 2 frames per second. The images were manually analyzed offline.

5.2.9. Statistical analysis

Results are expressed as mean ± standard error of measurement (SEM). Statistical significance was determined by using Student's t-test for two groups of data. The level of statistical significance was defined as $p < 0.05$ from 3 to 6 separate experiments.

5.3. Experiment results of *in vitro* shear-regulated endothelial cell function

5.3.1. Cytokine-induced endothelial CAM expression

The shear-regulated CAM expression was measured as a function of distance down the flow channel in which WSS linearly decreases from 1.6 Pa at the inlet to essentially

zero at the exit (Fig. 36). This WSS range was chosen to model the transition from atheroprotective (i.e. = 1.2 Pa) to athero-prone (i.e. = 0.4 Pa) conditions as defined in previous studies.[5] Representative images of ICAM-1 immunofluorescence depicted in Fig. 41 correspond to distances 3, 6, 12 and 18 mm downstream of the chamber inlet. CAM expression was quantified by image analysis over these distinct $\sim$ 1 mm^2 regions of the HAEC monolayer after 4hr of TNF-α in the presence of laminar WSS. An increase in MFI is observed with increased WSS, however, the elongation or realignment of HAEC was not apparent.

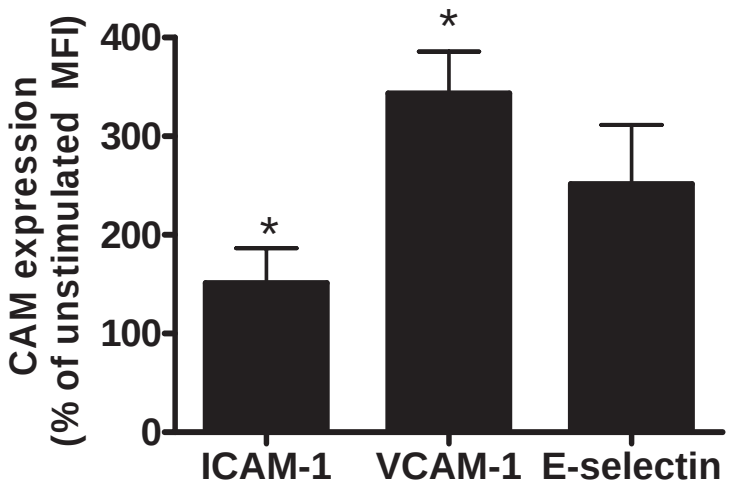

Figure 40. TNF-α induces ICAM-1, VCAM-1 and E-selectin expressions. The controls are defined as the mean fluorescence intensity of the unstimulated endothelial cells under the static condition. $*p < 0.05$

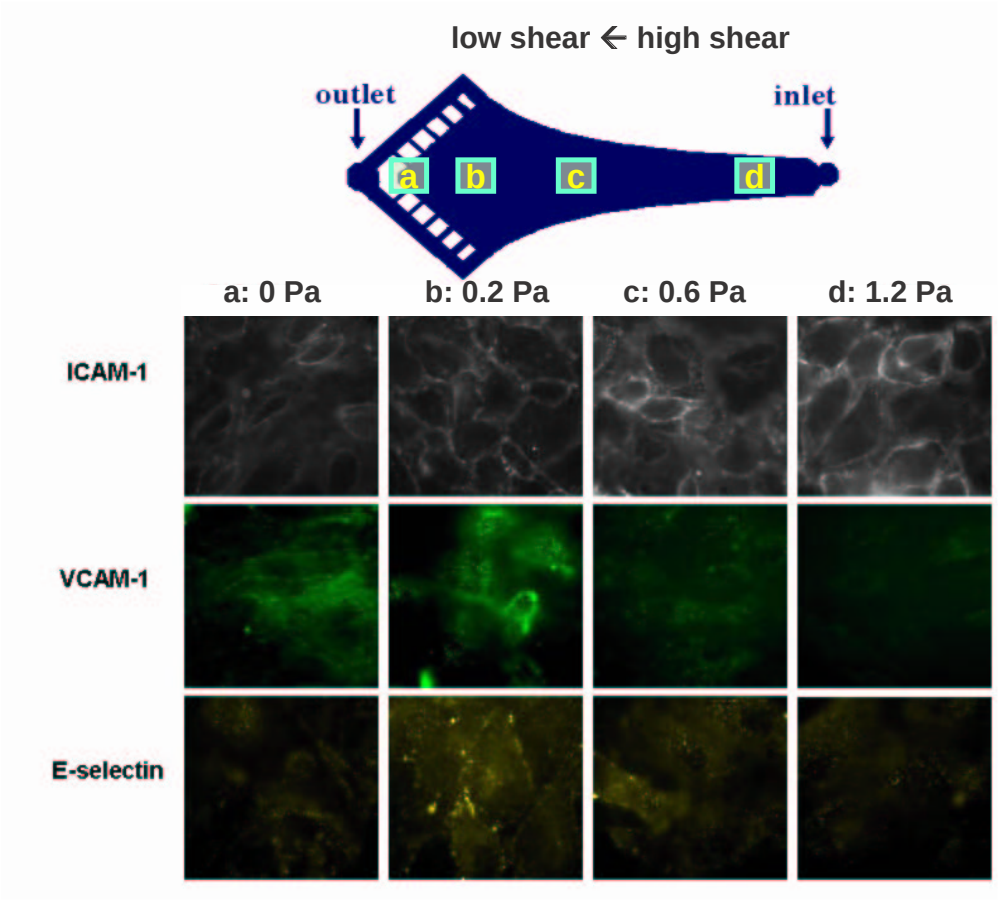

Figure 41. Representative immunofluorescence images of ICAM-1,VCAM-1 and E-selectin surface expression down a linear shear field. Images (size not scaled) are oriented parallel to the flow stream lines and are sampled from regions as indicated in the schematic: (a) static (b) 0.2 (c) 0.6 and (d) 1.2 Pa.

5.3.2. Shear-regulated endothelial CAM expression

In order to investigate the relative change in CAM expressions caused solely by shearing and cytokine stimulation, non-specific binding MFI baseline estimated from the images of HAEC labeled with control markers was subtracted from the images. As shown in Fig. 40, in the presence of TNF-α (30U/ml) stimulation under static con-

ditions, VCAM-1 expression was amplified by almost 3-fold, whereas ICAM-1 and E-selectin was amplified by 0.5-fold and 1.5-fold, respectively. The relative change in CAM expression as a function of WSS was computed by normalizing the MFI of EC at each position by the unstimulated value measured under static conditions (Fig. 42). Shear alone resulted in a $\sim$1.1-fold increase in ICAM-1 expression at high WSS. In contrast, VCAM-1 and E-selectin expression was not significantly altered by WSS.

TNF-α-induced ICAM-1 expression increased linearly along the WSS gradient rising $\sim$3.5-fold above static conditions, before reaching a plateau at $\sim$0.9 Pa (Fig. 42 a). VCAM-1 and E-selectin exhibited a very different response in that maximal amplification of 3.6-fold and 1.6-fold were detected at positions corresponding to 0.2 and 0.4 Pa, respectively (Fig. 42 b, c). Beyond this region, VCAM-1 and E-selectin decreased with increase in exposed WSS. When WSS $>$ 0.8 Pa , VCAM-1 and E-selectin expression was suppressed below that induced by TNF-α stimulation under static conditions. These data indicate that WSS has a potent and differential effect on the transcriptional process initiated by TNF-α stimulation.

Mapping of shear-mediated CAM expression suggested that changes $<$ 0.1 Pa can alter cytokine-elicited CAM expression. In order to determine more precisely the spatial effect of WSS on HAEC inflammatory response, immunofluorescence of CAM expression was analyzed at a 10-fold higher spatial resolution along the shear gradient (Fig. 42 d-f). Images were collected at 180 μm increments down the channel, corresponding to a 0.017 Pa decrease in WSS over the area of HAEC analyzed. Analysis was focused on the regions of the flow channel in which the greatest rate of change

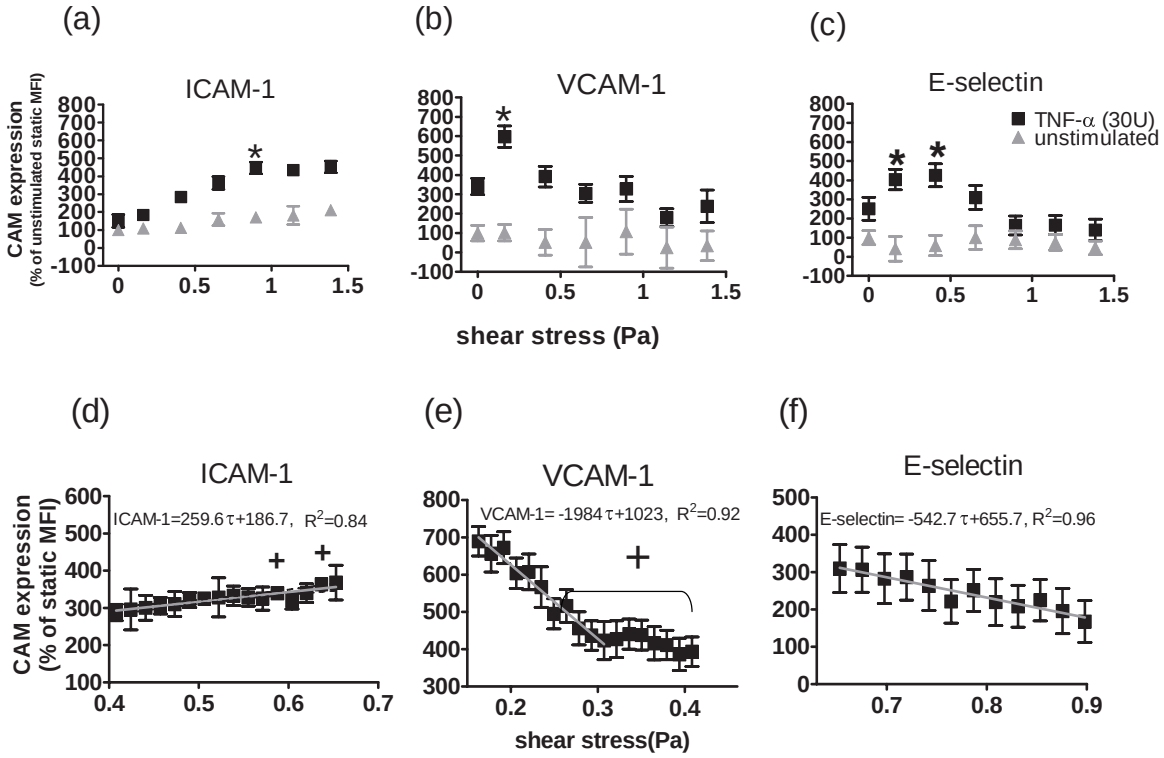

Figure 42. Spatial gradients in TNF-α induced CAM expression with shear stress in the Hele-Shaw chamber: (a) ICAM-1, (b) VCAM-1 and (c) E-selectin. The corresponding CAM expression acquired with fine stress resolution was plotted in d-f. Data are presented as a percentage change relative to unstimulated static controls. $*p < 0.05$ **versus stimulated static condition.**$+p < 0.05$ **versus the condition exposed to the lowest shear stress shown in the plots.**

of CAM expression was observed in Fig. 42 a-c. ICAM-1 expression measured over a shear range of 0.4-0.65 Pa revealed a linear increase at a rate of ∼250 %/Pa (Fig. 42 d). In a range in WSS from 0.16-0.4 Pa, VCAM-1 exhibited a much faster rate of

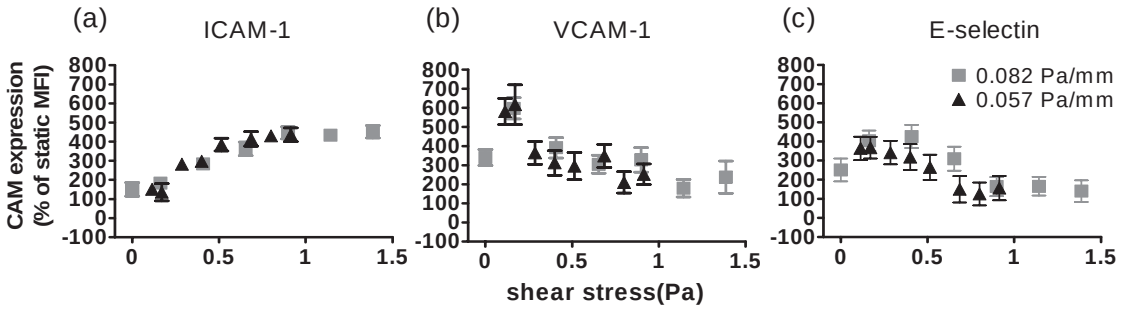

Figure 43. Spatial CAM regulation is dependent on the magnitude and not the gradient of applied shear stress. Two distinct spatial shear gradients 0.082 and 0.057 Pa per mm were applied. Varying spatial gradients in shear stress shows no significant alteration in CAM expression. Expression levels are compared with the unstimulated static controls

decrease in expression falling ∼2000 %/Pa (Fig. 42 e). Between 0.7-0.9 Pa, E-selectin decreased at a rate of ∼550 %/Pa (Fig. 42 f). These data indicate that VCAM-1 expression is down regulated with the highest spatial acuity in response to small fluctuations in WSS. For instance, we measured a 50% drop in VCAM-1 expression over a distance of ∼300 μm down the channel. This corresponds to ∼10 EC responding to a decrease in WSS of 0.025Pa. Consequently, these are the ranges of WSS at which improvements in ultrasonic measurements should be target for maximum diagnostic effect.

5.3.3. Influence of changes in spatial shear gradient on CAM expression

We next examined the sensitivity of the EC response to a 30% decrease in the WSS gradient by a commensurate drop in the input volumetric flow rate as defined by

Eq. 29. Thus, the maximum WSS dropped from 1.6 to 1.1 Pa and the gradient was reduced from 0.082 to 0.057 Pa/mm. CAM expression over the shallower spatial gradient is plotted in Fig. 43, at positions corresponding to the same WSS levels as measured in Fig. 42(a-c). Remarkably, no significant difference in shear-mediated CAM expression was observed, which indicates that the magnitude of WSS and not the rate of change dominates the regulation of acute TNF-α-induced CAM expression.

5.3.4. Leukocyte recruitment on a shear conditioned EC monolayer

It is well established that monocytes are recruited to sites of atherosclerosis with much higher efficiency than neutrophils.[9] Monocytes are enriched at vascular sites of plaque formation, but the role of WSS and differential regulation of CAM expression on recruitment efficiency remains obscure. Thus, we measured the multi-step process of leukocyte recruitment on HAEC that were stimulated with TNF-α and continuously exposed to a WSS gradient in the Hele-Shaw flow chamber. In order to shear monocytes or neutrophils at a constant stress of 0.2 Pa, a second flow chamber consisting of 3 independent rectangular flow channels was assembled over the pre-conditioned HAEC (Fig. 44 a). This facilitated imaging of leukocyte adhesion kinetics over regions pre-conditioned at WSS levels of 0.2, 0.6, and 1.2 Pa, as well as the static condition. Adhesion dynamics were obtained from five random fields for each region of the channel allowing quantification of the number of leukocytes engaging in slow rolling, cell arrest, and transmigration to a position under the HAEC monolayers. Rolling monocytes were arrested with greater efficiency than rolling neutrophils

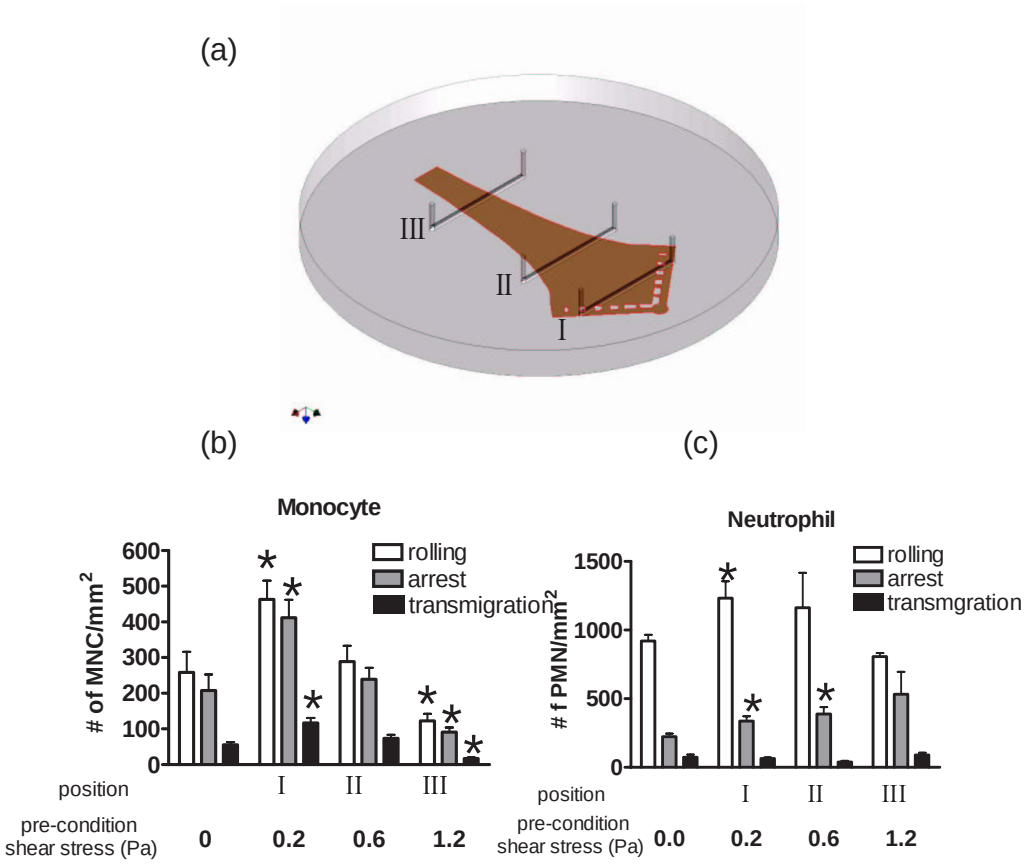

Figure 44. Leukocyte recruitment on inflamed HAEC preconditioned over a linear gradient of shear stress. Leukocytes at 10^6/ml were perfused perpendicular to the direction that monolayers were pre-sheared at positions corresponding to 0, 0.2, 0.6 and 1.2 Pa. The number of (b) monocytes (MNC) and (c) neutrophils (PMN) interacting with the endothelium were counted. $*p < 0.05$ **versus ECs in static condition.**

for all WSS conditions. The recruitment efficiency, defined as the ratio of leukocyte arrest to those rolling, was ∼1:1 for monocytes, whereas it was 1:3 for neutrophils over all WSS levels, except at 1.2 Pa where rolling numbers decrease and arrest ef-

ficiency reached a maximum (Fig.44 b, c). Efficiency of recruitment for monocytes reached 85% at region (I) and only slightly declined within regions pre-sheared at higher magnitude (i.e., 80% at 0.6 Pa, and 70% at 1.2 Pa). In contrast, neutrophil recruitment efficiency was ∼20% even though rolling numbers were highest within this region. Neutrophil adhesion efficiency reached ∼66% within region (III). These differences were observed despite the fact that the total number of interacting cells was comparable between neutrophils and monocytes over all regions preconditioned at different WSS magnitudes. Interestingly, monocyte recruitment and transmigration was comparable on EC monolayers stimulated under static conditions or pre-sheared at 0.6 Pa. In contrast, neutrophil recruitment efficiency and transmigration increased with the magnitude of WSS preconditioning.

In a separate set of experiments we examined monocyte recruitment flowing in a direction parallel to that of shear preconditioning, thereby analyzing effects on EC in a geometry that more closely mimics recruitment in the vasculature. As depicted in Fig. 45 a, the flow channels were aligned parallel to the pre-shearing direction in which HAEC were exposed to 0-1.6 Pa. Monocytes were again infused at a constant shear of 0.2 Pa and adhesive interactions over five fields were video recorded. Previous studies have shown that ECs start to elongate and align with the direction of laminar flow after only 3 hours of shear,[80] however, no difference in monocyte-EC interactions were detected for monocyte interaction with EC parallel to the direction of shear preconditioning (Fig. 45 b). This suggests the initial modification in EC morphology or interactions along the gradient of CAM have minimum impact on

monocyte recruitment.

A final analysis focused on how monocyte recruitment efficiency varies with position down the flow channel (Fig. 45 c). This analysis provides a map of recruitment efficiency as a function of the differential expression of CAMs. Shear stress at ∼0.7Pa emerged as a critical threshold for monocyte arrest. Monocytes recruitment efficiency increased significantly at pre-conditioned WSS below this threshold. This observation is consistent with the fact that both E-selectin and VCAM-1 expression were elevated within this shear range. Significantly, E-selectin reached the greatest rate of change in expression between 0.6-0.9 Pa. Thus, EC ligands for both monocyte capture and arrest are critical for optimum transition to stable adhesion and transmigration.

5.4. Summary and Discussion

Vascular hemodynamics, most notably WSS, has been established to be critical for maintaining vessel homeostasis. The anti-inflammatory action is attributed to mechano-transduction of shear response elements that regulate the transcriptional response to cytokines. The focal nature of atherosclerosis associating with regional low fluid shear and complex flow disturbances implies a central role for WSS, and possibly the spatial heterogeneity of the shear field in EC dysfunction contributing to atherogenesis. In this study, we discriminated between the effects of the magnitude and gradient of WSS in terms of the regulation of adhesion molecule expression on endothelium and subsequent monocyte recruitment over a physiological range of WSS (0-1.6 Pa) by using a modified PPFC with a well-defined spatially varying shear

field. A significant finding was that shear-modulated CAM expression in the inflamed HAEC was most responsive to the magnitude of shear but insensitive to a 30% change in the spatial gradient of WSS. We also discovered that a change in magnitude on the order of 0.025 Pa can be sensed by as few as ∼10 EC and elicit a 50% change in VCAM-1 expression. Monocyte recruitment, the key step in early atherogenesis, increased in direct proportion to the level of VCAM-1 and E-selectin, but was independent of ICAM-1 expression. In contrast, the efficiency of neutrophil recruitment was several-fold less than that for monocytes, except within regions of high WSS preconditioning where ICAM-1 expression was greatest. The implication is that these leukocyte subtypes are differentially recruited at vascular regions as a function of shear regulated CAM expression.

Mapping the response of TNF-α-stimulated CAM expression as a function of the distance down the linear shear flow channel with high spatial resolution (∼100 μm) revealed that each receptor exhibited a distinct expression pattern with preconditioning laminar WSS. However, shear alone only exerted subtle influence on the CAM expression level and was detected only for ICAM-1. Our observations of cytokine-stimulated CAM expression in response to fluid WSS are consistent with that of Chiu[15] and Tsao,[32] where attenuation in E-selectin and VCAM-1 expression was found after shearing the human umbilical vein endothelial cell monolayers at high shear (2 and 1.2 Pa). It also agrees with the findings of Mohan et al.,[16] where amplification in VCAM-1 expression was reported after shearing EC monolayer at low WSS (0.2 Pa). Similar upregulation pattern of ICAM-1 expression with increase in WSS

was reported by Tsuboi et al.[17] These studies were conducted at constant levels of WSS within the range of 0-2 Pa using conventional PPFC where the shear fields were uniform.[15–17,32] We present the first data of CAM expression mapped as a function of the rate of change in laminar WSS on a single continuous endothelial monolayer using a microfluidic channel that requires lower numbers of EC and reagent volumes ($\sim \mu$l).

We observed that the greatest change in CAM expression on inflamed HAEC occurred within the low range in WSS from 0.2-0.4 Pa correlating with stress values found within vascular regions prone to atherogenesis.[5] In contrast, TNF-α stimulated CAM expression reached a steady state at WSS greater than 1 Pa, which reflects the quiescence of inflammatory response within the normal physiological range in arteries (i.e. 1.2 - 1.7 Pa). The implication on vessel homeostasis is that WSS has a direct influence on the regional progression of atherosclerosis. It is noteworthy that WSS induced significant alteration in CAM expression only when cytokine was present, thus highlighting the importance of inflammatory mediators in triggering atherogenesis.

VCAM-1 exhibited the greatest sensitivity and upregulation at low shear flow condition ($\sim$2 Pa) where ICAM-1 exhibited the smallest increase. Inflamed HAEC monolayers exposed to low WSS were most effective at recruiting monocytes, but not neutrophils. Gonzales et al.[26] reported a similar result for EC preconditioned at 0.2 Pa where monocyte adhesion increase 3-fold above static culture. Our data is first to show that neutrophil recruitment efficiency is greatest within regions of inflamed HAEC pre-exposed to a high WSS of 1.2 Pa. Leukocytes adhesive interactions are dependent

on the relative level of CAMs expressed on the EC membrane and the corresponding integrins and selectin receptors on the leukocytes. Leukocyte function-associated antigen-1 (LFA-1), very late antigen-4 (VLA-4) and P-selectin glycoprotein ligand-1 (PSGL-1) expressed on the monocytes are known to recognize ICAM-1, VCAM-1 and E-selectin on the HAEC surface, respectively. E-selectin is required for cell tethering and rolling, whereas ICAM-1 and VCAM-1 are receptors that mediate leukocyte arrest and transmigration.[81] The efficiency of monocyte arrest correlated directly with VCAM-1 expression and not ICAM, implying that VCAM-1 is the primary receptor mediating arrest. On the other hand, neutrophils predominantly express LFA-1 which binds with high affinity to ICAM-1. This was consistent with the observation that the efficiency of neutrophil recruitment was positively correlated to ICAM-1 expression pattern. The efficiency of capture and rolling for monocytes and neutrophils were both closely correlated to the expression pattern of E-selectin.

Our findings that monocyte recruitment efficiency varied directly with shear-regulated VCAM-1 expression might explain why VCAM-1, and not ICAM-1, is more important in atherogenesis[24] and why recruitment of monocytes occurs preferential over neutrophils.[9] The high sensitivity in regulation of VCAM-1 expression to small perturbations in a low WSS range over small distances ($\sim$170 μm) also underscores the focal nature of atherosclerosis in which plaque formation maps to regions of low WSS.[6] The prominent effect on CAM expression over small distance and WSS differences (0.01-0.02 Pa) suggests a minor influence of cell-cell communication or paracrine signaling from neighboring endothelial cells. The other important finding is that CAM

expression is dominated by the absolute magnitude of WSS rather than the spatial gradients in the unidirectional laminar WSS. However, one must consider that this interpretation might change in vivo or other *in vitro* systems due to different scales or patterns of spatial shear gradient,[82] time scales and the potential for more complex cellular interactions, such as influence from intima and smooth muscle cells.[15] Nonetheless, White et al.[31] also concluded that the spatial gradient in WSS is not the key factor for EC proliferation despite the fact that different flow profiles were investigated. Additionally, monocyte recruitment data reported by Chen et al.[30] support the concept that the spatial shear gradient is not the primary factor affecting monocytes arrest on the endothelium.

In summary, this chapter has established CAM regulation and leukocyte recruitment as a function of shear magnitude of unidirectional laminar flow with a constant spatial shear gradient. The data show that WSS has a direct influence in transcriptional regulation and expression of ICAM-1, VCAM-1, and E-selectin over small difference in stress on the order of 0.025 Pa and across ∼10 EC. VCAM-1 expression was most closely correlated with adhesion efficiency of monocytes and a threshold in stress mediated expression was found at $\sim$ 0.7 Pa. We conclude that the magnitude of shear forces imparted vascular regions of disturbed blood flow is a critical determinant in the spatial regulation of the endothelial inflammatory response and subsequent monocyte recruitment.

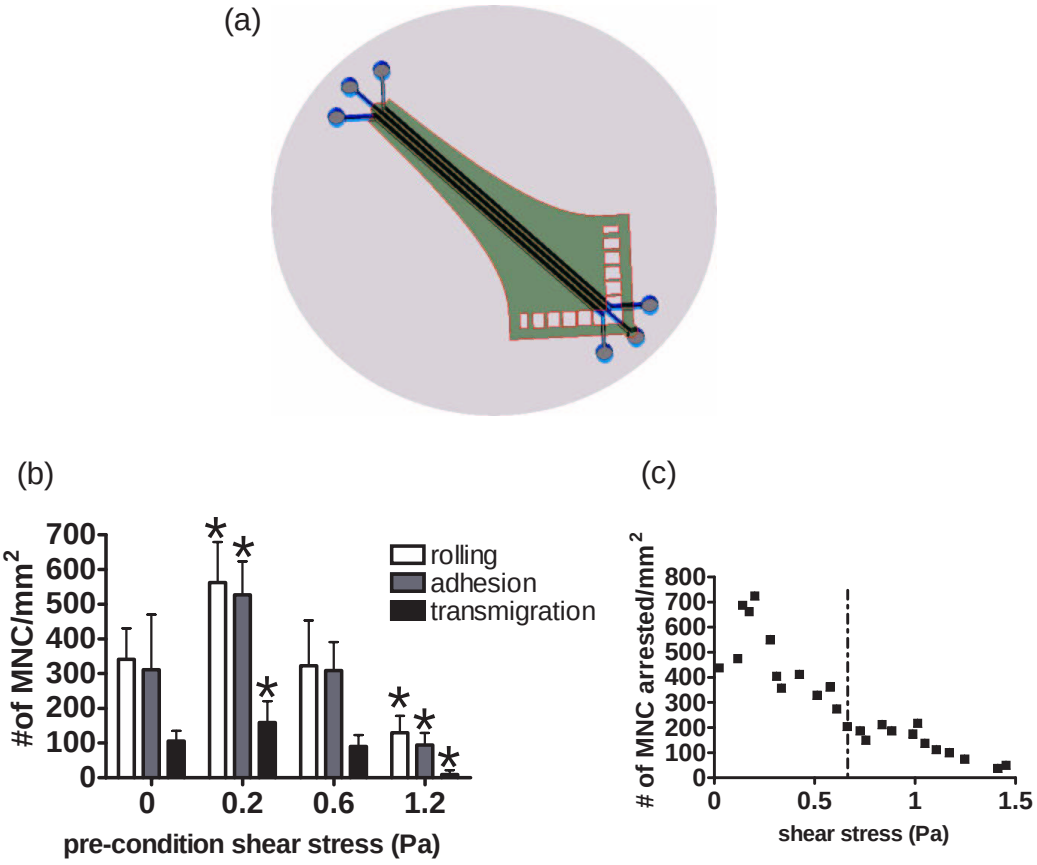

Figure 45. Monocyte recruitment as a function of pre-conditioning shear stress. (a) Monocytes (10^6/ml) were perfused at 0.2 Pa in the flow channels aligned parallel to the original flow direction placed on the EC monolayer. (b) The monocyte-endothelium interactions are plotted for specific pre-shearing magnitudes. (c) The number of monocytes firmly arrested along the rectangular channel that was transverse a HAEC monolayer preconditioned to a continuously decreasing shear field. $*p < 0.05$ versus ECs in static condition.

6. PREDICTION ERRORS IN SHEAR-MEDIATED ENDOTHELIAL CELL FUNCTION

6.1. Objectives

One of the main goals of this dissertation is to present a practical method to effectively improve the accuracy and precision in the measurement of ultrasonic wall shear rate so that medical ultrasound can be more reliably used in assessing vascular hemodynamics, EC function, and risk for focal plaque development. In order to achieve this goal, we started with the theoretical simulations (Chapter 2), which guides the design of the transmission pulse sequences and the development of the imaging process algorithms. The design is validated first with our experimental system as a proof of concept (Chapter 3), and subsequently implemented on a state of the art commercial medical scanner (Chapter 4). In this series of studies, we found our method can significantly reduce the errors in ultrasonic wall shear rate measurements compared with the conventional uncoded imaging pulses. And as expected, the measurement errors become smaller when the method is implemented on a better system. However, we can not help but wonder if the improvement in the ultrasonic shear rate estimation can indeed help medical diagnosis? Are the few percents of improvement crucial for monitoring vascular hemodynamics for the purpose of detecting arterial region suspicious of early atherogenesis? Since atherogenesis initiates from the dysfunction of endothelial cell lining on the arterial wall, we investigated the influence of shear flow on the EC inflammatory response in Chapter 5 to gain a better understanding of

the problematic shear ranges. In this chapter, we extract the important findings from previous chapters to understand how the measurement errors propagate into uncertainty in predicting EC function. The results would help to guide future improvement in ultrasonic shear rate imaging.

6.2. Ultrasonic and endothelial cellular shear flow experiment with comparable wall shear stress conditions

In order to analyze the influence of the shear rate (stress)-dependent ultrasonic shear measurement errors when correlating the estimated shear field and the corresponding change in endothelial function, the engineering aspect of ultrasonic error analysis and the biological investigation on EC functions are performed in separate controlled experiments but under comparable shear flow conditions. The reason for separate ultrasound and EC experiments is the experimental difficulty in developing a flow system for shearing a large EC monolayer for 4 hours while monitoring ultrasonically in sterile conditions. In addition, the cumulative cost of such combined experiments would be very high.

The details of the experimental setup in the ultrasound phantom studies for wall shear rate error assessment are described in Section 4.6, and the detailed procedures regarding the cellular studies are explained in Section 5.2.4. The following is a quick recapitulation of the experimental condition for both ultrasonic and cellular studies (experiment setups are shown in Fig. 46). For the ultrasonic wall shear rate measurements, a series echo data were acquired at various locations within a 3-mm high and

130-mm long Hele-Shaw flow channel, where the shear field linearly decreases from 1.9 to 0.3 Pa.

For the human aortic endothelial cell studies, a scaled down version of the Hele-Shaw flow chamber (100 μm high and 20 mm long) that delivers a linearly-varying shear field (1.6-0 Pa) was used. The monolayer was continuously treated with a low does of TNF-α (0.43 pg/ml) under shear flow for 4 hours to stimulate the inflammatory reaction in the endothelial monolayer to create an environment similar to a person under high risk of atherosclerosis, such as conditions occur in patients with chronic smoking histories and high fat diets. Shear-regulated CAM expression including ICAM-1, VCAM-1 and E-selection vary significantly over this shear range as quantified using immunofluorescence microscopy. In Section 5.3.4, we found that increased E-selectin and VCAM-1 expression triggered monocyte rolling and adhesion to endothelial cells, representing an important initial step in the atherogenic process. Therefore, data analysis in this chapter focuses on the interplay between ultrasonic measurement errors and these two adhesion molecules.

Fig. 46 recapitulates the major results we showed in previous chapters regarding the ultrasonic measurement errors and shear-mediated CAM expression on inflamed HAEC monolayer. These graphs clearly show that the accuracy and precision in ultrasonic WSS measurements or CAM expression are not constants within the physiological fluid shear range. VCAM-1 and E-selectin are more sensitive to low shear range (< 0.4 Pa) and almost no response to shear > 0.8 Pa. In contrast, ultrasonic errors are observed to be minimal in the low shear range and increases with WSS. In

order to understand the impact of correlating biased WSS estimates to shear-mediated CAM expression, the prediction errors were computed. The method of estimating the prediction errors is demonstrated in the following section.

6.3. Prediction errors in CAM expression resulted from ultrasonic shear measurement errors

6.3.1. Error analysis method

As shown in Fig. 47, the shear-mediated CAM expression data were first fitted to a 6th order polynomial curve (solid line) to serve as a template for interpolating the CAM expression. No clear difference was found in the fitted curve when a higher order polynomial model was used. Therefore, we assume the prediction error due to inappropriate fitting is minor and negligible. The upper (bias + standard deviation) and lower limit (bias - standard deviation) of the biased ultrasonic WSR estimates (true WSR + bias) were calculated and converted to WSS by multiplying the medium viscosity 0.003 Pa-s. The WSS errors were then projected onto the template (O). Prediction error is viewed as the difference between expression level at the true WSS value (∇) and the mean level at the WSS of the upper and lower bounds ($\diamondsuit$). The upper and lower bound of the prediction is the range of random error occurring in WSS measurements.

6.3.2. Prediction errors in CAM expression derived from ultrasonic measurement errors with shear-mediated CAM expression

As explained previously, we combine our findings of WSS measurement errors dependency on input WSS (Fig. 46 a, b) and CAM expression dependency on input WSS (Figs. 46 c, d) to predict errors in CAM expression measured ultrasonically as a function of input WSS. Using the method described previously, these results were obtained by first fitting the CAM expression data from Figs. 46 c, d with a 6th order polynomial, as shown in Fig. 47. Then, by selecting a point on the fitted curve, and using the data from Fig. 46 a, we were able to derive the amount of bias in estimating WSS ultrasonically. The difference between CAM expression values for true and biased WSS estimates is plotted in Figs. 48 a, b as the average error. Finally, we noted the standard error in WSS estimates from Fig. 46 b on the interpolated curve of Fig. 47. The error-prediction results for VCAM-1 and E-selectin derived from Doppler estimates (labeled narrow-band) and 13-bit Optimal coded estimates are found in Figs. 48 a, b. The corresponding values of CAM expression gave the error bars plotted in Figs. 48 a, b. Consequently, points plotted in Figs. 48 a, b are the bias errors in CAM expression as a result of bias in WSR estimates, while the error bars in Figs. 48 a, b are an estimate of measurement precision.

As expected, 13-bit Optimal code yields lower prediction errors in both VCAM-1 and E-selectin while generating the lowest ultrasonic measurement errors compared with the uncoded narrow-band Doppler pulse. The interesting thing is that, in the

average prediction errors in assessing VCAM-1 expression on the flow-conditioned HAEC monolayer, both broadband and 13-bit Optimal code yield their respective maximum prediction errors at 0.3 Pa (20% and 8%), where the lowest WSR Rbias and Rstd were observed in the ultrasonic phantom studies (Fig. 46 a, b). In this case, the prediction errors are dominated by sensitivity of VCAM-1 expression to fluid shear. The scale of the prediction errors decreases with measured WSS for both 13-bit Optimal coded and uncoded narrow-band pulses.

The pattern of shear-mediated E-selectin is slightly different from that of VCAM-1. Expression of E-selectin peaked at 0.4 Pa, with the biggest transition occurring between 0.4-0.8 Pa, and slowly dropping to a basal expression level at shear > 0.8 Pa. Therefore, instead of exhibiting similar prediction error profiles as VCAM-1, the prediction errors of shear-regulated E-selectin rose and then dropped with increasing WSS. Combined with gradually increasing ultrasonic measurement errors, the high sensitivity of E-selectin to both magnitude and difference in WSS resulted in high prediction errors at mid WSS range between 0.4 and 0.8 Pa (shown in Fig. 48 b).

6.4. Summary and Discussion

By combining the results from our previous ultrasonic WSS studies (Figs. 46 a, b) with a series of research studies on endothelial cell function under shear flow (Figs. 46 c, d,), we provide a connection between engineering measurement uncertainties and the impact of the uncertainties on analyzing shear-regulated vascular function due to mis-registration to incorrect WSS values (Figs. 48 a, b). That is, we can now discuss

the consequences of velocity errors from ultrasonic measurements in biological terms. While the largest errors in WSR estimates occur at the largest values of WSS (Fig. 46 a, b), i.e., at the highest blood velocities, the largest errors in CAM expression occur at relatively lower shear stress values. The greatest change in E-selectin expression occurs for WSS values between 0.4 - 0.8 Pa, which is the range where measurement techniques errors should be minimized. Also coded-pulse transmission reduces bias errors relative to narrow-band Doppler methods by more than a factor of 2 over the entire range. Similar improvements for VCAM-1 expression were found, although the biggest reduction in errors was obtained at a lower range of shear stress values. The error bars in Figs. 48 a, b reflect the precision of CAM expression estimates due to ultrasonic variability.

In summary, we presented the first set of data to correlate engineering measurement errors to the biological functions by performing parallel but independent ultrasonic and endothelial cellular experiments with comparable shear flow conditions. By propagating the errors in ultrasonic shear stress measurement into shear-regulated EC function, we found that broadband coded-pulse excitation techniques can not only significantly reduce ultrasonic measurement errors but also exhibit a better ability in predicting endothelial cell function in terms of shear-sensitive CAM expression. The difference in shear-regulated CAM expression under the influence of shear-dependent ultrasonic measurement errors results in different prediction error patterns although both VCAM-1 and E-selectin are highly responsive to low shear condition and quiescent under high shear. In order to accurately assess atherosclerosis-related VCAM-1

and E-selectin, ultrasonic measurement should be optimized when imaging shear condition < 0.8 Pa.

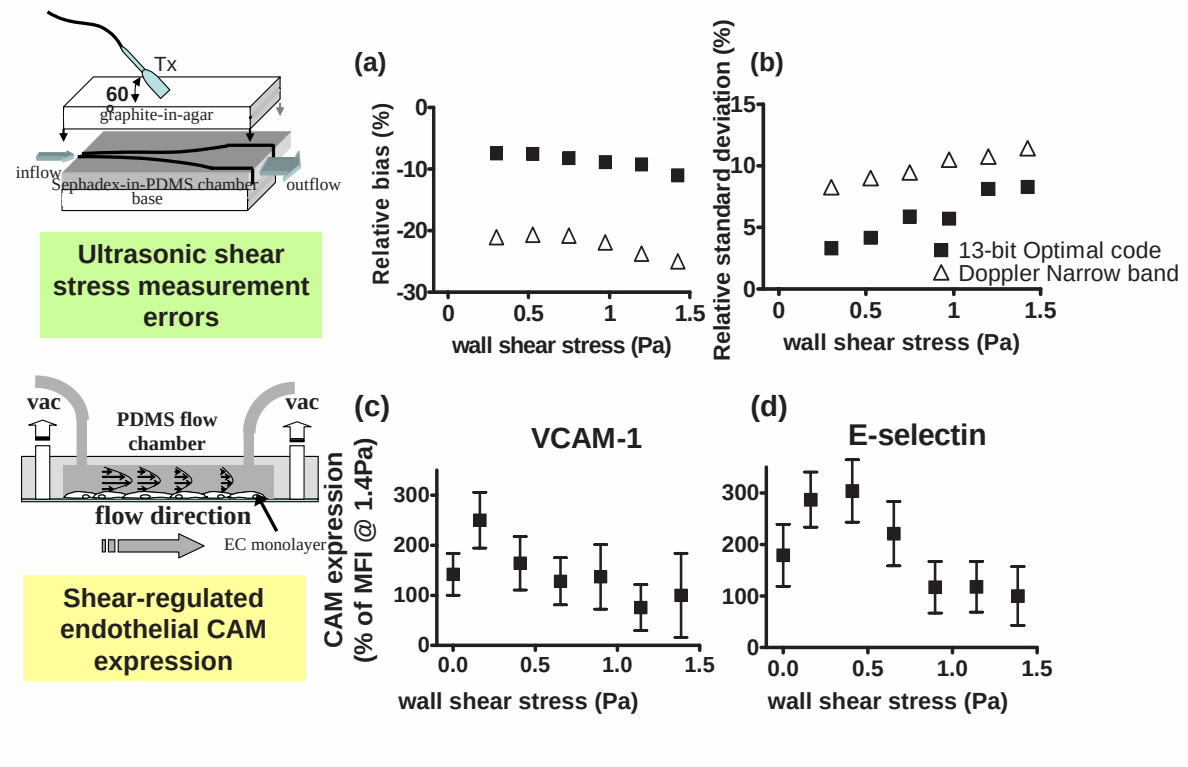

Figure 46. Ultrasonic wall shear stress measurement errors and endothelial CAM expression under similar shear flow conditions. The experiment procedures of both studies are shown on the left side of the figure. (a) systematic and (b) random measurement errors in ultrasonic shear imaging over WSS range of 0.3-1.9 Pa. The WSS errors were derived from the WSR errors (Fig. 33), which was offset by the medium viscosity (3 mPa-s). (c) VCAM-1 and (d) E-selectin expression as functions of fluid shear (0-1.6 Pa). The baseline level (100%) in (c) and (d) was set to the steady-state MFI; in this experiment steady-state expression occurs at WSS of 1.4 Pa.

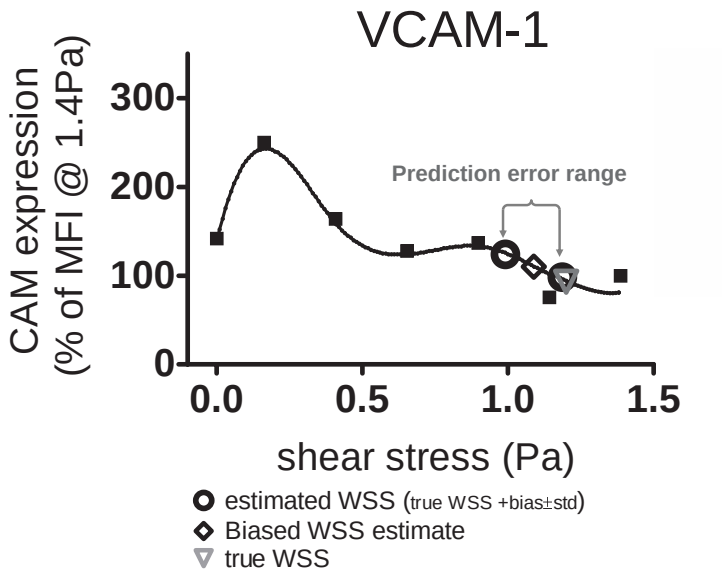

Figure 47. Representative data showing the method for estimate prediction error in CAM expression as a function of shear stress. o indicates VCAM-1 expression level at the upper (true WSS + bias + std) and lower (true WSS + bias - std) bound of the biased wall shear stress (true WSS + bias). The prediction errors at this particular shear stress for VCAM-1 expression is the difference between the mean prediction error range (♢) and the expression level where cells were conditioned at the true WSS magnitude (▽). Minimum MFI of VCAM-1 expression was found when sheared at 1.4Pa and was chosen to be the base line (100%)

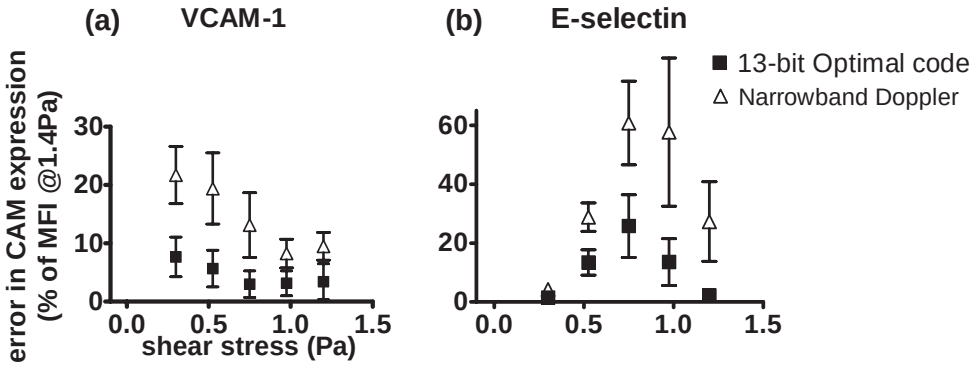

Figure 48. Prediction errors in determining cell adhesion molecule expression as a function of shear stress. Small values are what we attempt to achieve. Errors in predicting (a) VCAM-1 and (b) E-selectin expression are estimated from propagating errors in ultrasonic WSR estimates as illustrated in Fig. 47. "narrow-band" results are from typical Doppler estimates of velocity, and "13-bit Optimal code" results are the best of our proposed methods. Axis labels for (a) are the same as in Fig. 46(c), and those for (b) are the same as Fig. 46(d).

7. DISCUSSION AND CONCLUSION

7.1. Discussion

Vascular hemodynamics has been identified as an critical factor in initiating atherosclerotic plaque formation. To effectively detect arterial regions that are suspicious of developing atherosclerosis, a low-cost but reliable medical imaging method is needed to routinely monitor of vascular WSS. Non-invasive medical ultrasonic imaging shows a strong potential for success in this application due to its ability to track flow and motion in real-time. While the accuracy and precision of ultrasonic WSR estimation has room for improvement, the influence of correlating the shear-regulated vascular functions to incorrect WSS estimates is needed to be investigated. The goal of this project is to develop a robust, safe, high-resolution, and high sensitivity approach to measure vascular WSS suitable for studying hemodynamics in the vasculature.

The accuracy and precision of WSR estimates rely on the quality of estimated velocity profile. The key is to increase sensitivity in detecting weak and slow blood scatterers flowing near the vessel wall, while at the same time maintaining a high spatial resolution to minimize bias from spatial averaging. The traditional narrow-band color flow imaging method uses long duration pulse transmission to achieve high signal power and thereby increase sensitivity. However, the loss in signal bandwidth results in a significant bias in WSR estimation. By implementing coded-pulse excitation techniques, the long duration pulses can be compressed to restore spatial resolution, and therefore sensitivity can be enhanced without concomitant loss of

spatial resolution..

This work contributes three aspects in biomedical studies of arterial WSS. First, an ultrasonic broadband coded-pulse excitation method was developed in conjunction with a regularized velocity estimator to provide more accurate and precise WSR estimates. Second, the differential regulation of shear on endothelial cell function was studied, particularly in atherosclerosis-related functions such as the expression of CAM and the recruitment efficiency of leukocytes. Third, guided by the knowledge of the sensitivity of EC function in applied fluid shear, we determined the range of WSS that improvements in WSR estimation have the greatest influence on shear-mediated EC function. This dissertation describes detailed studies in the development of the ultrasonic coded-excitation WSR imaging, the regulation of shear on endothelial cell function, and the impact of ultrasonic WSR measurement errors on predicting EC functions.

7.1.1. Coded-pulse excitation for ultrasonic wall shear rate imaging

In order to design WSR imaging pulse sequences and optimize the processing strategies for ultrasonic shear rate imaging, a signal model that mimics the acoustic and flow environment of an adult carotid artery was established and tested in a series of simulations. The challenging part in developing ultrasonic shear rate imaging compared with the color-flow velocity imaging is to accurately trace the velocity profile at the blood (flow) - vessel wall (tissue) interface, which would require high spatial resolution in order to identify the interface. The large difference in echo intensities

across the vessel wall ($\sim$ 15 dB) combining with non-stationary flow patterns create a signal processing environment that is very difficult to obtain accurate WSR estimates. Numerical simulations show that it requires echo data with both high spatial resolution and high eSNR to effectively suppress the errors in WSR measurement. Bias in WSR estimates is always negative because of the spatial averaging of non-stationary shear rate values within the correlation window positioned at the vessel wall. However, in conventional ultrasonic systems, there are always tradeoffs between signal bandwidth and echo signal energy. Generally, eSNR inside the carotid artery with a uncoded broadband pulse is around 15 dB, which is considered a noise-limited condition for WSR estimation. Simulations show that eSNR enhancement is more influential than signal bandwidth at reducing velocity measurement errors. As a result, conventional ultrasonic flow imaging applications utilize long duration pulses to boost signal energy and thus improve velocity estimates, but its WSR bias remains very large ($\sim$ -28%). Coded-pulse excitation approaches high spatial resolution and high sensitivity in WSR estimation by providing both high bandwidth and high eSNR. Our results indicated that both FM and PM codes can reduce WSR errors significantly under noise-limited conditions. FM chirps are slightly less effective than PM codes. However, in situations where eSNR inside the vessel lumen is $>$ 30 dB, broadband coded-pulse excitation techniques provide no advantage over a high energy uncoded broadband image pulse at minimizing systematic and random measurement errors. However, exceeding the 30 dB eSNR threshold for an uncoded broadband imaging pulse is difficult to achieve even using commercial instruments. This reemphasizes

the advantage of using coded-pulse excitation on vascular flow or shear imaging. Although longer codes indicate higher eSNR, the range sidelobe artifact caused by the decoding step degrades the contrast resolution and increase undesired signal decorrelation, which biases the WSR estimation. As a result of that, longer code length is not necessary to further improve WSR imaging quality and the choice of code length should be optimized based on the imaging tasks.

The feasibility of the proposed coded excitation techniques method was demonstrated using our laboratory system equipped with a highly focused 10MHz transducer. At this first stage of phantom studies and proof-of-concept, a tissue-mimicking ultrasonic phantom with a flow channel diameter similar to that of an adult carotid artery was utilized. An 8 bit PM Optimal coded pulse yielded a comparable spatial resolution to an uncoded broadband but with a 10 dB increase in eSNR. Despite the noisy conditions for the experimental system, the improvement in signal strength reduced the systematic and random errors in WSR measurements from $\sim$ -65% and $\sim$ 58% down to $\sim$ -10% and $\sim$ 13%, respectively. A sinusoidal FM chirp that transmitted the same pulse energy as the 8 bit Optimal code but doubled in length was also implemented into the system. Consistent with the simulation results, Optimal coded pulses showed greater ability to lower when compared with the FM chirp pulses. This suggests that the greater energy in PM coded pulses allow for shorter duration transmission that introduce less severe decoding artifacts and therefore are better for ultrasonic WSR imaging.

At the second stage of phantom experiments, we further implemented coded-pulse

excitation techniques onto a commercial system to take advantage of its superior system performance. In this series of studies, the shear-rate-dependent ultrasonic WSR measurement errors were investigated using a Hele-Shaw flow chamber. The results indicate that the improvement in WSR estimation using coded-pulse excitation is more significant when eSNR is low. The studies show that for all imaging pulses both uncoded and coded, ultrasonic WSR measurement errors increase with fluid shear. This is possibly due to greater signal decorrelation at higher flow velocity (i.e. high fluid shear). With higher eSNR, measurement errors derived from coded pulses are less sensitive to shear. With low eSNR broadband pulses, the degradation is particularly obvious in both random and systematic errors, which states the WSR imaging is limited by noise. The shear-dependency suggests that ultrasonic WSR measurement errors can be lowered by increasing PRF to reduce the level of signal decorrelation between echo ensembles. This is verified in the simulations under laminar flow conditions, where the amount of signal decorrelation between ensembles is determined by PRF and the flow velocity parallel to the ultrasonic beam. The selection of PRF should also take in account of the round trip time for sound to travel to and from the region of interest. Based on the observations from numerical simulations and experimental results, we recommend maintaining a proper PRF that is higher than 4000 Hz when using our broadband coded-pulse WSS imaging techniques to monitor vascular WSS inside an adult carotid artery with a 9 MHz transducer.

In the third stage of ultrasonic shear rate studies, *in vivo* WSR imaging at carotid and brachial arteries were performed. Shear rate images acquired with coded pulses

exhibit a better signal penetration and spatial resolution compared with uncoded broadband and narrow-band Doppler pulses. The estimated shear rate profiles clearly show contouring patterns with shear rate decreasing toward the center of the lumen. Similar to the results reported in the phantom studies, estimated WSR values are higher than those from uncoded pulses. The estimated WSR in carotid and brachial arteries are ~ 850 and $\sim 740\ \mathrm{s}^{-1}$ respectively, which are within the data range reported in literature.[83,45,41]

7.1.2. Differential regulation of vascular shear on endothelial cell functions

Atherosclerosis is initiated by inflammatory responses at the vessel surface, which causes endothelial cell dysfunction. In order to understand the role of shear stress in triggering the inflammatory response in endothelial cell monolayers, a microfluidic Hele-Shaw flow chamber was utilized to expose the cells to a broad shear range. Our studies show that the EC monolayer stimulated with the cytokine TNF-α is more responsive to shear stress, suggesting that shear stress is not the only factor promoting the inflammatory atherogenic reaction. However, abnormally low shears can accelerate and amplify the alteration in CAM expression when the EC monolayer is not healthy, such as in vessels chronically exposed to high blood cholesterol and chemical residue from smoking. ICAM-1, which is associated with the recruitment of neutrophils, increases expression as the fluid shear increases until it reaches a steady state at shear $>$ 0.8 Pa. VCAM-1 and E-selectin, which contribute to the

recruitment of monocytes, show similar patterns in response to shear. In contrast to shear-regulated ICAM-1 expression, VCAM-1 and E-selectin are most sensitive to low shear at 0.2 and 0.4 Pa, respectively. Above those threshold values, VCAM-1 and E-selectin expression gradually decrease until they approach a baseline expression at 0.8 Pa. No significant difference in shear-mediated CAM expression was observed when a different spatial shear gradient was applied. The differential regulation of shear on CAM expression shows a complicated mechanotransduction signal pathway. The gradual change of CAM expression over the medium shear range (0.2 - 0.8 Pa) indicates that shear regulation is not an on-off step function. However, the narrow transition shear range suggests the existence of a shear threshold in up- or down-regulating CAM expression on EC monolayer.

The differential response in CAM expression shows further influence on the efficiency of recruiting leukocytes onto the shear-conditioned EC monolayer. Monocytes, the key type of leukocytes involved in early atherosclerosis, actively interact with the region of EC monolayer that has been exposed to low shear for over 4 hours. This is consistent with the observed changes in shear-mediated VCAM-1 and E-selectin expression.

This series of studies mapped the shear-dependency of CAM expression. The important finding is that the absolute shear magnitude rather than the spatial shear gradient is the key factor in altering EC functions.

7.1.3. Connecting engineering findings to biological impacts

The magnitude of arterial shear stress has been measured on various animal models and human subjects either *in vivo* or *ex vivo* using ultrasound flow imaging methods.[6,83,45,41] The WSR values measured at the locations of atherosclerotic plaques are further correlated to the shear ranges that trigger atherogenesis and alters EC functions. By combining results from the ultrasonic WSS studies and data from shear-regulated CAM expression, a connection in terms of prediction errors, associated with the uncertainties of engineering measurement and shear-dependent vascular function to biased WSS values was provided. As expected, ultrasonic coded pulse transmission provided echo signals that yielded much lower systematic and random errors in ultrasonic WSS measurements. Errors were less than those found using conventional narrow-band pulses.

The errors in predicting VCAM-1 expression are dominated by shear-dependent ultrasonic WSS measurement errors where greater errors were observed under higher shear condition. However, prediction errors in E-selectin expression are relatively low at both ends of shear due to low shear sensitivity in E-selectin expression at high shear and low measurement errors at low shear.

The shear-dependent prediction errors provide a tool to evaluate the impact of measurement errors in correlating biological function. It can be useful in developing new methods to improve ultrasonic measurements. In order to focus on monitoring shear-mediated E-selectin and VCAM-1 expression that associated with atherogene-

sis, ultrasonic WSR measurement should be optimized when imaging shear conditions less than 0.8 Pa.

7.2. Conclusion

In this dissertation, broadband coded-pulse excitation techniques were incorporated into ultrasonic WSR imaging and implemented on both our experimental ultrasonic system and a commercial medical ultrasonic system. New post-processing algorithms, including a signal condition method to minimize amplitude differences at the tissue-flow interface and a regularized broadband velocity estimator, were developed to provide accurate and robust shear rate estimates. Coded pulses generated echo signals with both high spatial resolution and high eSNR. This resulted in significant reductions in both systematic and random WSR errors. Two versions of Hele-Shaw flow were developed for investigating shear-dependent EC functions (CAM expression and leukocyte recruitment) and ultrasonic WSS measurement errors. The prediction errors obtained by combining the ultrasonic measurement uncertainties and biological function indicate ultrasonic WSS imaging method should be optimized when imaging the shear range lower than 0.8 Pa. Better understanding of the code selection and the effect of decoding artifacts can further improve the WSR imaging performance. The performance and efficiency of the post-processing algorithm can be further improved and directly implemented onto a ultrasonic imaging system for real-time image processing.

APPENDIX A. LIST OF ABBREVIATIONS

CAM	cell adhesion molecule	PM	phase-modulated
CC	cross correlation	PMN	polymorphonuclear leucocyte
CFD	computational fluid dynamics	PPFC	parallel-plate flow chamber
EC	endothelial cell	PRF	pulse repetition frequency
ECG	electrocardiogram	psf	point spread function
eSNR	echo signal-to-noise ratio	PSGL-1	P-selectin glycoprotein ligand-1
FITC	fluorescein	RF	radio frequency
FM	frequency-modulated	TBP	time-bandwidth product
HAEC	human aortic endothelial cell	PBS	phosphate-buffered saline
HHB	Hepes buffer	PDMS	poly-dimethylsiloxane
HSA	human serum albumin	TEQ	tissue equalization
ICAM-1	intravascular cell adhesion molecule	TNF-α	tumor necrosis factor -α
IVUS	intravascular ultrasound	URI	ultrasound research interface
LDL	low density lipoprotein	VCAM-1	vascular cell adhesion molecule-1
LFA-1	leukocyte function-associated antigen-1	VLA-4	very late antigen-4
mAB	monoclonal antibody	WF	Wiener filter
MF	matched filter	WGN	white Gaussian noise
MNC	mononuclear cell	WSR	wall shear rate
MRI	magnetic resonance imaging	WSS	wall shear stress
MFI	mean fluorescence intensity		

APPENDIX B. LIST OF PUBLICATIONS AND PRESENTATIONS

⋆ 1. **Tsou JK**, Simon SI, Insana MF, "Role of ultrasonic velocity estimation errors in assessing inflammatory response and vascular risk", *Biomedical Engineering Society Annual Fall Meeting*, 2006.

2. Sridhar M, **Tsou JK**, Insana MF, "In-vivo imaging of breast tissue viscoelasticity using ultrasound", *Biomedical Engineering Society Annual Fall Meeting*, 2006.

⋆ 3. **Tsou JK**, Simon SI, Barakat AI, Insana MF, "Role of ultrasonic shear rate estimation errors in assessing early stage of atherogenesis," *Annals of Biomedical Engineering, (In preparation).*

⋆ 4. **Tsou JK**, Liu J, Insana MF, "Coded excitation improves vascular wall shear rate estimation", *Proc IEEE Ultrasonics Symp, 2006 (In press).*

⋆ 5. **Tsou JK**, Simon SI, Insana MF, "Role of ultrasonic velocity estimation errors in assessing inflammatory response and vascular risk", *Proc IEEE Ultrasonics Symp, 2006 (In press).*

6. Sridhar M, **Tsou JK**, Insana MF, "In-vivo imaging of breast tissue viscoelasticity", *Proc IEEE Ultrasonics Symp, 2006, (In press).*

⋆ 7. **Tsou JK**, Ting HJ, Schaff UY, Insana MF, Simon SI, "Spatial regulation of shear stress in cultured human aortic endothelial cell functions", *Arter. Thromb. Vasc. Biol. (In review).*

⋆ 8. **Tsou JK**, Liu J, Insana MF, "Modeling and phantom studies of ultrasonic wall shear rate measurements using coded pulse excitation", *IEEE Trans Ultrason. Ferroelec. Freq. Contrl.*, vol. 53, pp 724-734, 2006.

9. **Tsou JK**, Ting HJ, Schaff UY, Insana MF, Simon SI, " Spatial regulation of shear stress in cultured human aortic endothelial cell functions", *Experimental Biology*, 2006.

⋆ 10. **Tsou JK**, Liu J, Insana MF, "Vascular wall shear rate measurement using coded excitation techniques", *Proc. SPIE*, vol. 5750, pp269-280, 2005.

11. Sridhar M, Du H, Pellot-Barakat C, **Tsou JK**, Insana MF, " Ultrasonic imaging of biochemical changes in tissues", *Proc IEEE Ultrasonics Symp*, vol. 3, pp2145-2148, 2004.

12. **Tsou JK**, Liu J, Pellot-Barakat C, Insana MF, "Improved accuracy of vascular wall shear rate measurements", *Proc IEEE Ultrasonics Symp*, vol.2, pp1239-1242, 2004.

13. Pellot-Barakat C, Frouin F, Herment A, Mai JJ, Lindfors K, **Tsou JK**, Von Behren P, Insana MF, "A regularized approach to freehand ultrasound elastography of breast lesions", *IEEE ISBI*, 2004.

14. **Tsou JK**, Mai JJ, Lupotti FA, Insana MF, "Simultaneous Narrow-band Ultrasonic Strain-Flow Imaging", *Proc SPIE, vol. 5373*, pp173-183, 2004.

15. Mai JJ, **Tsou JK**, Pellot-Barakat C, Hornof WJ, Kargel CJ, Insana MF, "Vascular compliance using elasticity imaging", *Proc IEEE Ultrasonics Symp*, 01CH37263, pp. 1577-80, 2001.

⋆ indicates the publication or presentation is directly related to the thesis project.

APPENDIX C. ULTRASONIC PHANTOMS

C.1. Ultrasonic tissue-mimicking flow phantoms

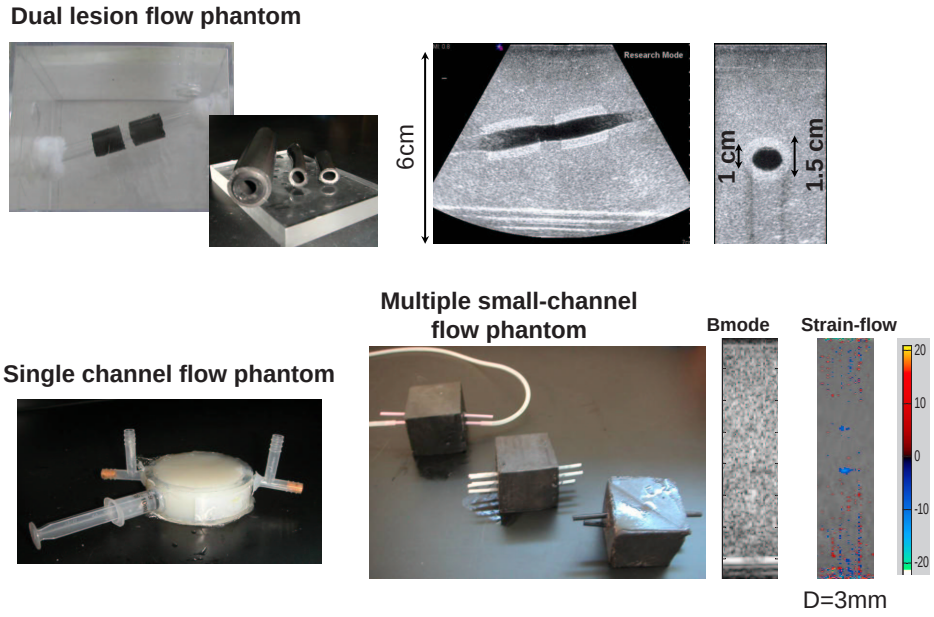

C.2. Ultrasonic tissue-mimicking speciality phantoms

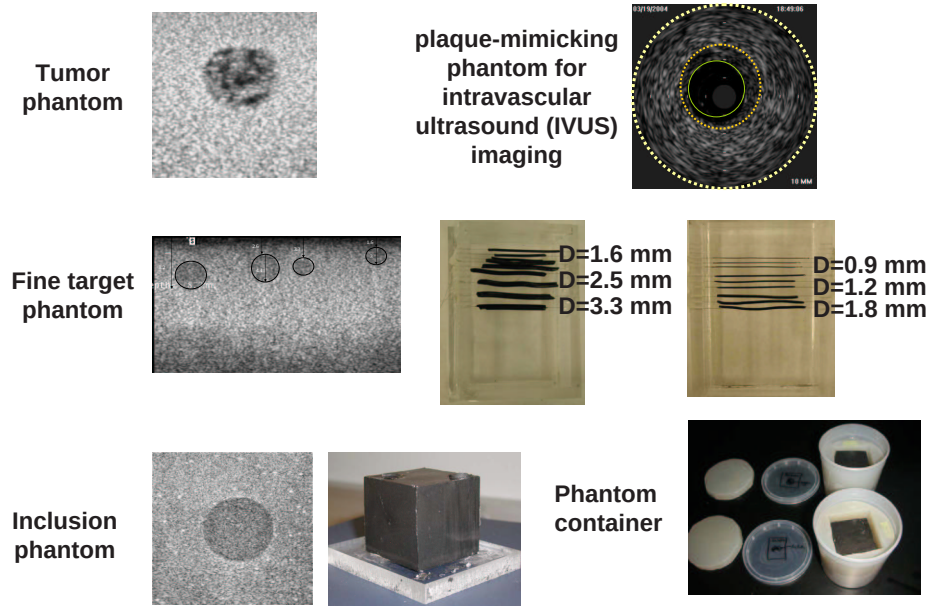

REFERENCES

1. "Heart disease and strole statistics-206 update," *Circculation* **113**, pp. e85–e151, 2006.
2. C. G. Caro, J. M. Fitz-Gerald, and R. C. Schroter, "Atheroma and arterial wall shear: observation, correlation and proposal of a shear dependent mass transfer mechanism of atherogenesis," in *Proc. R. Soc. London (Biol.)*, 177, pp. 109–159, 1971.
3. J. Farmer and G. Torre-Amione, "Atherosclerosis and inflammation," *Current Atherosclerosis Reports* **4**, pp. 92 – 98, 2002.
4. R. M. Nerem, "Vascular fluid mechanics, the arterial wall and atherosclerosis," *J. Biomech. Eng.* **114**, pp. 274–282, 1992.
5. A. M. Malek, S. L. Alper, and S. Izumo, "Hemodynamic shear stress and its role in atherosclerosis," *JAMA* **282**, pp. 2035–2042, 1999.
6. D. P. Giddens, Z. K. Zarins, and S. Glagov, "The role of fluid mechanics in the localization and detection of atherosclerosis," *J. Biomech. Eng.* **115**, pp. 588–594, 1993.
7. G. Helmlinger, B. C. Berk, and R. M. Nerem, "Calcium responses of endothelial cell monolayers subjected to pulsatile and steady laminar flow differ," *Am. J. Physiol.* **269**, pp. C367–C375, 1995.
8. D. N. Ku, D. P. Giddens, C. K. Zarins, and S. Glagov, "Pulsatile flow and atherosclerosis in the human carotid bifurication," *Atherosclerosis* **5**, pp. 293–302, 1985.
9. A. J. Lusis, "Atherosclerosis," *Nature* **407**, pp. 233–241, 2000.
10. P. Libby, "Inflammation in atherosclerosis," *Nature* **420**, pp. 868–874, 2002.
11. M. A. J. Gimbrone, "Vascular endothelium, hemodynamic forces and atherogenesis," *Am. J. Pathol.* **155**, pp. 1–5, 1999.
12. J. J. Chiu, B. S. Wung, J. Y. Shyy, H. J. Hsieh, and D. L. Wang, "Reactive oxygen species are involved in shear stress-induced intercellular adhesion molecule-1 expression in endothelial cells," *Arterioscler. Thromb. Vasc. Biol.* **17**, pp. 3570–3577, 1997.
13. B. R. Blackman, K. A. Barbee, and L. E. Thibault, "In vitro cell shearing device to investigate the dynamic response of cells in a controlled hydrodynamic environment," *Ann. Biomed. Eng.* **28**, pp. 363–372, 2000.
14. J. J. Chiu, L. J. Chen, P. L. Lee, C. I. Lee, L. W. Lo, S. Usami, and S. Chien, "Shear stress inhibits adhesion molecule expression in vascular endothelial cells induced by coculture with smooth muscle cells," *Blood* **101**, pp. 2667–2674, 2003.

15. J. J. Chiu, P. L. Lee, C. N. Chen, C. I. Lee, S. F. Chang, L. J. Chen, S. C. Lien, Y. C. Kao, S. Usami, and S. Chien, "Shear stress increases ICAM-1 and decreases VCAM-1 and E-selectin expressions induced by tumor necrosis factor-α in endothelial cells," *Arteriscler. Thromb. Vasc. Biol.* **24**, pp. 73–79, 2004.
16. S. Mohan, N. Mohan, A. J. Valente, and E. A. Sprague, "Regulation of low shear flow-induced HAEC VCAM-1 expression and monocyte adhesion.," *Am. J. Physiol.* **145**, pp. C1100–C1107, 1999.
17. H. Tsuboi, J. Ando, R. Korenaga, Y. Tajada, and A. Kamiya, "Flow stimulates ICAM-1 expression time and shear stress dependently in cultured human endothelial cells," *Biochemical Biophysical research communications* **206**, pp. 988–996, 1995.
18. H. Morawietz, R. Talanow, M. Szibor, U. Rueckschloss, A. Schubert, B. Bartling, D. Darmer, and J. Holtz, "Regulation of the endothelin system by shear stress in human endothelial cells," *J. Physiol.* **525**, pp. 761–770, 2000.
19. A. I. Barakat and D. K. Lieu, "Differential responsiveness of vascular endothelial cells to different types of fluid mechanical shear stress," *Cell Biochemistry and Biophysics* **38**, pp. 323–343, 2003.
20. J. W. Hallett, J. L. Mills, J. J. Earnshaw, and J. A. Reekers, *Comprehensive Vascular and Endovascular Surgery*, Mosby, 2003.
21. M. Noris, M. Morigi, R. Donadelli, S. Aiello, M. FOPPOLO, M. TODESCHINI, S. ORISIO, G. REMUZZI, and A. REMUZZI, "Nitric oxide synthesis by cultured endothelial cells is modulated by flow condition," *Circ. Res.* **76**, pp. 536–543, 1995.
22. B. V. Khan, D. G. Harrison, M. T. Olbrych, and R. W. Alexander, "Nitric oxide regulates vascular cell adhesion molecule-1 gene expression and erdox-sensitive transcriptional events in human vascular endothelial cells," *Proc. Natl. Acad. Sci. USA* **93**, pp. 9114–9119, 1996.
23. K. Ley and Y. Huo, "VCAM-1 is critical in atherosclerosis," *J. Clin. Invest* **107**, pp. 1209–1210, 2001.
24. M. I. Cybulsky, K. Iiyama, H. Li, S. Zhu, M. Chen, M. Iiyama, V. Davis, J. C. Gutierrez-ramos, P. W. Connelly, and D. S. Milstone, "A major role for VCAM-1, but not ICAM-1, in early atherosclerosis," *J. Clin. Invest.* **107**, pp. 1255–1262, 2001.
25. S. E. Abbot, W. J. D. Whish, C. Jennison, D. R. Blake, and C. R. Stevens, "Tumour necrosis factor α stimulated rheumatoid synovial microvascular endothelial cells exhibit

increased shear rate dependent leucocyte adhesion in vitro," *Ann. Rheum. Dis.* **58**, pp. 573–581, 1999.

26. R. S. Gonzales and T. M. Wick, "Hemodynamic modulation of monocytic cell adherence to vascular endothelium," *Annals of Biomedical Engineering* **24**, pp. 382–393, 1996.
27. A. Dardik, L. L. Chen, J. Frattini, H. Asada, F. Aziz, F. A. Kudo, and B. E. Sumpio, "Differential effects of orbital and laminar shear stress on endothelial cells," *J. Vasc. Surg.* **41**, pp. 869–880, 2005.
28. D. C. Chappell, S. E. Varner, R. M. Nerem, R. M. Medford, and R. W. Alexander, "Oscillatory shear stress stimulates adhesion molecule expression in cultured human endothelium," *Circ. Res.* **82**, pp. 532–539, 1998.
29. G. Helmlinger, R. V. Ggeiger, S. Schreck, and R. M. Nerem, "Effects of pulastile flow on cultured vascular endothelial cell morphology," *J. Biomech. Eng.* **113**, pp. 123–131, 1991.
30. C. N. Chen, S. F. Chang, P. L. LEE, K. Chang, L. J. Chen, S. Usami, S. Chien, and J. J. Chiu, "Neutrophils, lymphocytes and monocytes exhibit diverse behaviors in transendothelial and subendothelial migrations under co-culture with smooth muscle cells in disturbed flow," *Blood* **107**, pp. 1933–1942, 2006.
31. C. R. White, M. Haidekker, X. Bao, and J. A. Frangos, "Temporal gradients in shear, but not spatial gradients, stimulate endothelial cell profliferation," *Circulation* **103**, pp. 2508–2513, 2001.
32. P. S. Tsao, R. Buitrago, J. R. Chan, and J. P. Cooke, "Fluid flow inhibits endothelial adhesiveness," *Circulation* **94**, pp. 1682–1689, 1996.
33. A. G. Passerini, D. C. Polacek, C. Shi, N. M. Francesco, E. Manduchi, G. R. Grant, W. F. Pritchard, S. Powell, G. Y. Chang, C. J. J. Stoeckert, and P. F. Davies, "Coexisting proinflammatory and antioxdative endothelial transcription profiles in a disturbed flow region of the adult porcine aorta," *Proc. Natl. Acad. Sci. USA* **101**, pp. 2482–2487, 2004.
34. R. Ross, "The pathogenesis of atherosclerosis: a perspective for the 1990s," *Nature* **362**, pp. 801–809, 1993.
35. S. P. Wu, S. Ringgaard, S. Oyre, M. S. Hnsen, S. Rasmus, and E. M. Pedersen, "Wall shear rates differ between the normal coarotid, femoral, and brachial arteries: an in vivo MRI study," *Magn. Reson. Imag.* **19**, pp. 188–193, 2004.

36. J. A. Jensen, *Estimation of Blood Velocities Using Ultrasound:A Signal Processing Approach*, Cambridge University Press, 1996.

37. R. S. Reneman, T. Arts, and A. P. G. Hoeks, "Wall shear stress- an important determinant of endothelial cell function and structure in the arterial system in vivo," *J. Vasc. Res.* **43(4)**, pp. 251–269, 2006.

38. P. Papathanasopoulou, S. Z. Zhao, U. Kohler, M. B. Robertson, Q. Long, P. Hoskins, X. Y. Xu, and I. Marshall, "MRI measurement of time-resoluved wall shear stress vectors in a carotid bifurcation model, and comparison with CFD preductions," *Magn. Reson. Imag.* **17**, pp. 153–162, 2003.

39. C. P. Cheng, D. Paker, and C. A. Taylor, "Quantification of wall shear stress in large blood vessels using lagrangian interpolation functions with cine phase-contrast magnetic resonance imaging," *Ann. Biomed. Eng.* **30**, pp. 1020–1032, 2002.

40. J. N. Oshinki, D. N. Ku, S. Mukundan, F. Loth, and R. I. Pettigrew, "Determination of wall shear stress in the aorta with the use of MR phase velocity mapping," *Magn. Reson. Imag.* **5**, pp. 640–647, 1995.

41. A. P. G. Hoeks, S. K. Samijo, P. J. Brands, and R. S. Reneman, "Noninvasive determination of shear rate distribution across the arterial lumen," *Hypertension* **26(1)**, pp. 26–33, 1995.

42. G. Couturier, A. Voustaniouk, J. Weinberger, and V. Fuster, "Correlation between coronary artery disease and aortic arch plaque thickness measured by non-invasive B-mode ultrasoundgraphy," *Atherosclerosis* **185**, pp. 159–164, 2006.

43. P. J. Brands, A. P. G. Hoeks, L. Hofstra, and R. S. Reneman, "A noninvasive method to estimate wall shear rate using ultrasound," *Ultrasound Med. Biol.* **21**, pp. 171–185, 1995.

44. R. Dammers, F. Stifft, J. Tordoir, J. Hameleers, A. Hoeks, and P. Kitslaar, "Shear stress depends on vascular territory: comparison between common carotid and brachial artery," *J. Appl. Physiol.* **94**, pp. 485–489, 2003.

45. S. K. Samijo, J. M. Willigers, R. Barkhuysen, P. J. E. H. M. KITSLAAR, R. S. RENEMAN, P. J. BRANDS, and A. P. G. HOEKSf, "Wall shear stress in the human common carotid artery as function of age and gender," *Cardiovasc Res* **39**, pp. 515–522, 1998.

46. H. B. Kim, J. Hertzberg, and R. Shandas, "In vitro study of wall shear stress measurement using echo-piv technique," in *Proc. Summer bioengineering conference*, pp. 71–72, 2003.
47. J. J. Wentzel, F. J. H. Gijsen, N. Stergiopulos, P. W. Serruys, C. J. SLAGER, and R. KRAMS, "Shear stress, vascular remodeling and neointimal formation," *J. of Biomech.* **36**, pp. 681–688, 2003.
48. S. P. Wu, S. Ringgaard, and E. Pedersen, "Three-dimensional phase contrast velocity mapping acquisition improves wall shear stress estimation in vivo," *Magn. Reson. Imag.* **22**, pp. 345–351, 2004.
49. J. K. Tsou, J. Liu, and M. F. Insana, "Modeling and phantom studies of ultrasonic wall shear rate measurements using coded pulse excitation," *IEEE Trans. Ultrason. Ferroelec. Freq. Contrl.* **53**, pp. 724–734, 2006.
50. C. Kargel, G. Hoebernreich, B. Trummer, and M. F. Insana, "Adaptive clutter rejection filtering in ultrasonic strain-flow imaging,," *IEEE Trans. Ultrason. Ferroelec. Freq. Contrl.* **50**, pp. 824–835, 2003.
51. R. Y. Chiao and X. Hao, "Coded excitation for diagnostic ultrasound: a system developer's perspective," *IEEE Trans. Ultrason. Ferroelec. Freq. Contrl.* **52(2)**, pp. 160–170, 2005.
52. P. E. Hughes and T. V. How, "Pulsatile velocity distribution and wall shear rate measurement using pulsed doppler ultrasound," *J. Biomech* **27**, pp. 103–110, 1994.
53. D. S. Zrnic, "Spectral moment estimators from correlated pulse pairs," *IEEE Trans. Aero. Electron. Sys.* **AES-13**, pp. 344–354, 1977.
54. P. E. Hughes and T. V. How, "Quantitative measurement of wall shear rate by pulsed Doppler ultrasound," *Journal of Medical Engineering & Technology* **17**, pp. 58–64, 1993.
55. P. Flaud, Bensalah, and P. Peronneau, "Deconvolution process in measurement of arterial velocity profiles via an ultrasonic pulsed doppler velocimeter for evaluation of the wall shear rate," *Ultrasound in Med. & Biol.* **23**, pp. 425–436, 1997.
56. M. O'Donnell, "Coded excitation system for improving the penetration of real-time phased-array imaging systems," *IEEE Trans. Ultrason. Ferroelec. Freq. Contrl.* **39**, pp. 341–351, 1992.
57. J. Liu and M. F. Insana, "Coded pulse excitation for ultrasonic strain imaging," *IEEE Trans. Ultrason. Ferroelec. Freq. Contrl.* **52(2)**, pp. 231–240, 2005.

58. B. Haider, P. A. Lewin, and K. E. Thomenius, "Pulse elongation and deconvolution filtering for medical ultrasonic imaging," *IEEE Trans. Ultrason. Ferroelectr. Freq. Control* **45**, pp. 98 – 113, 1998.
59. M. H. Pedersen, T. X. Misaridis, and J. A. Jensen, "Clinical evaluation of chirp-coded excitation in medical ultrasound," *Ultrasound in Med. & Biol.* **29(6)**, pp. 895–905, 2003.
60. Y. Wang, K. Metzger, D. N. STEPHENS, G. WILLIAMS, S. BROWNLIE, and M. O'DONNELL, "Coded EXcitation with Spectrum Inversion (CEXSI) for ultrasound array imaging.," *IEEE Trans. Ultrason. Ferroelec. Freq. Contrl.* **50(7)**, pp. 805–823, 2003.
61. M. Skolnik, *Radar handbook*, McGraw-Hill, Inc., 2 ed., 1990.
62. A. P. G. Hoeks, T. G. J. Arts, P. J. Brands, and R. S. Reneman, "Comparison of the performance of the RF cross-correlation and Doppler autocorrelation technique to estimate the mean velocity of simulated ultrasound signals," *Ultrasound Med. & Biol.* **19**, pp. 727–740, 1993.
63. M. A. Benkhelifa, M. Gindre, J. Y. L. Huerou, and W. Urbach, "Echography using correlation techniques: choice of coding signal," *IEEE Trans. Ultrason. Ferroelec. Freq. Contrl.* **41**, pp. 579–587, 1994.
64. R. L. Frank, "Polyphase codes with good noneriodic correlation properties," *IEEE Trans. Inform. Theory* **IT-9**, pp. 43–45, 1963.
65. D. Huffman, "The generation pf impulse-equivalent pulse trains," *IEEE Trans. Inform. Theory* **8**, pp. 10–16, 1962.
66. W. H. Chen and J. L. Deng, "Ultrasonic non-destructive testing using barker code pulse compression techniques," *Ultrasonics* **26(1)**, pp. 23–26, 1988.
67. J. Ruprecht and M. Rupf, "On the search for good aperiodic binary invertible sequences," *IEEE Trans. Inform. Theory* **42**, pp. 1604–1612, 1996.
68. R. Y. Chiao and X. Hao, "Coded excitation for diagnostic ultrasound: a system developer's perspective," *IEEE Ultrason. Symp.* **03CH37476C**, pp. 437–448, 2003.
69. M. J. Golay, "Complementary series," *IRE Trans. Inform. Theory* **IT-7**, pp. 82–87, 1961.
70. T. X. Misaridis and J. A. Jensen, "An effective coded excitation scheme based on a predistorted FM signal and an optimized digital filter," *Proc. IEEE Ultrason. Symp.* –, pp. 1589 – 1593, 1999.

71. J. Liu, C. K. Abbey, and M. F. Insana, "Linear approach to axial resolution in elasticity imaging," *IEEE Trans. Ultrason. Ferroelec. Freq. Contrl.* **51(6)**, pp. 716–725, 2004.

72. J. K. Tsou, J. J. Mai, F. A. Lupotti, and M. F. Insana, "Simutaneous narrow-band ultraonic strain-flow imaging," in *Proc of SPIE*, 2004.

73. C. Kargel, G. Plevnik, B. Trummer, and M. F. Insana, "Doppler ultrasound systems designed for tumor blood flow imaging," *IEEE Trans. Ultrason. Ferroelec. Freq. Contrl.* **53**, pp. 524–536, 2004.

74. Y. C. Fung, *Biomechanics*, Springer, 1993.

75. K. V. Ramnarine, D. K. Nassiri, P. R. Hoskins, and J. Lubbers, "Validation of a new blood-mimicking fluid for use in doppler flow test objects," *Ultrasound. Med. Biol.* **24**, pp. 451–459, 1998.

76. E. Madsen, J. Zagzebski, and G. Frank, "Oil-in-gelatin dispersions for use as ultrasonically tissue-mimicking materials," *Ultrasound Med Biol.* **8**, pp. 277–87, 1982.

77. F. A. Kudo, B. Warycha, P. J. Juran, H. Asada, D. Teso, F. Aziz, J. Frattini, B. E. Sumpio, T. Nishibe, C. Cha, and A. Dardik, "Differential responsiveness of early- and late-passage endothelial cells to shear stress," *Am J Surg* **190(5), pages =**.

78. S. Usami, H. H. Chem, Y. Zhao, S. Chien, and R. Skalak, "Design and construction of a lineaer shear stress flow chamber," *Annals of Biomedical Engineering* **21**, pp. 77–83, 1993.

79. D. R. Lide, *CRC Handbook of Chemistry and Physics*, CRC Press, 86 ed., 2005.

80. Y. S. J. Li, J. H. Haga, and S. Chien, "Molecular basis of the effects of shear stress on vascular endothelial cells," *J. Biomech.* **38**, pp. 1949–1971, 2005.

81. E. Dejana, F. Breviario, and L. Caveda, "Leukocyte-endothelial cell adhesive receptors," *Clin. Exp. Rheumatol.* **S10**, pp. 25–28, 1994.

82. N. DePaola, M. A. Gimbrone, P. F. Davies, and F. Dewey, "Vascular endothelium responds to fluid shear stress gradients," *Arterioscler. Thromb.* **12**, pp. 1254–1257, 1992.

83. S. K. Samijo, J. M. Willigers, P. J. Brands, R. Barkhuysen, R. S. Reneman, P. J. Kitslaar, and A. P. G. Hoeks, "Reproducibility of shear rate and shear stress assessment by means of ultrasound in the common carotid artery of young human makes and females," *Ultrasound in Med. & Biol.* **23**, pp. 583–590, 1997.